INSTITUTE OF PHYSICS POLISH ACADEMY OF SCIENCES

DOCTORAL DISSERTATION

TOPOLOGICAL AND NON-TOPOLOGICAL BOUNDARY STATES IN SNTE AND HGTE MATERIALS

Supervisors

DR.
TIMO TAPIO HYART

DR. HAB.
WOJCIECH MIKOŁAJ BRZEZICKI

Author
NGUYEN MINH NGUYEN

*Thesis submitted in fulfillment of the requirements
for the degree of Doctor of Philosophy*

in the

*International Centre for Interfacing Magnetism and
Superconductivity with Topological Matter*

Acknowledgements

Declaration

I, Nguyen M. Nguyen, declare that this thesis entitled "Topological and non-topological boundary states in SnTe and HgTe materials" and the work presented in it are my own. I confirm that:

- This work was done wholly while in candidature for a research degree at the Institute of Physics, Polish Academy of Sciences.

- Where any part of this thesis has previously been submitted for a degree or any other qualification at this Institute or any other institution, this has been clearly stated.

- Where I have consulted the published work of others, this is always clearly attributed.

- Where I have quoted from the work of others, the source is always given or cited. Except for such quotations, this thesis is entirely my work.

- I have acknowledged all primary sources of help.

- Where the thesis is based on work done by myself jointly with others, I have made clearly what was done by others and what I have contributed.

Warsaw, August 17, 2023

NGUYEN MINH NGUYEN

Abstract

T his dissertation focuses on the classification of strong topological insulators and superconductors, gapless topological phases, and higher order topological phases supporting protected corner states and hinge states. In this thesis, two main research topics were considered. The first topic of our research explored topological boundary states in SnTe. SnTe materials ($Sn_{1-x}Pb_xTe_{1-y}Se_y$) have proven to be highly versatile in investigating the interplay between topology and different types of symmetry-breaking perturbations during the last decade. Our study focused on examining SnTe nanowires under the influence of combinations of a Zeeman field, s-wave superconductivity, and an inversion-symmetry-breaking field. Throughout our research, we successfully revealed the origin of robust corner states and hinge states in the normal state of SnTe. We observed gapless bulk Majorana modes protected by inversion symmetry, leading to quantized thermal conductance in ballistic wires. Additionally, introducing an inversion-symmetry-breaking field caused the bulk Majorana modes to become gapped, resulting in the appearance of topologically protected localized Majorana zero modes at the ends of the nanowire. While we primarily focused on relatively thin nanowires, the observed trends in thickness dependence suggest that realistic nanowire thicknesses could achieve topologically non-trivial phases with experimentally attainable values of the Zeeman field. These findings hold promising possibilities for advancing our understanding and utilization of topological phenomena in SnTe nanowires, and they open up new opportunities for controlling and creating Majorana zero modes by manipulating inversion-symmetry-breaking fields (e.g. via ferroelectricity).

In our second research project, we direct our attention to investigating non-topological boundary states in candidate materials for quantum spin Hall insulators, such as HgTe/CdTe and InAs/GaSb heterostructures. We have observed that these multilayer structures not only host topologically protected helical edge modes but also exhibit additional edge states that can have an impact on scattering and transport, potentially deteriorating the quality of the quantum spin Hall effect. Employing first-principles calculations, we construct an effective tight-binding model for the HgTe/CdTe, HgS/CdTe, and InAs/GaSb heterostructures and discover that these materials support extra edge states influenced by the edge termination. The microscopic origin of these additional edge states can be traced back to a minimal model which support flat bands and nontrivial quantum geometry, which gives rise to polarization charges at the edges. As the flat bands interact with each other and other states, when forming the Hamiltonian that describes the entire heterostructure, these polarization charges manifest as the observed additional edge states. Notably,

in HgTe/CdTe quantum wells, the additional edge states lie far from the Fermi level, rendering them inactive in the transport process. However, in HgS/CdTe and InAs/GaSb heterostructures, these states emerge within the bulk energy gap, allowing for the possibility of multimode edge transport. Finally, we demonstrate that since these additional edge modes are non-topological, it is possible to eliminate them from the bulk energy gap by modifying the edge potential, such as using a side gate or chemical doping.

The research presented in the dissertation has been published in two scientific articles:

- Nguyen, N. M.; Brzezicki, W., & Hyart, T. Corner states, hinge states, and Majorana modes in SnTe nanowires. **Phys.Rev.B.105.075310 (2022)**

- Nguyen, N. M.; Cuono, G.; Islam, R.; Autieri, C.; Hyart, T., & Brzezicki, W. Unprotected edge modes in quantum spin Hall insulator candidate materials, **PhysRevB.107.045138 (2023)**

Streszczenie

T a rozprawa skupia się na klasyfikacji silnych izolatorów topologicznych i nad-przewodników, faz topologicznych bez przerw i faz topologicznych wyższego rzędu wykazujących obecność stanów narożnych i krawędziowych. W niniejszej pracy rozważano dwa główne wątki badawcze. Pierwszym tematem badań były stany topologiczne w SnTe. Materiały typu SnTe okazały się bardzo wszechstronne w badaniu wzajemnych zależności między topologią a różnymi rodzajami zaburzeń łamiących symetrię w ciągu ostatniej dekady. Przedstawione tu badania koncentrowały się na nanoprzewodów SnTe pod wpływem kombinacji pola magnetycznego Zeemana, nadprzewodnictwa typu s i pola łamiącego symetrię inwersji. W trakcie badań udało się wyjaśnić pochodzenie stanów narożnych i krawędziowych w fazie normalnej SnTe. Zaobserwowano także stany Majorany bez przerw chronione przez symetrię inwersji, co prowadzi do skwantyzowanego przewodnictwa cieplnego w drutach balistycznych. Dodatkowo wprowadzenie pola łamiącego symetrię inwersji spowodowało, że objętościowe stany Majorany uzyskały przerwę energetyczną, co spowodowało pojawienie się topologicznie chronionych stanów Majorany zlokalizowanych na końcach nanoprzewodu. Chociaż skupiliśmy się przede wszystkim na stosunkowo cienkich nanoprzewodach, obserwowane trendy w zależności od grubości sugerują, że realistyczne grubości nanoprzewodów mogą osiągnąć topologicznie nietrywialne fazy w osiągalnych doświadczalnie wartościach pola Zeemana. Odkrycia te dają obiecujące możliwości pogłębienia naszego zrozumienia i wykorzystania zjawisk topologicznych w nanoprzewodach SnTe oraz kontrolowania i tworzenia stanów zerowych Majorany poprzez manipulowanie polami łamiącymi symetrię inwersji (np. poprzez ferroelektryczność).

W drugim projekcie badawczym kierujemy naszą uwagę na badanie nietopologicznych stanów granicznych w materiałach będących potencjalnie kwantowymi spinowymi izolatorami Halla, takich jak heterostruktury HgTe/CdTe i InAs/GaSb. Udało się stwierdzić, że te wielowarstwowe struktury nie tylko zawierają topologicznie chronione helikalne stany brzegowe, ale także wykazują dodatkowe stany zlokalizowane na brzegu, które mogą mieć wpływ na rozpraszanie i transport, potencjalnie pogarszając jakość kwantowego spinowego efektu Halla. Wykorzystując obliczenia oparte na pierwszych zasadach, konstruujemy efektywny model ścisłego wiązania dla heterostruktur HgTe/CdTe, HgS/CdTe i InAs/GaSb i odkrywamy, że materiały te wykazują obecność dodatkowych stanów brzegowych, na które wpływa zakończenie brzegu. Mikroskopowe pochodzenie tych dodatkowych stanów brzegowych można prześledzić wstecz do minimalnego modelu, który zawiera płaskie

pasma i nietrywialną geometrię kwantową, co powoduje powstawanie ładunków polaryzacyjnych na brzegach. Ponieważ płaskie pasma oddziałują ze sobą i innymi stanami, podczas tworzenia hamiltonianu opisującego całą heterostrukturę, ładunki te manifestują się jako obserwowane dodatkowe stany brzegowe. Warto zauważyć, że w studniach kwantowych HgTe/CdTe dodatkowe stany brzegowe leżą daleko od poziomu Fermiego, czyniąc je nieaktywnymi w procesie transportu. Jednak w heterostrukturach HgS/CdTe i InAs/GaSb stany te pojawiają się w przerwie energetycznej, co pozwala na wielomodowy transport krawędziowy. Na koniec pokazujemy, że ponieważ te dodatkowe stany krawędziowe są nietopologiczne, możliwe jest wyeliminowanie ich z obszaru przerwy energetycznej poprzez modyfikację elektrostatycznego potencjału krawędziowego, na przykład za pomocą bramki bocznej lub domieszkowania chemicznego.

Badania przedstawione w rozprawie zostały opublikowane w dwóch artykułach naukowych:

- Nguyen, N. M.; Brzezicki, W., & Hyart, T. Corner states, hinge states, and Majorana modes in SnTe nanowires. **Phys.Rev.B.105.075310 (2022)**

- Nguyen, N. M.; Cuono, G.; Islam, R.; Autieri, C.; Hyart, T., & Brzezicki, W. Unprotected edge modes in quantum spin Hall insulator candidate materials, **PhysRevB.107.045138 (2023)**

Other publication:

- Campetella, M.; Baima, J.; Nguyen, N. M.; Maschio, L.; Mauri, F., & Calandra, M. Hybrid-functional electronic structure of multilayer graphene. **PhysRevB.101.165437 (2020)**

List of Abbreviations

QWZ Qi-Wu-Zhang

BHZ Bernevig-Hughes-Zhang

TRS Time-reversal symmetry

PHS Particle-hole symmetry

TRI Time-reversal invariant

AZ Altland-Zirnbauer

TIs Topological insulators

TSCs Topological superconductors

Contents

List of Figures

List of Tables

Motivation

T opological semiconductors are an emerging and active area of research in condensed matter physics and materials science. They are an exciting branch of topological materials, which exhibit unique electronic properties due to their non-trivial topology. The history of topological semiconductors can be traced back to the early 2000s when theoretical physicists began exploring the concept of topological insulators. These materials were characterized by an insulating bulk state but conducting surface states that were topologically protected, meaning they were robust against certain types of defects and disorder. In 2010, a landmark paper by M. Z. Hasan and C. L. Kane predicted the existence of 3D topological insulators [36]. Roughly at the same time, a research group led by Qi and Zhang proposed the concept of 2D topological insulators [68], which were later experimentally observed in quantum wells of HgTe/CdTe semiconductor structures. Although the general classification of topological insulators and superconductor is well-developed, many of the properties of the real world topological semiconductors are still poorly understood. Here we concentrate on two classes of topological semiconductors: (i) SnTe materials as an example of topological crystalline insulators, gapless topological phases, higher order topological phases and topological superconductors in the presence of induced superconductivity, and (ii) HgTe materials as an example of quantum spin Hall insulators exhibiting interplay of topological and non-topological edge modes.

Beginning with the pioneering theoretical work by Fu and Kane [38], it was predicted that SnTe could host a 3D topological insulator phase with symmetry-protected surface states. SnTe materials ($Sn_{1-x}Pb_xTe_{1-y}Se_y$) are renowned for being exemplary systems to study 3D topological crystalline insulators and phase transitions. This is because the band inversion can be controlled by adjusting the Sn content [28, 38, 88, 96]. However, their significance in future studies of topological effects could be even more profound. Experimental observations of robust 1D modes at the surface atomic steps [83] have been made and interpreted as topological flat bands, based on a model with chiral symmetry [72]. Additionally, these experiments suggest that these flat bands could give rise to correlated states and result in a robust zero-bias peak in tunneling conductance at low temperatures [59]. While there has been a temptation to interpret the zero-bias anomaly as evidence of topological superconductivity, all the observed phenomena can be explained without invoking superconductivity or Majorana modes [10, 11, 59]. On one hand, recent research on flat-band systems [54, 64] suggests that in thin films of SnTe materials, the tunability of density with gate voltages may enable the realization of both magnetism and

superconductivity at the step defects. On the other hand, there is a growing priority to enhance the manufacturing process of low-dimensional SnTe systems with controllable carrier density in which theoretical calculations indicate that thin SnTe multilayer systems have the potential to host a wide range of 2D topological phases, such as quantum spin Hall [51, 77] and 2D topological crystalline insulator phases [11, 52]. Recent experiments on thin films of SnTe materials show that their transport properties can be controlled by intentionally breaking the mirror symmetry [41]. SnTe materials hold promise for the exploration of higher-order topology [39, 80]. Consequently, it will pave the way for investigating to investigate the hinge and corner states in these systems.

Moreover, both theoretical and experimental research on superconductivity has revealed that it can be induced either through the proximity effect or by introducing In-doping, suggesting the occurrence of diverse and intricate physics as a result [4, 8, 29, 47, 70, 78, 92, 97]. Time-reversal symmetry breaking is also expected to give rise to interesting topological phases. For example, a Zeeman magnetic field can be applied externally with high efficiency due to the significant g factor, approximately $g \sim 50$ [25, 63], or it can be introduced through magnetic dopants [62, 85, 86]. Although the topological properties of SnTe nanowires have received little experimental attention thus far, the situation is expected to soon change because of ongoing progress in their fabrication [53, 76]. Taking inspiration from these reasons, we have conducted a comprehensive investigation of the symmetries and topological properties in SnTe nanowires, while also utilizing adjustable symmetry-breaking fields to achieve various types of topological states.

Expanding on the discovery of topological states in SnTe, we aim to deepen our understanding by investigating the non-topological states associated with the quantum spin Hall effect. The theory of the quantum spin Hall effect was initially proposed independently by Kane and Mele in 2005 [40] and by Bernevig, Hughes, and Zhang in 2006 [6]. They predicted that specific 2D materials with strong spin-orbit coupling could exhibit a unique electronic behavior, where electrons with opposite spins move in opposite directions along the material's edges, creating dissipationless conduction channels. However, this phenomenon has been known to exhibit surprisingly poor quantization of conductance, especially when compared to the ordinary quantum Hall effect. Various theories have been proposed to elucidate this behavior. Notably, by introducing impurity doping in InAs/GaSb bilayers [24] and employing gate training in HgTe/CdTe quantum wells [56], the quality of edge transport can be enhanced. These findings imply the presence of additional low-energy states without topological protection, influenced by specific sample preparation techniques, which might contribute to the breakdown of topological protection. In certain experiments, for instance in InAs/GaSb bilayers without impurity doping additional edge modes seem to contribute to transport [61] or in HgTe/CdTe quantum wells, where the additional states are distant from the Fermi level and do not significantly impact transport, their dynamic properties suggest involvement in scattering [18]. The microscopic origin of these additional states in both materials is still unknown.

In our second project, we show another possibility of having additional edge states which were overlooked by the simple theories, whose number is proportional to the thickness of the system. Our studies are based on tight-binding models derived from the ab-initio calculations and analytical results for emergent symmetries, geometric phases and the end-states of the minimal model. We show in details how the minimal model can be derived from the full one by appropriate projections and how the end-states of the minimal model become the edge-states of the original system.

Outline of the thesis

This thesis is divided into two parts. In the first part of the dissertation, we first review the classification of strong topological insulators and superconductors topological crystalline insulators, gapless topological phases and higher order topological phases.

- In Chapter 1, we provide a concise review of nonspatial symmetries and the classification of strong topological insulators and superconductors. Subsequently, we demonstrate calculations for the Qi-Wu-Zhang (QWZ) and Bernevig-Hughes-Zhang (BHZ) models, exemplifying quantum spin Hall insulators, and the Kitaev model, representing topological superconductivity.

- Chapter 2 begins with an exploration of topological crystalline insulators, emphasizing the significance of spatial symmetries, particularly mirror symmetry. We then delve into the SnTe model, where we compute the topological invariant and delve into the examination of topological phases.

- In Chapter 3, we draw motivation from the gapless phase observed in the BHZ model in Chapter 1 and establish foundational knowledge before delving into Chapter 5. This chapter focuses on the classification of gapless topological phases, and we showcase calculations for the nodal superconductor and the gapless Weyl semimetal.

- Lastly, Chapter 4 will explore higher-order topological phases where we elucidate the concept of topologically nontrivial phases and proceed to construct simple models for second-order topological insulators and superconductors, relying on a single mirror symmetry.

The second part of the dissertation provides a summary of the most significant results obtained in the articles: (i) Corner states, hinge states, and Majorana modes in SnTe nanowires (in chapter 5), and (ii) Unprotected edge modes in quantum spin Hall insulator candidate materials (in chapter 6). Finally, we present the conclusion and outlook to conclude the thesis.

Chapter 1

Strong topological insulators and superconductors

Topological insulators are insulating in the bulk and theory predicts the unique physical properties which guarantees the existence of low-energy states located at their boundaries [33, 34, 36, 67, 68, 90]. Although the best known example of a topological phase is the integer quantum Hall state, in which protected chiral edge states give rise to a quantized transverse Hall conductivity in the presence of magnetic field breaking the time-reversal symmetry, was discovered in 1980 [45], the first successful theoretical proposal of time-reversal invariant topological insulators was publish in the early 2000s [6] and followed by several experiments [24, 46, 95]. We start this Chapter by reviewing symmetries in quantum systems and discussing the topological classification of fully gapped free-fermion systems in terms of nonspatial symmetries, namely, time-reversal symmetry (TRS), particle-hole symmetry (PHS), and chiral symmetry which define a total of ten symmetry classes. In this Chapter, we introduce one of the most important thing there is about a topological system. Namely, the bulk-boundary correspondence. The bulk-boundary correspondence of a topological system is what allow the edge of the system to develop unique properties which only exist because of the topologically nontrivial bulk. The first example will be the Bernevig-Hughes-Zhang (BHZ) model [6] for a two-dimensional topological insulator where we compute the phase diagrams in the presence of various additional symmetries and obtain the bulk-boundary correspondence by establishing the relation between the Chern number and the number of gapless edge modes. We find that these system fall into two categories: trivial insulator (even number of pairs of edge states at a single edge) and the topological phase (odd number of pairs of edge states at a single edge). Finally, we also introduce the Kitaev model as an example of topological superconductivity and Majorana modes. This Chapter mainly follow the review paper [16] and lecture notes [3].

1.1 Nonspatial symmetries and classification of strong topological insulators and superconductors

In this section, we classify fully gapped free-fermion systems in terms of topology in the presence of nonspatial symmetries, namely, time-reversal symmetry (TRS),

particle-hole symmetry (PHS), and chiral symmetry which define a tenfold classification table [75, 82].

We consider a quantum systems in which $\left\{c_i, c_i^\dagger\right\}_{i=1...N}$ define a set of fermion annihilation or creation operators which satisfy the canonical anticommutation relation $\left\{c_i, c_j^\dagger\right\} = \delta_{ij}$. Here we set our notation asscociated with the lattice sites, so i, j are combination of lattice sites ($I, J = 1...M$) and the additional quantum number for example orbital and spin quantum number: $s, p_x, p_y, p_z, \sigma \ldots$. The Pauli matrices:

$$\sigma_x = \begin{pmatrix} 0 & 1 \\ 1 & 0 \end{pmatrix}, \ \sigma_y = \begin{pmatrix} 0 & i \\ -i & 0 \end{pmatrix}, \ \sigma_z = \begin{pmatrix} 1 & 0 \\ 0 & -1 \end{pmatrix}, \tag{1.1}$$

complex matrices which are Hermitian, involutory and unitary. The "second quantization" tight-binding Hamiltonian in most of the condensed matter physics context, can be represented as:

$$\hat{H}(\mathbf{k}) = \sum_\mathbf{k} \sum_{i,j} \mathrm{H}_\mathbf{k}^{ij} c_i^\dagger c_j \tag{1.2}$$

The system states can be represented as an vector live in the Hilbert space. This can be more compactly expressed using the vector notation Δ.

$$c = \begin{pmatrix} c_1 \\ c_2 \\ \vdots \\ c_N \end{pmatrix} \tag{1.3}$$

We examine the ways in which various symmetries are applied in fermionic systems. In accordance with Wigner's symmetry representation theorem, any symmetry transformation can be expressed by an linear and unitary, or antilinear and antiunitary operator in the Hilbert space and their action on the fermionic states:

$$c \rightarrow c' = \mathrm{U}c, \tag{1.4}$$

and matrices change as $\mathrm{H}' = \mathrm{U}\mathrm{H}\mathrm{U}^{-1}$. If the system obeys a unitary symmetry then U and H commute $[\mathrm{U}, \mathrm{H}] = 0$. If a unitary operator $\mathcal{U}$ act on the spatial part of the eigenvector ψ (lattice sites $I = 1, \ldots M$) then it is called spatial or if it does not act on the spatial part it is nonspatial symmetry which we will focus in this section.

1.1.1   Time-reversal symmetries

For systems that can be realized experimentally, time-reversal is the most significant discrete symmetry. Until the beginning of this century, physicist thought that only system without the TRS can exhibit interesting effects such as the quantized Hall voltage. But thanks to the research of Kane and Mele initiating the study of topological band theory since 2005, it has been known that the systems with TRS could also have significant topological phenomena originating from a $\mathbb{Z}_2$ topological invariant [40]. The TRS operator is an antiunitary operator which has the general

form

$$\mathcal{T} = \mathrm{T}\mathcal{K} \tag{1.5}$$

Which contains the unitary part, T and the complex-conjugation part $\mathcal{K}$. Its action on the Hamiltonian is:

$$\mathcal{T}\mathrm{H}_{\mathbf{k}}\mathcal{T}^{-1} = \mathrm{H}_{-\mathbf{k}}$$
$$\mathrm{T}\mathrm{H}_{\mathbf{k}}\mathrm{T}^{\dagger} = \mathrm{H}_{-\mathbf{k}}^{\intercal} \tag{1.6}$$

Typically $T = \sigma_y$, where σ_y is Pauli matrix acting on the spin, meaning that the time-reversal operation does not affect the position coordinate but it flips the sign of momentum and spin.

Kramers' Theorem

One of the most important consequence of TRS is Kramers' theorem which states that for every energy eigenstate of a time-reversal symmetric system with half-integer total spin and $\mathcal{T}^2 = -1$[1], there is at least another eigenstate with the same energy.

Proof: Consider a TR symmetric system which means $[\mathcal{T}, \mathrm{H}_{\mathbf{k}}] = 0$. Then any eigenstate $\psi_{\mathbf{k}}$ of $\mathrm{H}_{\mathbf{k}}$ with energy eigenvalue $E_{\mathbf{k}}$ has a TRS partner $\mathcal{T}\psi_{\mathbf{k}}$ which is an eigenstate of $\mathrm{H}_{-\mathbf{k}}$ with the same energy. This proof is sufficient for all states within the Brillouin zone, except for time-reversal invariant momenta (TRI) where $\tilde{\mathbf{k}} = \{k_i\}_{i=1,\cdots,d}, k_i = (0, \pi)$, as these time-reversal symmetric (TRS) pairs reside at different momenta. If we could proof that these partner states orthogonal then the spectrum is indeed doubly degenerate. To demonstrate this, we use the fact that the unitary part of TRS is anti-symmetric: $\mathcal{T}^2 = -1 \Leftrightarrow \mathrm{T}\mathcal{K}\mathrm{T}\mathcal{K} = -1 \Leftrightarrow \mathrm{T}\mathrm{T}^* = -1 \Leftrightarrow \mathrm{T} = -\mathrm{T}^{\intercal}$

$$\langle\psi|\mathcal{T}\psi\rangle = \sum \psi_i^* \mathrm{T}_{ij}\mathcal{K}\psi_j = \sum \psi_i^* \mathrm{T}_{ij}\psi_j^* = \sum \psi_j^*(-\mathrm{T}_{ji})\psi_i^*$$
$$= \sum \psi_j^*(-\mathrm{T}_{ji})\mathcal{K}\psi_i = -\langle\psi|\mathcal{T}\psi\rangle = 0. \tag{1.7}$$

Thus, at high symmetry points in the Brillouin zone at the time-reversal invariant momenta (TRI), the TRS map two orthogonal eigenstates onto each other and they have the same energy. Such states are called Kramer's doublet. From Eq(1.6).

$$\mathcal{T}\mathrm{H}_{\tilde{\mathbf{k}}}\mathcal{T}^{-1} = \mathrm{H}_{\tilde{\mathbf{k}}} \tag{1.8}$$

for d-dimensional system, we have 2^d high symmetry points. For instance, in one-dimensional system, one point is the center $\tilde{\mathbf{k}} = 0$ and the other point is at the border $\tilde{\mathbf{k}} = \pi$.

---

[1]It is a very important condition to proof Kramers' Theorem because for $\mathcal{T}^2 = 1$ case, the two TRS partners may belong to same band.

1.1.2 Particle-hole symmetries

Particle hole symmetry, also known as charge conjugation, is a anti-unitary transformation that swap fermion's creation and annihilation operators and their action on the Hamiltonian:

$$\mathcal{P} = P\mathcal{K} \tag{1.9}$$

$$\mathcal{P}H_{\mathbf{k}}\mathcal{P}^{-1} = -H_{-\mathbf{k}} \tag{1.10}$$

$$PH_{\mathbf{k}}P^{\dagger} = -H_{-\mathbf{k}}^{\intercal} \tag{1.11}$$

Similar with the TRS if $H_{\mathbf{k}}|\psi_{\mathbf{k}}\rangle = E_{\mathbf{k}}$ is eigenstate then is PH partner $\mathcal{P}|\psi_{\mathbf{k}}\rangle$ is also an eigenstate but with energy $-E_{\mathbf{k}}$. *Proof:*

$$\mathcal{P}H_{\mathbf{k}}|\psi_{\mathbf{k}}\rangle = \mathcal{P}E_{\mathbf{k}}|\psi_{\mathbf{k}}\rangle$$
$$\mathcal{P}H_{\mathbf{k}}\mathcal{P}^{-1}\mathcal{P}|\psi_{\mathbf{k}}\rangle = E_{\mathbf{k}}\mathcal{P}|\psi_{\mathbf{k}}\rangle$$
$$-H_{-\mathbf{k}}\mathcal{P}|\psi_{\mathbf{k}}\rangle = E_{\mathbf{k}}\mathcal{P}|\psi_{\mathbf{k}}\rangle$$
$$H_{-\mathbf{k}}\left(\mathcal{P}|\psi_{\mathbf{k}}\rangle\right) = -E_{\mathbf{k}}\left(\mathcal{P}|\psi_{\mathbf{k}}\rangle\right). \tag{1.12}$$

1.1.3 Chiral symmetries

When the system has both particle-hole and time-reversel symmetries we can combined to obtains the chiral symmetry, $\mathcal{S} \sim \mathcal{TP} \sim \mathrm{TP}$. Notice in some case the hamiltonian can have chiral symmetry while the both the TRS and PHs broken.

$$\mathcal{S}H_{\mathbf{k}}\mathcal{S}^{\dagger} = -H_{\mathbf{k}} \text{ or } \{\mathcal{S}, H_{\mathbf{k}}\} = 0 \tag{1.13}$$

As a consequence, spectrum of chiral symmetric system will be symmetric around $E = 0$ due to the fact that the eigenvector $|\psi_{\mathbf{k}}\rangle$ of H with energy $E_{\mathbf{k}}$ always have their chiral partner $\mathcal{S}|\psi_{\mathbf{k}}\rangle$ eigenstates with opposite energy $-E_{\mathbf{k}}$.

$$\mathcal{S}H_{\mathbf{k}}|\psi_{\mathbf{k}}\rangle = \mathcal{S}E_{\mathbf{k}}|\psi_{\mathbf{k}}\rangle$$
$$\mathcal{S}H_{\mathbf{k}}\mathcal{S}^{\dagger}\mathcal{S}|\psi_{\mathbf{k}}\rangle = E_{\mathbf{k}}\mathcal{S}|\psi_{\mathbf{k}}\rangle$$
$$-H_{\mathbf{k}}\left(\mathcal{S}|\psi_{\mathbf{k}}\rangle\right) = E_{\mathbf{k}}\left(\mathcal{S}|\psi_{\mathbf{k}}\rangle\right)$$
$$H_{\mathbf{k}}\left(\mathcal{S}|\psi_{\mathbf{k}}\rangle\right) = -E_{\mathbf{k}}\left(\mathcal{S}|\psi_{\mathbf{k}}\rangle\right). \tag{1.14}$$

Chiral symmetric hamiltonian spectrum with odd degrees of freedom has flat-band at zero energy. Altogether $\mathcal{T}$, $\mathcal{P}$ and $\mathcal{S}$ define a total of ten symmetry classes which were originally described by Altland and Zirnbauer [2, 101] (AZ symmetry classes).

In the next subsections we will consider some relevant examples of strong topological insulators and topological superconductors in more detail.

Class	Symmetry			Dimension							
	$\mathcal{T}$	$\mathcal{P}$	$\mathcal{S}$	0	1	2	3	4	5	6	7
A	0	0	0	$\mathbb{Z}$	0	$\mathbb{Z}$	0	$\mathbb{Z}$	0	$\mathbb{Z}$	0
AIII	0	0	1	0	$\mathbb{Z}$	0	$\mathbb{Z}$	0	$\mathbb{Z}$	0	$\mathbb{Z}$
AI	1	0	0	$\mathbb{Z}$	0	0	0	$2\mathbb{Z}$	0	$\mathbb{Z}_2$	$\mathbb{Z}_2$
BDI	1	1	1	$\mathbb{Z}_2$	$\mathbb{Z}$	0	0	0	$2\mathbb{Z}$	0	$\mathbb{Z}_2$
D	0	1	0	$\mathbb{Z}_2$	$\mathbb{Z}_2$	$\mathbb{Z}$	0	0	0	$2\mathbb{Z}$	0
DIII	-1	1	1	0	$\mathbb{Z}_2$	$\mathbb{Z}_2$	$\mathbb{Z}$	0	0	0	$2\mathbb{Z}$
AII	-1	0	0	$2\mathbb{Z}$	0	$\mathbb{Z}_2$	$\mathbb{Z}_2$	$\mathbb{Z}$	0	0	0
CII	-1	-1	1	0	$2\mathbb{Z}$	0	$\mathbb{Z}_2$	$\mathbb{Z}_2$	$\mathbb{Z}$	0	0
C	0	-1	0	0	0	$2\mathbb{Z}$	0	$\mathbb{Z}_2$	$\mathbb{Z}_2$	$\mathbb{Z}$	0
CI	1	-1	1	0	0	0	$2\mathbb{Z}$	0	$\mathbb{Z}_2$	$\mathbb{Z}_2$	$\mathbb{Z}$

TABLE 1.1: Tenfold classification table for topological insulators and superconductors [75]. The first column is the notation of ten symmetry classes of fermionic Hamiltonians. In the case of TRS and PHS, the symmetry class is characterized by the presence and $\mathcal{T}^2(\mathcal{P}^2) = \pm 1$ values, or absence (denoted as 0). However, for chiral symmetry, it depends solely on whether it is present (denoted as 1) or absent (denoted as 0). The symbols $\mathbb{Z}$, $\mathbb{Z}_2$, $2\mathbb{Z}$, and 0 denote the existence or absence of nontrivial topological insulators (TIs), superconductors (TSCs), or topological defects, and if present, indicate the specific categories of these states.

1.2 Qi-Wu-Zhang and Bernevig-Hughes-Zhang models

In this section, we introduce a classic example of two-dimensional topological insulator Qi-Wu-Zhang (QWZ) model [67] (initially used to explain the Quantum anomalous Hall Effect) and then quantum spin Hall insulator, known as Bernevig-Hughes-Zhang (BHZ) model [6] for a time-reversal invariant insulator system.

The bulk momentum-space Hamiltonian of QWZ model describes two-dimensional insulators

$$\mathrm{H}_{\mathbf{k}}^{QWZ} = \sin k_x \sigma_x + \sin k_y \sigma_y + [\cos k_x + \cos k_y + u]\,\sigma_z, \qquad (1.15)$$

where u is the sublattice potential, also known as the mass term, because it bears analogy to relativistic dispersion[2]. The topological properties in this case are characterised by the Chern number, an important topological invariant for two-dimensional electron systems. We briefly show the way to compute the Chern number and how it can predict the real-space edge-state channels behaviour. Theoretically, the Chern number for the nth occupied band $|\psi_n\rangle$ is given by:

$$C^{(n)} = -\frac{1}{2\pi} \int_{\text{Brillouin zone}} \left(\frac{\partial A_y^{(n)}}{\partial k_x} - \frac{\partial A_x^{(n)}}{\partial k_y} \right) dk_x dk_y \qquad (1.16)$$

---

[2]Notice that after expansion of (1.15) around $k = 0$ and denoting $u = u + \delta u$, the dispersion is $E = \pm\sqrt{k_x^2 + k_y^2 + (\delta u)^2}$, so that δu is analogous to the mass of relativistic particles.

in which $A_j^{(n)} = -i\langle\psi_n|\partial_{k_j}|\psi_n\rangle$, $j = x, y$, is known as Berry connection. In general, for the two band system, one needs to compute the eigenstate for the only occupied band. On the other hand, for a finite system two-dimensional Hilbert space of quantum states with points labelled by $n, m \in \mathbb{Z}$, for an elementary square of the grid the Berry flux is:

$$\text{F}_{(n,m)} = -\arg\left[\langle\psi_{n,m}|\psi_{n+1,m}\rangle\langle\psi_{n+1,m}|\psi_{n+1,m+1}\rangle\langle\psi_{n+1,m+1}|\psi_{n,m+1}\rangle\langle\psi_{n,m+1}|\psi_{n,m}\rangle\right],$$
(1.17)

and the sum of the Berry flux, over all the elementary squares in the Brillouin zone, gives us value of Chern number:

$$C = \frac{1}{2\pi}\sum_{n,m}\text{F}_{(n,m)}.$$
(1.18)

Because the Berry flux is gauge invariant it means that the Chern number itself is gauge invariant. Moreover, we can also use this formula as numerical technique for a finite-resolution grid of k_x, k_y points in the Brillouin zone. Therefore, the Chern number of a chosen band can be computed using this discrete definition (1.18). As the mass term parameter u changes, there exists three qualitatively different behaviors:

iors: $\begin{cases} |u| > 2, C = 0, & \text{trivial} \\ -2 < u < 0, C = -1, & \text{non-trivial} \\ 0 < u < 2, C = 1, & \text{non-trivial} \end{cases}$

We then go to the real space Hamiltonian for the QWZ model to confirm the bulk-boundary correspondence. This means that now just k_y is a good quantum number and the eigenstates in the k_x direction are quantized. As Fig. 1.1 (d) depicts, in the trivial regime, $C = 0$, the one-dimensional spectrum is gapped (the system is a trivial insulator). However, when the sublattice potential $-2 < u < 2$, there are energy eigenstates that are localized on the edge of the system connecting between the positive and negative bands. As Fig. 1.1 (b) shown, electrons move in the positive direction in real space on the left edge and negative direction on the right edge when $C = -1$ and vice versa in Fig. 1.1 (c) when $C = 1$.

After discussing the QWZ model, we next introduce the description for the BHZ model or time-reversal invariant two dimensional insulator. It can be written in matrix form as [6]:

$$\text{H}_{\mathbf{k}}^{BHZ} = \begin{pmatrix} \text{H} & \Delta \\ \Delta^\dagger & \text{H}^* \end{pmatrix}$$
(1.19)

or expanded with the help of Pauli matrices as (notice that both are in momentum space)

$$\text{H}_{\mathbf{k}}^{BHZ} = \sigma_0 \otimes [(u + \cos k_x + \cos k_y) \cdot \sigma_z + \sin k_y \cdot \sigma_y] + \sigma_x \otimes \Delta + \sigma_z \otimes \sin k_x \sigma_x.$$
(1.20)

This means that starting from QWZ Hamiltonian Eq.(1.15), we duplicate the system, take the complex conjugate of one of the subsystems, $\text{H}^* = \text{KHK}$, and allow
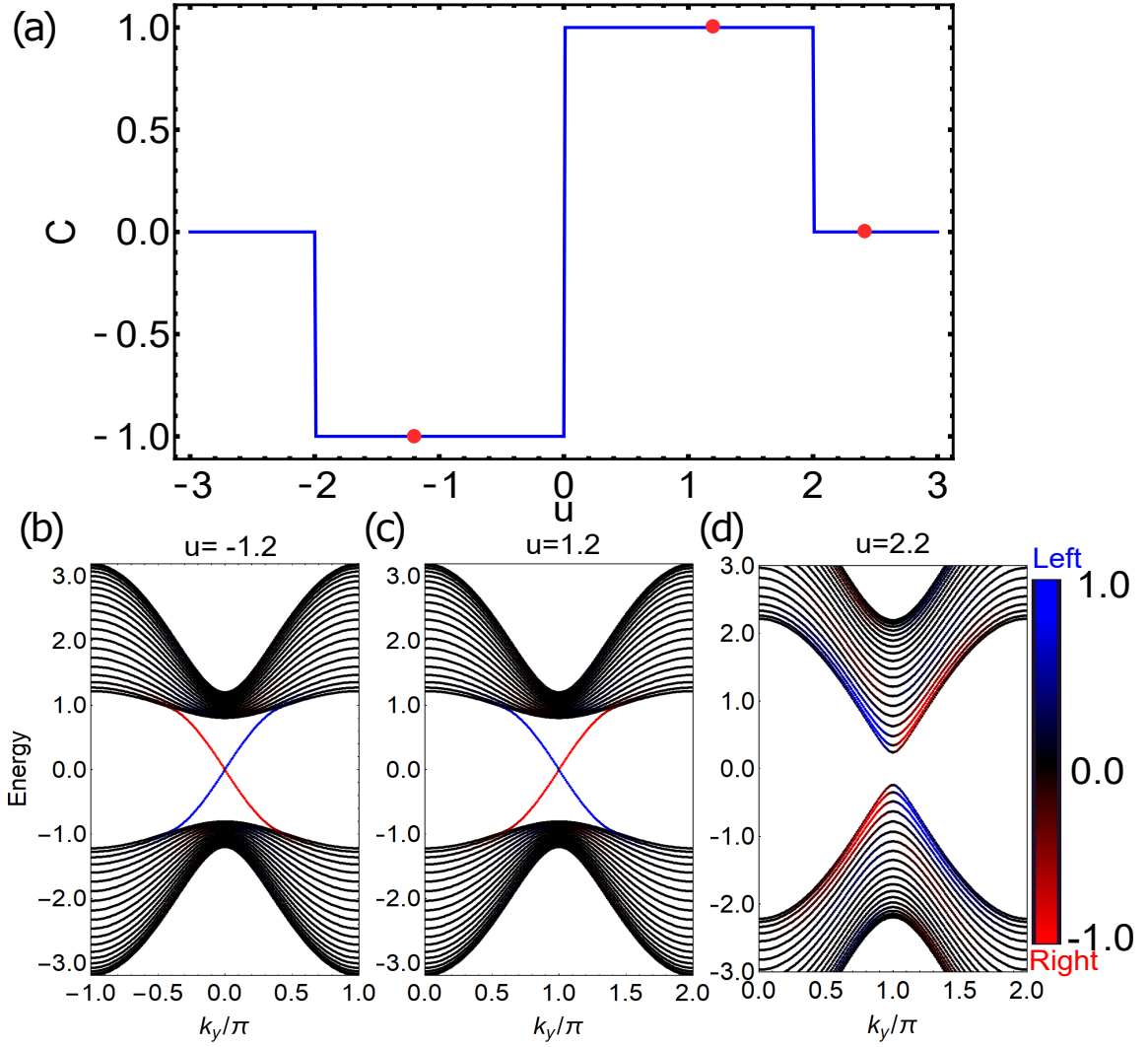
FIGURE 1.1: (a) Topological phase diagram of QWZ Hamiltonian (1.15) as function of mass term u. Red dots are discrete values of u in which the one-dimensional spectra are computed in (b),(c) and (d) with system width $N = 20$ unit cells. Blue/Red color indicate the projection of the eigenstates onto the first/last unit cells located at the left (blue) and right (red) edge of the system. (b) Spectrum of the non-trivial phase at $u = -1.2$ with Chern number $C = -1$ (c) Spectrum of the non-trivial phase at $u = +1.2$ with Chern number $C = +1$ (d) Spectrum of the non-trivial phase at $u = 2.4$ with Chern number $C = 0$.

a specific form of coupling Δ between the subsystems [3]. The coupling term Δ is a Hermitian operator acting on the internal degree of freedom (ex: orbital, spin..). The last piece of the picture would be the effect of these couplings on the system, particularly on the edge modes. Consider two cases of TRS.

$$\mathcal{T}_1 = \sigma_x \otimes \mathbb{1}_2 \, \text{K} \qquad\qquad\qquad \mathcal{T}_1^2 = 1 \qquad\qquad (1.21)$$

$$\mathcal{T}_2 = i\sigma_y \otimes \mathbb{1}_2 \, \text{K} \qquad\qquad\qquad \mathcal{T}_2^2 = -1 \qquad\qquad (1.22)$$

where $\mathbb{1}_2$ are 2×2 identity matrices and their action on the Hamiltonian reads

$$\mathcal{T}_1 H'_\mathbf{k} \mathcal{T}_1^{-1} = \begin{pmatrix} 0 & 1 \\ 1 & 0 \end{pmatrix} \begin{pmatrix} H^* & \Delta^* \\ \Delta^\intercal & H \end{pmatrix} \begin{pmatrix} 0 & 1 \\ 1 & 0 \end{pmatrix} = \begin{pmatrix} H & \Delta^\intercal \\ \Delta^* & H^* \end{pmatrix} \qquad (1.23)$$

$$\mathcal{T}_2 H'_\mathbf{k} \mathcal{T}_2^{-1} = \begin{pmatrix} 0 & 1 \\ -1 & 0 \end{pmatrix} \begin{pmatrix} H^* & \Delta^* \\ \Delta^\intercal & H \end{pmatrix} \begin{pmatrix} 0 & -1 \\ 1 & 0 \end{pmatrix} = \begin{pmatrix} H & -\Delta^\intercal \\ -\Delta^* & H^* \end{pmatrix} \qquad (1.24)$$

And from Eq.(1.6), the requirements for the system to have time-reversed symmetric with $\mathcal{T}_1^2 = 1$ if $\Delta = \Delta^\intercal$ are symmetric and with $\mathcal{T}_2^2 = -1$ if $\Delta = -\Delta^\intercal$ are anti-symmetric. If we set $\Delta = 0$ the BHZ model is the direct sum of two QWZ Hamiltonians with opposite Chern numbers. Fig. 1.2(a) shows that the spectrum of the uncoupled systems is just the sum of two opposite Chern number-QWZ models with two opposite-propagating edge state branches on each edge (Each branch of propagating edge states is similar to Fig. 1.1 (b)-(c)) and they connected by time-reversed transformation. In typical physical realization the subsystems correspond to spin $\uparrow$ and spin $\downarrow$. Therefore, in the following the subsystems will be called spin sectors.

Let's now consider the case where the spin sectors are coupled. First for the $\Delta \sim \sigma_x$ which obeys the time-reversal symmetry $\mathcal{T}_1$ satisfying $\mathcal{T}_1^2 = 1$ (and breaks the $\mathcal{T}_2$ symmetry), an anti-crossing is observed in the edge-states dispersion relations, as in Fig.1.2(b), because particles now can move between subsystems on the same edge which have opposite propagating direction or in other words, counter-propagating edge states on the same edge are now coupled. The system is not topological insulator based on Table. 1.1. On the other hand when $\Delta \sim \sigma_y$, the coupling between the spin sectors causes the bands support a nontrivial pseudospin texture $\langle\vec{\tau}\rangle_n = \langle\psi_n|\vec{\tau}|\psi_n\rangle$ the pseudospin operators where $\tau_{x,y,z}$ are the Pauli matrices acting in each spin sector space. As illustrated in Fig. 1.2 (c) the spin direction[4] depends on the momentum whereas pseudospin texture is trivial in case $\Delta = 0$, as shown in Fig. 1.2 (a). Because the antisymmetric coupling obeys $\mathcal{T}_2$, the two counter-propagating modes still have opposite spins at each momentum, so that there is no anti-crossing happening as long as the coupling is not strong enough to close the bulk gap as depicted in Fig.1.2(c).

---

[3]These two diagonal-block have opposite Chern number.

[4]the pseudospin direction rotates in two-dimensional $(\langle\tau_x\rangle_n, \langle\tau_z\rangle_n)$ plane because the pseudospin component $\langle\tau_y\rangle_n$ is negligible
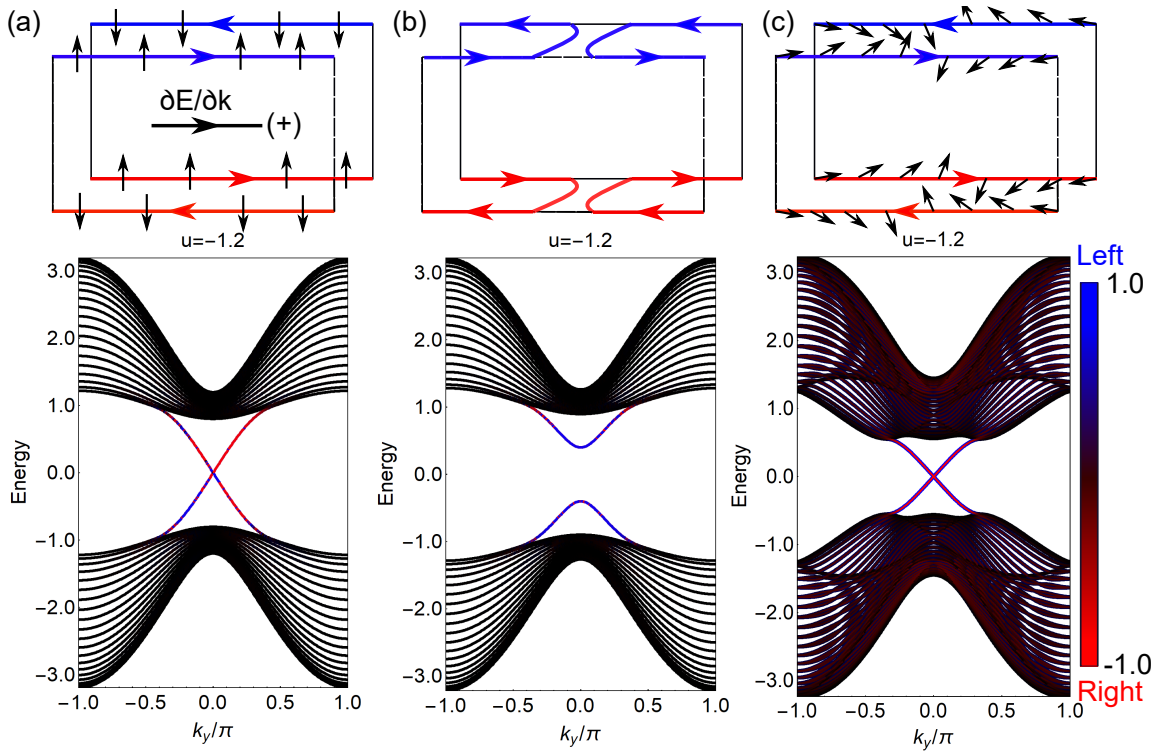
FIGURE 1.2: One-dimensional energy spectra of the BHZ model with stripe width $N = 20$. Here we set the sublattice potential $u = -1.2$. Blue/Red color indicate the projection of the eigenstates onto the first/last unit cells located at the left (blue) and right (red) edge of the system. (a) $\Delta = 0$ uncoupled layers. (b) $\Delta = 0.4\sigma_x$, symmetric coupling cause the low-energy bands to form an anti-crossing. (c) $\Delta = 0.4\sigma_y$ anti-symmetric coupling where we observe a non-trivial pseudospin texture in contrast with (a).

Similarly, as in the QWZ case, it is natural to compute the phase diagram for two cases $\Delta = 0$ and $\Delta \sim \sigma_y$. In case of no coupling system, the Hamiltonian (1.20) has inversion symmetry $I = \mathbb{1}_2 \otimes \sigma_z$, $I \cdot H_{\mathbf{k}} \cdot I^\dagger = H_{-\mathbf{k}}$ and $[I, \mathcal{T}_2] = 0$. Therefore, the eigenstates of TRS are also eigenstates of inversion symmetry. Consider time-reversal invariant momenta (TRI), eigenstate $|\psi_{\tilde{\mathbf{k}}}\rangle$ and its Kramer partner $\mathcal{T}_2|\psi_{\tilde{\mathbf{k}}}\rangle$ are orthogonal, as proved in (1.7), and share the same inversion eigenvalue. The $\mathbb{Z}_2$ bulk topological invariant is the parity of all occupied Kramers pairs 's inversion eigenvalues at all the time-reversal invariant momenta $\theta\left(\tilde{\mathbf{k}}\right)$, $\tilde{\mathbf{k}}_j = (0,0), (0,\pi), (\pi,0), (\pi,\pi)$.

$$-1^N = \prod_{i,j} \theta_i\left(\tilde{\mathbf{k}}_j\right), \tag{1.25}$$

where i are the Kramer pairs indices. In this case we just have one occupied Kramer pair.

As shown in Fig.1.3, if $|u| > 2$, the parity of the eigenvalues is 1, so $N = 0$ and the system is in the trivial regime, while the topological insulator phase appears when $-2 < u < 2$ because the parity is -1 and $N = 1$. Finally, when adding the inversion breaking term, the anti-symmetric coupling $\Delta \sim \sigma_y$, the calculation of $\mathbb{Z}_2$ invariant now is not quite straightforward. Based on the work of Kane and Mele [40], from occupied band wave functions we calculate the Pfaffian:

$$P\left(\mathbf{k}\right) = Pf[\langle\psi_{\mathbf{k}}|\mathcal{T}_2|\psi_{\mathbf{k}}\rangle]. \tag{1.26}$$

Then the bulk topological invariant can be obtained by counting the number of pairs of complex zeros of P which can be computed from expression:

$$I = \frac{1}{2\pi i} \int_F d\mathbf{k} \cdot \nabla_{\mathbf{k}} ln\left[P\left(\mathbf{k}\right) + i\delta\right], \tag{1.27}$$

the path F is defined so that it contains half of the complex zeros of the Pfaffian. In this case we chose a loop around half of the Brillouin zone. The nontrivial phase is determined by $\mathbb{Z}_2$, defined as $I \mod 2$, as shown in Fig. 1.4 (a). Additionally, we demonstrate that the closing of the bulk gap indicates a phase transition by calculating the bulk gaps as a function of the mass term u, as depicted in Fig. 1.4 (b)-(d). The bulk-boundary correspondence is illustrated in Fig. 1.5 (a)-(b), where the topological phase exhibits gapless edge modes, while the trivial insulator does not. Finally, as we conclude this Chapter, it is worth noting that the system also contains gapless topological phases, as depicted in Fig.1.4 (d) and Fig.1.5 (c). A more detailed exploration of these phases will be undertaken in Chapter 3.

Parity of Kramers pairs

The TRS $\mathcal{T}_2^2 = -1$ provides us a further restriction on the number of edge states under an adiabatic deformation of the BHZ Hamiltonian which will define a topological invariant. Consider a single edge of the system described by a one-dimensional Hamiltonian along $k_{x/y} : -\pi \to \pi$. At any given energy the spectrum has to be
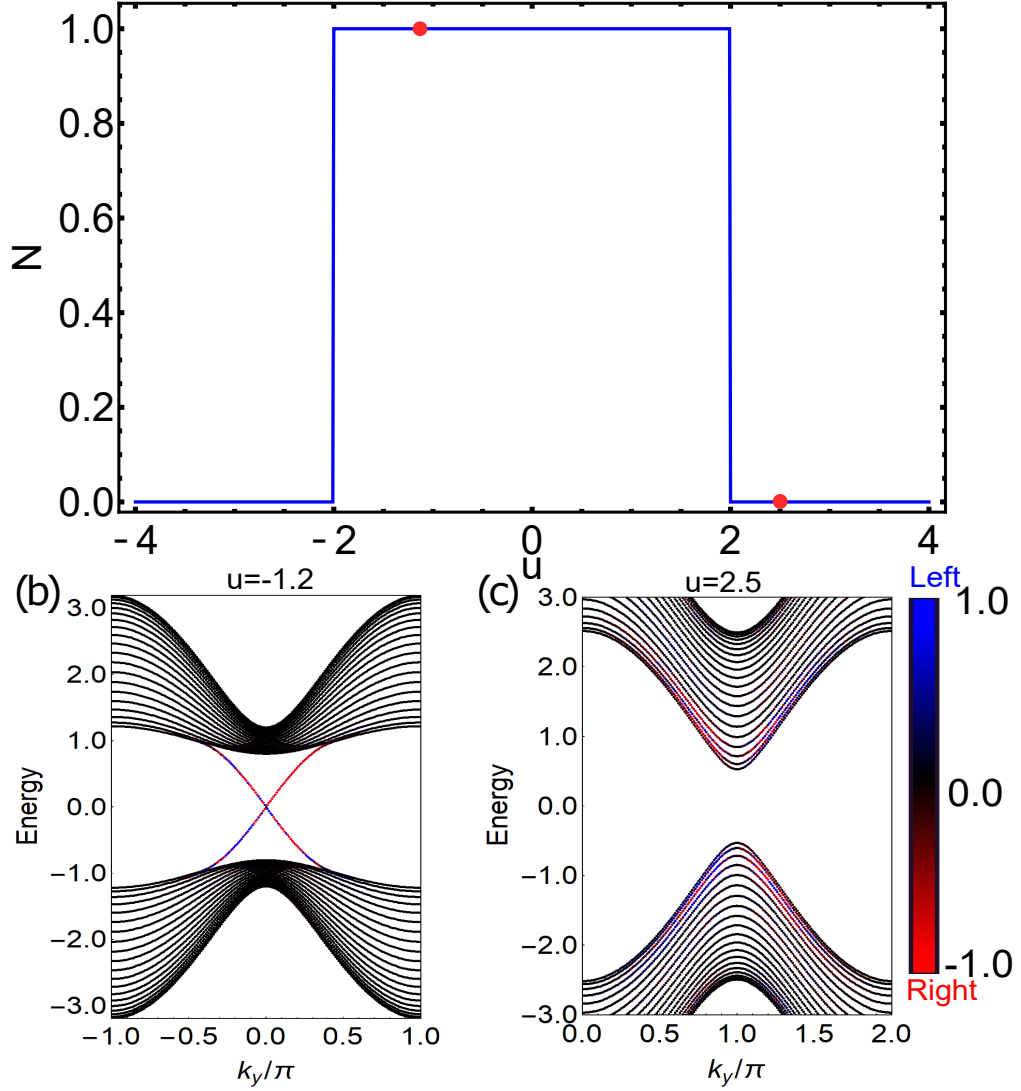
FIGURE 1.3: (a) Topological phase diagram of BHZ Hamiltonian (1.20) with no coupling between two layers $\Delta = 0$ as functions of mass term u. Red dots are discrete values of u in which the one-dimensional spectra with system width $N = 20$ unit cells are computed in (b) and (c). Blue/Red color indicate the projection of the eigenstates onto the first/last unit cells located at the left (blue) and right (red) edge of the system. (b) Spectrum of the non-trivial phase at $u = -1.2$ with bulk invariant $N = 1$. At low energy, on each side of the strip, there are two edge states connecting through the gap and propagating in opposite directions. (c) Spectrum of the trivial phase at $u = 2.5$ with bulk invariant $N = 0$.
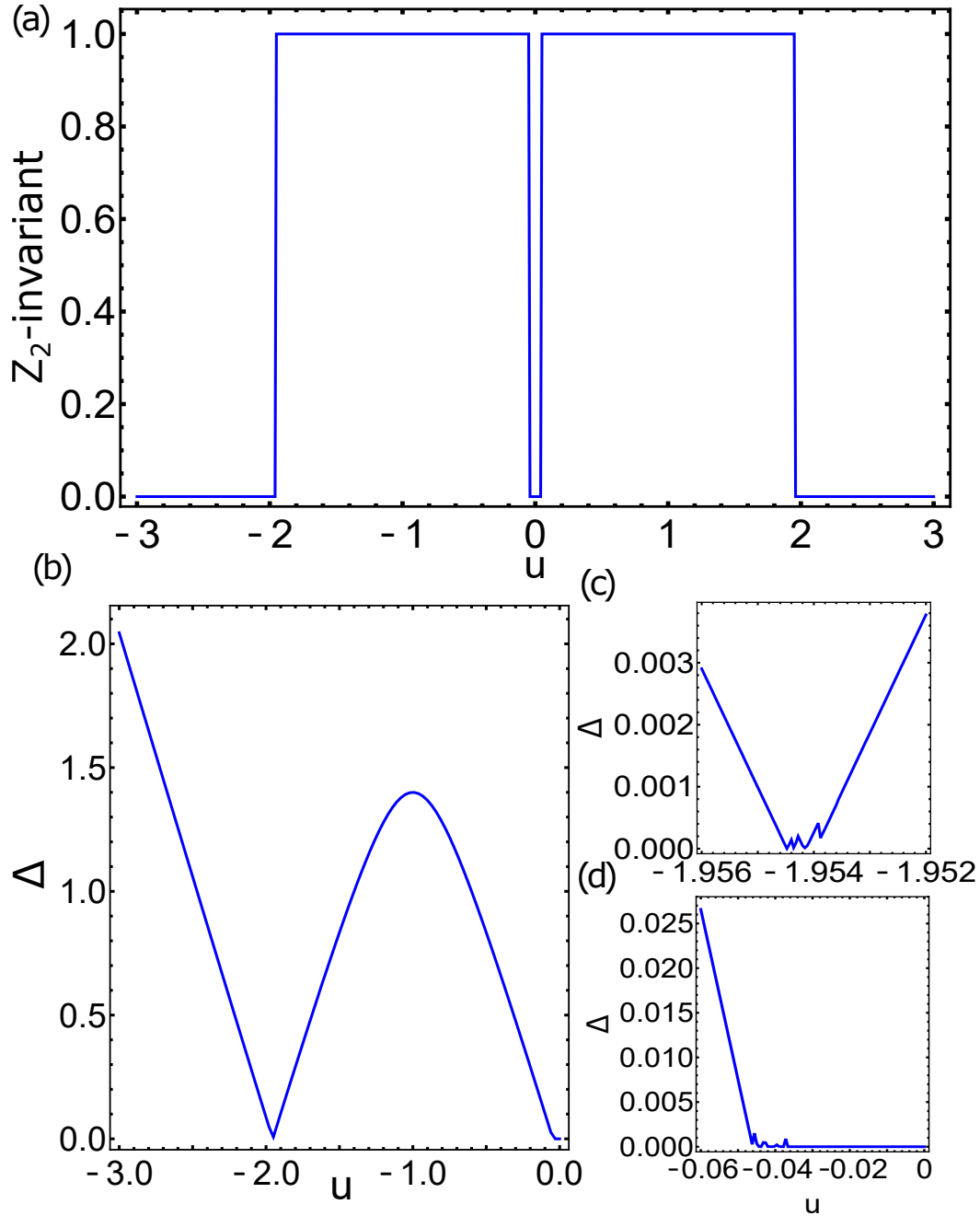
FIGURE 1.4: Topological phase diagram of BHZ Hamiltonian (1.20) with $\Delta = 0.3\sigma_y$. (a) Topological invariant $\mathbb{Z}_2$ as functions of mass term u. (b) Energy gap of the two-dimensional bulk system as functions of mass term u. (c)-(d) Energy gap around the transition points.
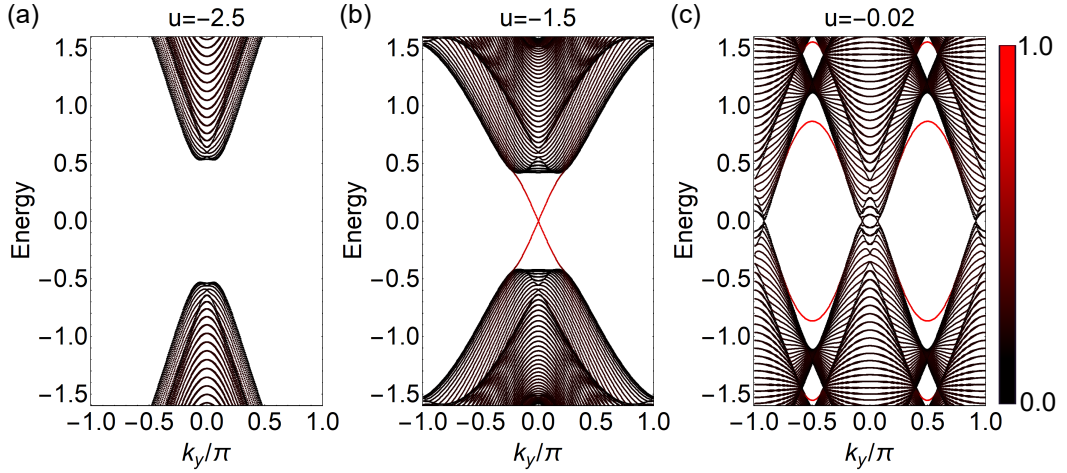
FIGURE 1.5: Dispersion relation of 1D BHZ Hamiltonian for system of width $N = 40$ unit cells at three different phases. Black/Red color indicates the projection of the eigenstates onto the first unit cells located on both of side the system. (a) Trivial insulator with $u = -2.5$. (b) Non-trivial phase with $u = -1.5$ (d) Gapless phase with $u = -0.02$.

symmetric around $k = 0$ due to TRS and because one edge can host both left and right moving edge states. Therefore, the number of nontopological edge states on one edge is always a multiple of 4. Under an adiabatic deformations, these states can be coupled so that they form an anti-crossing and appear (disappear) from that energy level, similarly as in Fig. 1.2 (c). By contrast, this cannot happen at $k = 0, \pi$ since it will violate the Kramers' Theorem which states that at that momenta the states have to be doubly degenerate, similarly as in Fig. 1.2 (d). So the parity of Kramers pairs:

$$d = \frac{N_+(E) + N_-(E)}{2} \text{mod } 2,$$ (1.28)

where $N_{-/+}(E)$ are number of left/right moving edge states on one edge, are a $\mathbb{Z}_2$ invariant because it can only take two values $0(1)$.

1.3 Kitaev model

We start by introducing the Majorana operators from the fermion creation and annihilation operators $\{c, c^\dagger\} = 1$ and their action on states as follow :

$$c^\dagger|0\rangle = |1\rangle, \ c|1\rangle = |0\rangle, \ c^\dagger|1\rangle = c|0\rangle = 0$$ (1.29)

This is Dirac's fermions: a particle is associated with an anti-particle (such as electrons and positrons). However, there is a distinct class of fermions called Majorana fermions: a particle that is its own anti-particle,

$$\gamma^\dagger = \gamma$$ (1.30)
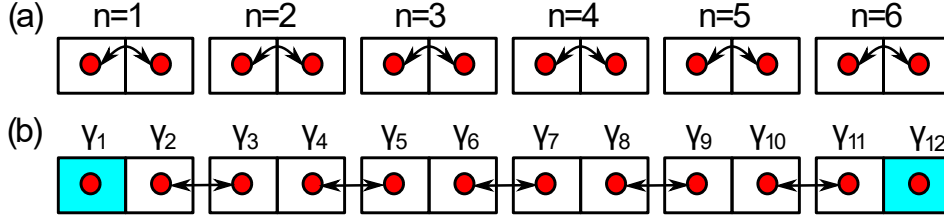
FIGURE 1.6: Schematic view of the system illustrates the two simple cases: (a) $\Delta = t = 0, \mu \neq 0$ and (b) $\Delta = t \neq 0, \mu = 0$. The black arrow indicates the paring order of Majorana states.

Even though the concept was first proposed by Ettore Majorana in the context of particle physics, it has not been discovered as elementary particle in nature to this day, but there are some candidates such as neutrinos. This section focuses on an alternative possibility of its appearance as a quasiparticle in a condensed matter system. Interestingly, one could obtain it by a simple transformation from one basis to the other:

$$c = \frac{1}{2}\left(\gamma_1 - i\gamma_2\right), \;\; c^\dagger = \frac{1}{2}\left(\gamma_1 + i\gamma_2\right) \tag{1.31}$$

$$\gamma_1 = c + c^\dagger, \;\; \gamma_2 = i\left(c - c^\dagger\right). \tag{1.32}$$

So γ_1, γ_2 satisfy the condition Eq.(1.30) and anticommute with each other as Dirac fermions.

$$\gamma_1^2 = \gamma_2^2 = 1, \;\; \{\gamma_1, \gamma_2\} = 0 \tag{1.33}$$

Therefore, a pair of Majorana operators can always be used to express any fermion operator in fermionic systems. In the following step, we will isolate a single Majorana mode from its partner utilizing the idea proposed by A. Kitaev [43]. Let's create a chain of fermions as shown in Fig.1.6 (a), where each domino tile n represents a fermion. Next, we write the one-dimensional superconducting Kitaev Hamiltonian:

$$\mathrm{H} = -\mu \sum_n c_n^\dagger c_n - t \sum_n \left(c_{n+1}^\dagger c_n + h.c\right) + \Delta \sum_n \left(c_{n+1} c_n + h.c\right) \tag{1.34}$$

where μ is the onsite energy, the hopping t between different sites and Δ is the superconducting pairing. By substitute the Eq.(1.31) we arrived:

$$\begin{aligned} \mathrm{H} = &-\mu \sum_n \left(\frac{1}{2} - i\gamma_{2n-1}\gamma_{2n}\right) + \frac{i}{2}\left(t + \Delta\right) \sum_n \gamma_{2n+1}\gamma_{2n} \\ &+ \frac{i}{2}\left(t - \Delta\right) \sum_n \gamma_{2n+2}\gamma_{2n-1} \end{aligned} \tag{1.35}$$

There are two limit cases: the first is $\Delta = t = 0, \mu \neq 0$ Eq. 1.35 reduces to $\mathrm{H}_1 = (i/2)\,\mu \sum_{n=1} \gamma_{2n+1}\gamma_{2n}$ which we pair up the Majoranas from same sites as the situation shown in Fig. 1.6(a) and $\Delta = t \neq 0, \mu = 0$ which help us to obtain unpaired

Majoranas at the end of the chain when the Majoranas are connected from different sites, because the Hamiltonian then becomes $H_2 = it \sum_{n=1} \gamma_{2n+1}^\dagger \gamma_{2n}$ as shown in Fig. 1.6(b). For convenience, the aforementioned superconducting Hamiltonian should be expressed using the Bogoliubov-de Gennes formalism.

$$H = \frac{1}{2} \Psi^\dagger H_{BdG} \Psi, \ \ \Psi = \begin{pmatrix} c_1 \\ \vdots \\ c_N \\ c_1^\dagger \\ \vdots \\ c_N^\dagger \end{pmatrix} \tag{1.36}$$

$$H_{BdG} = -\sum_n \mu \tau_z |n\rangle\langle n| - \sum_n [(t\tau_z + i\Delta \tau_y) |n\rangle\langle n+1| + h.c] \tag{1.37}$$

with $|n\rangle$ a column basis vector $(0,\dots,1,0,\dots)^\intercal$ corresponding to the n-th site of the chain, and $\tau_i, i = x, y, z$ are Pauli matrices acting on the electron and hole states $\tau_i = \sigma_i \otimes \mathbb{1}_N$. It has particle-hole symmetry $\mathcal{P} = \tau_x \mathcal{K}$, $\mathcal{P} H_{BdG} \mathcal{P}^{-1} = -H_{BdG}$. We then can write the BdG Hamiltonian in momentum space:

$$H(k) = \langle k | H_{BdG} | k \rangle = -(2t \cos k - \mu) \tau_z + 2\Delta \sin k \tau_y \tag{1.38}$$

with Bloch eigenstate:

$$|k\rangle = \frac{1}{\sqrt{N}} \sum_n e^{-ikn} |n\rangle. \tag{1.39}$$

The topological invariant of a Bogoliubov-de Gennes Hamiltonian is characterized by the sign of the Pfaffian. This Pfaffian may change sign only when an eigenvalue of $H(k)$ passes through zero. For every eigenvalue $E(k)$ we have another one at $-E(-k)$ because of particle-hole symmetry. So, if $E(k)$ switches sign, then its partner does as well. Furthermore, the spectrum has to be periodic in the Brillouin zone, which means that gap closings at finite momentum always come in pairs so it cannot change the Pfaffian. There are only two exception points which are the TRI: $\tilde{k} = (0, \pi)$, $\tau_x H^*(\tilde{k}) \tau_x = -H(\tilde{k})$, in which every eigenvalue are mapped onto themselves by particle-hole symmetry. To compute the topological invariant the Hamiltonian needs to be transformed into an antisymmetric form:

$$\tilde{H}(0) = \begin{pmatrix} 1 & 1 \\ i & -i \end{pmatrix} \begin{pmatrix} -2t-\mu & 0 \\ 0 & 2t+\mu \end{pmatrix} \begin{pmatrix} 1 & -i \\ 1 & i \end{pmatrix} = -i \begin{pmatrix} 0 & -2t-\mu \\ 2t+\mu & 0 \end{pmatrix} \tag{1.40}$$

$$\tilde{H}(\pi) = \begin{pmatrix} 1 & 1 \\ i & -i \end{pmatrix} \begin{pmatrix} 2t-\mu & 0 \\ 0 & -2t+\mu \end{pmatrix} \begin{pmatrix} 1 & -i \\ 1 & i \end{pmatrix} = -i \begin{pmatrix} 0 & 2t-\mu \\ -2t+\mu & 0 \end{pmatrix}. \tag{1.41}$$

The bulk topological invariant $\mathcal{Q}$ can be obtained by the following expression:

$$\mathcal{Q} = \text{sign} \left(\text{Pf} \left[i\tilde{H}(0) \right] \text{Pf} \left[i\tilde{H}(\pi) \right] \right). \tag{1.42}$$
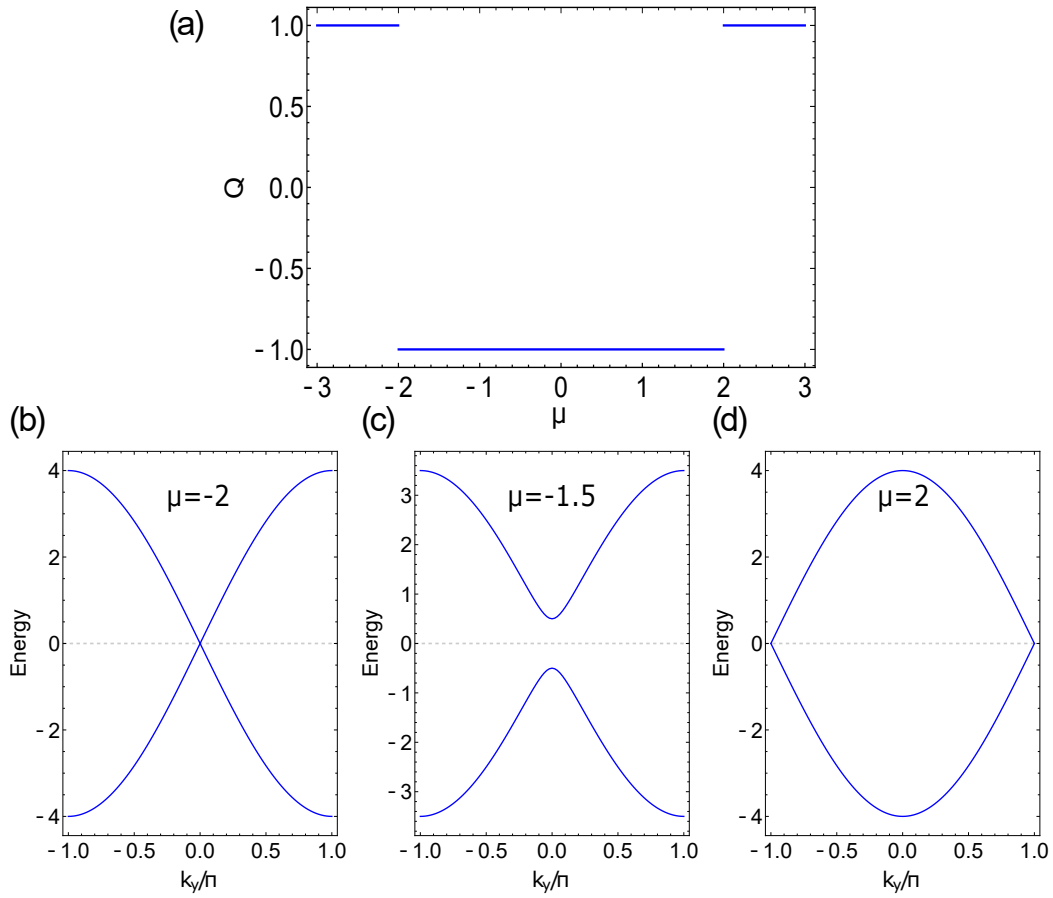
FIGURE 1.7: (a) Topological phase diagram of Kitaev model as a function of onsite potential μ. Band structure of Kitaev Hamiltonian for different chemical potential μ: (b) $\mu = -2.0t$. (c)$\mu = 1.5t$ (d) $\mu = 2.0t$. The gap closing point occurs at TRI points with $|\mu| = 2t$. We set $\Delta = t$ and t as the energy scale
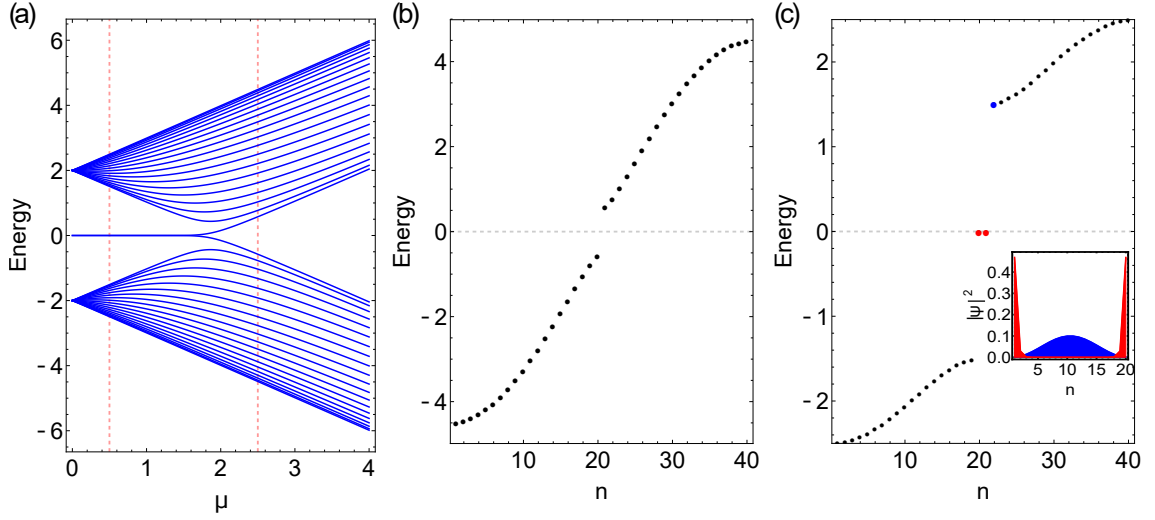
FIGURE 1.8: (a) The spectrum of an open Kitaev chain with $N = 20$ unit cells as a function of μ. The red dashed lines indicates the values of μ used in (b) and (c). (b) Trivial superconductor with $\mu = 2.5$. The system is gapped and there are no end states. (c) The topological regime with $\mu = 0.5$ shows two states at zero energy (red dots) and the blue dot is the first excited states. Inset: Local density of states (LDOS) as a function of position n. We set $t = 1.0$, $\Delta = t$.

For a 2×2 antisymmetric matrix:

$$\text{Pf}\left[i\tilde{\text{H}}\left(0\right) \right] = -2t - \mu \tag{1.43}$$

$$\text{Pf}\left[i\tilde{\text{H}}\left(\pi\right) \right] = 2t - \mu \tag{1.44}$$

As shown in Fig. 1.7 (a) $\mathcal{Q}$ changes sign at $\mu = -2t$ when $\text{Pf}\left[i\tilde{\text{H}}\left(0\right) \right]$ changes sign. This happens at the band crossing at $k = 0$ as shown in Fig. 1.7 (b). Another topological phase transition occurs at $\mu = 2t$ when $\text{Pf}\left[i\tilde{\text{H}}\left(\pi\right) \right]$ changes sign, and the band crossing occurs at $k = \pi$ as shown in Fig. 1.7 (d). The trivial phase characterized by $\mathcal{Q} = 1$ while $\mathcal{Q} = -1$ means that the bulk is in a topological phase. To understand the relationship between the edge Majorana modes and the bulk topological invariant $\mathcal{Q}$, we calculate the spectrum of the open-chain Kitaev Hamiltonian Eq. (1.37) as a function of μ. As shown in Fig. 1.8 (a), two states at zero energy, corresponding to the two unpaired Majorana zero modes, start to split around $\mu = 2t$. Moreover, as shown in Fig. 1.8 (c), these states are localized at the end of the wire. As long as the bulk energy gap is finite, the Majorana modes are protected by PHS which requires the spectrum has to be symmetric around zero energy. In contrast, when $\mu > 2t$ the Majorana modes disappeared as shown in Fig. 1.8 (b).

Chapter 2

Topological crystalline insulators

Until now, our primary focus has been on studying topological phases and phenomena that are protected solely by nonspatial AZ symmetries. In this chapter, we present additional spatial symmetries and discuss how these modifications impact the topological distinctions of gapped phases, resulting in an enrichment of the tenfold classification of topological insulators (TIs) and topological superconductors (TSCs). Imposing additional symmetries can have two potential effects. Specifically, additional spatial symmetries can lead to modifications in the topological classification [32], including weak TIs and TSCs. In such cases, the topological properties rely on the presence of lattice-translation symmetry or point-group symmetries, such as reflection and rotation [91]. Alternatively, these extra symmetries might not change the topological classification but can result in simplified formulations for the topological invariants within the tenfold classification [26, 27, 30]. In the following sections, after providing a brief overview of spatial symmetries, we focus on the classification of TCIs and TCSs in the presence of reflection symmetry. We then delve into the study of the SnTe topological crystalline insulator. For ease of understanding, the notation used in this chapter will follow the conventions from [16].

2.1 Classification of topological crystalline insulators and superconductors

Spatial symmetries of a lattice are described by space groups. Operations in space groups consist of lattice translations and point-group operations that leave at least one point in space unchanged (for example reflection, inversion and rotations). Consider a space-group operation G that maps the mth site in the unit cell at $\mathbf{r}$ to the $m'th$ site in the unit cell at $u_G\mathbf{r} + \mathbf{R}_m$ in a d-dimensional system, where u_G is an orthogonal $d \times d$ matrix and $\mathbf{R}_m$ is a lattice vector. Then fermion annihilation operators in real space $\hat{\psi}_a(\mathbf{r})$ are transformed correspondingly by a unitary operator $\hat{\mathcal{G}}$ acting on the electron field operator as

$$\hat{\mathcal{G}} \cdot \hat{\psi}_a(\mathbf{r}) \cdot \hat{\mathcal{G}}^{-1} = \sum_b \mathrm{U}_G^{ab} \hat{\psi}_a(u_G\mathbf{r} + \mathbf{R}_b) \tag{2.1}$$

where indices a and b label the sites within a unit cell as well as internal degrees of freedom, such as spin, and U_G is a unitary matrix. In general, we can always use momentum-space Bloch functions as the basis functions in generating irreducible representations of a space group. In momentum space, the fermion annihilation operators transform as

$$\hat{\mathcal{G}} \cdot \hat{\psi}_a(\mathbf{k}) \cdot \hat{\mathcal{G}}^{-1} = \sum_b U_G^{ab} e^{-i u_G \mathbf{k} \cdot \mathbf{R}_a} \hat{\psi}_b(u_G \mathbf{k}) \tag{2.2}$$

Hamiltonian has crystalline symmetry if $\hat{\mathcal{G}}\hat{\mathcal{H}}\hat{\mathcal{G}}^{-1} = \hat{\mathcal{H}}$ or the Bloch-BdG form:

$$U_G(\mathbf{k}) H(u_G^{-1}\mathbf{k}) U_G^\dagger(\mathbf{k}) = H(\mathbf{k}) \tag{2.3}$$

Crystalline symmetries are either symmorphic or nonsymmorphic space-group symmetries. A space group is called symmorphic if, in addition to lattice translations, all generating symmetry operations leave one common point fixed, $\mathbf{k}_0$ [21]. We then have $[H(\mathbf{k}_0), U_G(\mathbf{k}_0)] = 0$ which leads to the possibility to define topological invariants at $(\mathbf{k}_0)$ in the eigenbasis of $U_G(\mathbf{k}_0)$. In this chapter, we mainly focus on such symmorphic symmetry, which is reflection symmetry. Consider a the Bloch Hamiltonian that is invariant under reflection in the n_1 direction,

$$R_1^{-1} H(-k_1, \tilde{\mathbf{k}}) R_1 = H(k_1, \tilde{\mathbf{k}}) \tag{2.4}$$

where $\tilde{\mathbf{k}} = (k_2, \ldots, k_d)$. Because R_1[1] is unitary, thus, on the corresponding reflection plane, the hyperplanes that are symmetric under reflection in the BZ, $k_1 = 0$, ones can always choose:

$$R_1^\dagger = R_1, \ R_1{}^2 = \mathbb{1}, \tag{2.5}$$

so that the eigenvalues of R_1 are either -1 or $+1$. Finally, the classification of topological insulators and superconductors in the presence of reflection symmetry is defined by the relations between R_1 and the AZ symmetry operators ($\mathcal{T}$, $\mathcal{P}$ and $\mathcal{S}$)

$$R_1\mathcal{T} = \theta_\mathcal{T}\mathcal{T}R_1, \ R_1\mathcal{P} = \theta_\mathcal{P}\mathcal{P}R_1, \ R_1\mathcal{S} = \theta_\mathcal{S}\mathcal{S}R_1 \tag{2.6}$$

with $\theta_{\mathcal{T},\mathcal{P},\mathcal{S}} = \pm 1$. For the nonchiral symmetry classes AI, AII, AIII, C, and D, these values are labeled by $R_{\theta_\mathcal{T}}, R_{\theta_\mathcal{P}}, R_{\theta_\mathcal{S}}$, and $R_{\theta_{\mathcal{T}\mathcal{P}}}$ for chiral symmetry classes BDI, CI, CII, and DIII in table 1.1. As a result, we obtain 27 different symmetry classes in the presence of AZ and reflection symmetries. More details can be found in table VIII in the review paper [16] which summarizes as follow:

- $\mathbb{Z}$ and $\mathbb{Z}_2$ invariants: In cases where symmetry classes with minimum one AZ symmetry that anticommutes with the reflection operator, R, the topological

---
[1]R_1 can depend only on k_1

invariants ($\mathbb{Z}$ or $\mathbb{Z}_2$) of the original tenfold classification continue to maintain in certain cases, even when reflection is present. These invariants protect gapless boundary modes, regardless of the orientation of the boundary.

- $M\mathbb{Z}$ and $M\mathbb{Z}_2$ invariants: On the hyperplanes in the BZ that are symmetric under reflection, The mirror Chern numbers $M\mathbb{Z}_2$, the mirror winding numbers $M\mathbb{Z}$, and the mirror invariants $\mathbb{Z}_2$ are computed. A nontrivial value of these mirror indices signifies the presence of protected boundary modes at reflection symmetric surfaces. Conversely, surfaces that break reflection symmetry are generally characterized by a gap.

- $\mathcal{T}\mathbb{Z}_2$ invariant: In categories where the operator R anticommutes with both $\mathcal{T}$ and $\mathcal{P}$ operators, the second-order $\mathbb{Z}_2$ invariants are well defined only with the existence of translation symmetry. That is, protected TCIs and TCSs can exist if reflection, translation, and AZ antiunitary symmetries are all present.

- $M\mathbb{Z}\oplus\mathbb{Z}$ and $M\mathbb{Z}_2\oplus\mathbb{Z}_2$ invariants: When reflection-symmetric TIs (TCSs) with chiral symmetry are characterized both by a $\mathbb{Z}$ ($\mathbb{Z}_2$) invariant and independently by a mirror index $M\mathbb{Z}$ ($M\mathbb{Z}_2$). At boundaries that are perpendicular to the mirror plane, the number of protected gapless states is corresponding to the maximum values of $|n_{\mathbb{Z}}|$ and $|n_{M\mathbb{Z}}|$ [17].

In contrast to our previous chapter, where we examined gapless topological surface states that exist at any boundary of TCIs and TSCs protected by nonspatial AZ symmetries, TCIs and TCSs only display these gapless modes on surfaces that remain unchanged by the crystal symmetries. The lack of gapless modes on boundaries that violate spatial symmetries does not imply a trivial bulk topology and thus cannot be relied upon to deduce the topology of TCIs and TCSs. In the upcoming section, we will illustrate this concept using SnTe as a case study for topological crystalline insulators.

2.2   SnTe materials

SnTe materials have been experimentally identified as TCIs protected by reflection symmetry [38, 88]. Our starting is the p-orbital tight-binding Hamiltonian:

$$
\begin{aligned}
H(\mathbf{k}) \;=\;& m\mathbb{1}_2\otimes\mathbb{1}_3\otimes\Sigma + t_{12}\sum_{\alpha=x,y,z}\mathbb{1}_2\otimes(\mathbb{1}_3 - L_\alpha^2)\otimes h_\alpha(k_\alpha) \\
&+ t_{11}\sum_{\alpha\neq\beta}\mathbb{1}_2\otimes\left[\mathbb{1}_3 - \frac{1}{2}\left(L_\alpha + \epsilon_{\alpha\beta}L_\beta\right)^2\right]\otimes h_{\alpha,\beta}(k_\alpha,k_\beta)\Sigma \\
&+ \sum_{\alpha=x,y,z}\lambda_\alpha\,\sigma_\alpha\otimes L_\alpha\otimes\mathbb{1}_8,
\end{aligned}
\tag{2.7}
$$

which has been used for describing the bulk topological crystalline insulator phase in the SnTe materials [38] and various topological phases in lower dimensional systems [11, 83]. Here we have chosen a cubic unit cell containing eight lattice sites Fig. (2.1), Σ is a diagonal 8×8 matrix with entries $\Sigma_{i,i} = \mp 1$ at the two sublattices (Sn and Te atoms), $\varepsilon_{\alpha\beta}$ is Levi-Civita symbol, $L_\alpha = -i\varepsilon_{\alpha\beta\gamma}$ are the 3×3 angular momentum $L = 1$ matrices, σ_α are Pauli matrices, and $h_\alpha(k_\alpha)$ and $h_{\alpha,\beta}(k_\alpha, k_\beta)$ are 8×8 matrices describing hopping between the nearest-neighbors and next-nearest-neighbor sites, respectively . For more details, please refer to the Appendix A where we have included our paper in Chapter. 5. Here, we use $m = 1.65$ eV, $t_{12} = 0.9$ eV and $\lambda_\alpha \equiv \lambda = 0.3$ eV.

In the context of topological crystalline materials, a common method to differentiate between topologically trivial and nontrivial phases is by examining the midgap states present in the entanglement spectrum or entanglement Hamiltonian. These states serve as a reliable indicator. The distinguishing feature of these materials lies in their non-zero mirror Chern numbers, which result in the presence of four surface Dirac cones. These cones are protected by the reflection symmetry, providing further evidence of the material's topological nature. We note that the Hamiltonian exhibits the mirror and time-reversal symmetries. The diagonal mirror symmetries M_{xy} (M_{yx}) with respect to the $\hat{x} + \hat{y}$ ($\hat{x} - \hat{y}$) planes are the following:

$$M_{xy} = \frac{\sigma_x - \sigma_y}{\sqrt{2}} \otimes \left((L_x - L_y)^2 - \mathbb{1}_3\right) \otimes P_{xy} \tag{2.8}$$

$$M_{yx} = \frac{\sigma_x + \sigma_y}{\sqrt{2}} \otimes \left((L_x + L_y)^2 - \mathbb{1}_3\right) \otimes P_{yx} \tag{2.9}$$

where

$$P_{xy} = \begin{pmatrix} 1 & 0 & 0 & 0 & 0 & 0 & 0 & 0 \\ 0 & 1 & 0 & 0 & 0 & 0 & 0 & 0 \\ 0 & 0 & 0 & 1 & 0 & 0 & 0 & 0 \\ 0 & 0 & 1 & 0 & 0 & 0 & 0 & 0 \\ 0 & 0 & 0 & 0 & 0 & 1 & 0 & 0 \\ 0 & 0 & 0 & 0 & 1 & 0 & 0 & 0 \\ 0 & 0 & 0 & 0 & 0 & 0 & 1 & 0 \\ 0 & 0 & 0 & 0 & 0 & 0 & 0 & 1 \end{pmatrix} \tag{2.10}$$

$$P_{yx} = \begin{pmatrix} 0 & 1 & 0 & 0 & 0 & 0 & 0 & 0 \\ 1 & 0 & 0 & 0 & 0 & 0 & 0 & 0 \\ 0 & 0 & 1 & 0 & 0 & 0 & 0 & 0 \\ 0 & 0 & 0 & 1 & 0 & 0 & 0 & 0 \\ 0 & 0 & 0 & 0 & 1 & 0 & 0 & 0 \\ 0 & 0 & 0 & 0 & 0 & 1 & 0 & 0 \\ 0 & 0 & 0 & 0 & 0 & 0 & 0 & 1 \\ 0 & 0 & 0 & 0 & 0 & 0 & 1 & 0 \end{pmatrix} \tag{2.11}$$

They are Kronecker products of three parts corresponding to the spin, the orbital and the atomic degrees of freedom, respectively. P_{xy}/P_{yx} is the matrix that exchanges the atomic positions with respect to the mirror plane and the time-reversal
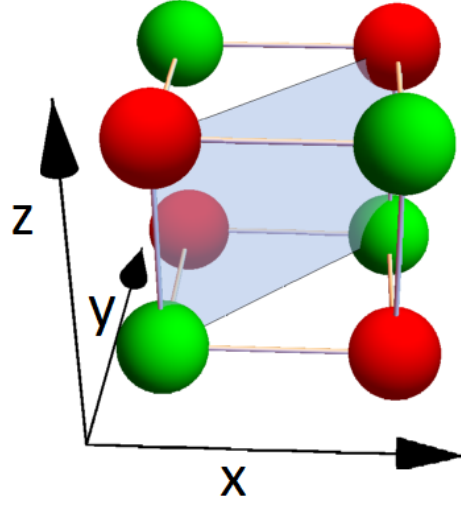
FIGURE 2.1: Schematic view of the unit cell. The two sublattices, corresponding to Sn (red) and Te (green) atoms, have opposite on-site energies. The shaded plane is the M_{xy} mirror plane.

operator is $\mathcal{T} = T\mathcal{K}$, $T = \sigma_y \otimes \mathbb{1}_3 \otimes \mathbb{1}_8$. These operators satisfy the following relations:

$$
\begin{aligned}
TH(\mathbf{k})T^\dagger &= H(-\mathbf{k})^\intercal \\
M_{xy}H(k_x, k_y, k_z)M_{xy}^\dagger &= H(k_y, k_x, k_z) \\
M_{yx}H(k_x, k_y, k_z)M_{yx}^\dagger &= H(-k_y, -k_x, k_z),
\end{aligned}
\tag{2.12}
$$

and the mirror operator anticommutes with the time-reversal operator. In the eigenbasis of these mirror operators, T takes block off-diagonal form while Hamiltonian has a block-diagonal form since it commutes with the mirror operators. Therefore, the sum of the mirror chern numbers (MCN) vanishes on the high symmetry planes, so that each block has an opposite MCN. The block-diagonal H':

$$
H' = \beta_M^{-1} H \beta_M,
\tag{2.13}
$$

with $\beta_M = \{|\alpha_j\rangle\}_{j=1\ldots d}$ are eigenbasis of $M_{xy}(M_{yx})$. The integral of the Berry curvature over the Brillouin zone summed over all occupied bands gives an integer called the Chern number

$$
C = \sum_{n \leqslant n_F} C^{(n)},
\tag{2.14}
$$

with $C^{(n)}$ is given in the previous Chapter, Eq. (1.16). Nonetheless, the expression (2.14) is impractical for numerical computation due to its reliance on a continuous gauge of vectors $|n, \mathbf{k}\rangle$, which can only be determined numerically for large matrices. This challenge can be overcome through special gauge-invariant approaches for Berry curvature [20]. However, these methods yield Berry curvature on a band-by-band basis and become singular when encountering band crossings. In scenarios where the curvatures of individual bands are unnecessary, as is the case here, the most
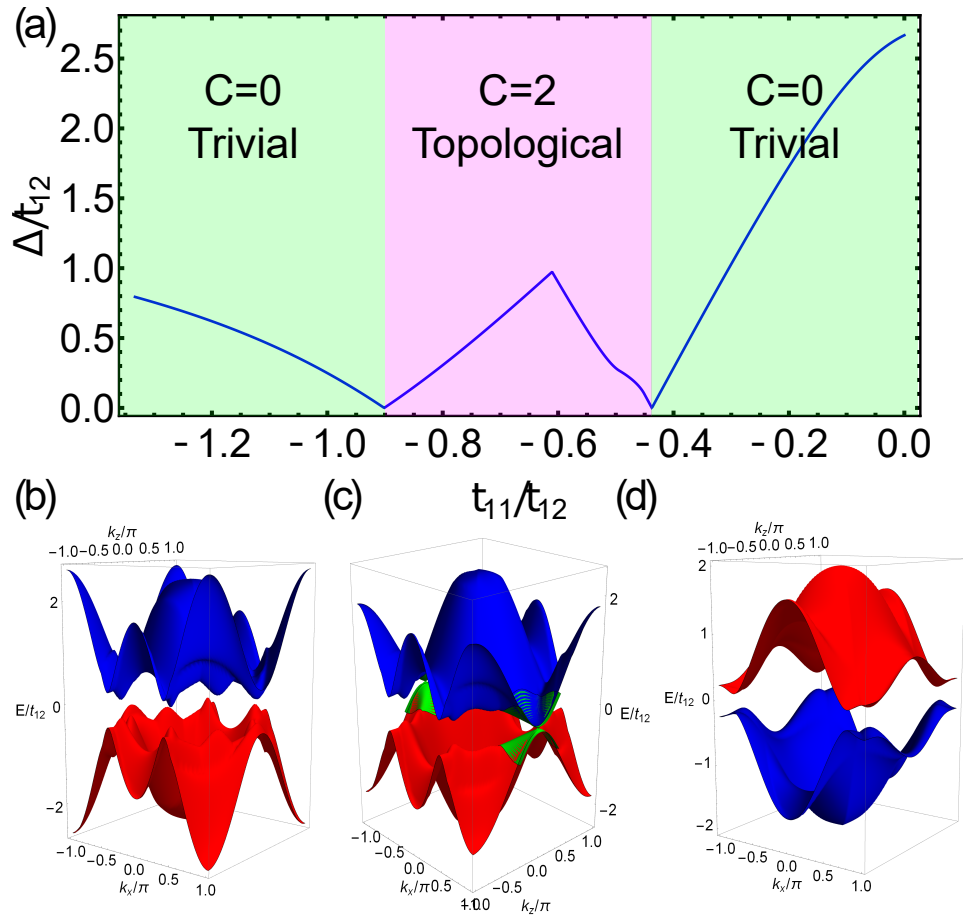
FIGURE 2.2: (a) Band gap (blue line) of the first diagonal-block of the three dimensions Hamiltonian (2.7) in the eigenbasis of M_{xy} as a function of the next-nearest-neighbor hopping t_{11}. Notice that on this mirror plane $(k_x, k_y, k_z) \rightarrow (k_x, k_x, k_z)$. (b)-(d) Bulk spectra for different values of $t_{11} = -1.1t_{12}$, $-0.9t_{12}$ and $-0.5t_{12}$ on the mirror plane. The green region in (c) highlight where the gap closing happens

pragmatic approach is to represent the Chern number as so-called Kubo formula that describes Hall conductivity in the quantum Hall systems [60]:

$$C = \frac{1}{\pi} \int_0^{2\pi} \int_0^{2\pi} \sum_{\substack{n \leqslant n_F \\ n' > n_F}} \mathbf{Im} \left[\frac{\langle n | \partial_{k_x} H' | n' \rangle \langle n' | \partial_{k_z} H' | n \rangle}{(\epsilon_n - \epsilon_{n'})^2} \right] dk_x dk_z, \qquad (2.15)$$

where $|n\rangle$ and ϵ_n are the eigenstates and the eigenvalues of the Hamiltonian in the projected subspace, H', and n_F is the half-filling. In the sum n runs over the occupied bands and n' over unoccupied ones. In our case, we do not insert the full Hamiltonian into the Kubo formula because it would give zero Chern number due to TRS. Instead we insert one of the diagonal blocks of H in the eigenbasis of the mirror operator M_{xy} (M_{yx}). It is worth noting that integral in Eq. (2.15) is calculated over the mirror plane, $k_x = k_y$. In Fig. 2.2, we plot the bulk gap on the corresponding mirror plane as function of the next-nearest-neighbor hopping t_{11}. When the MCN is equal to 0 we have a trivial insulator, while it is equal to 2 in the case of a TCI.

On the other hand, the bulk-boundary correspondence exists for surfaces that are parallel to the M_{xy} (M_{yx}) plane because it preserves these symmetries. Thus, we open the Hamiltonian respect to n_z-direction to show the surface Dirac cones. In Fig. 2.3, we show that the surface Dirac cones are correctly present in the low energy spectrum of a system with $L = 500$ layers stacked in the n_z-direction, with two cones appearing on each mirror M_{xy} (M_{yx}) eigenbasis.
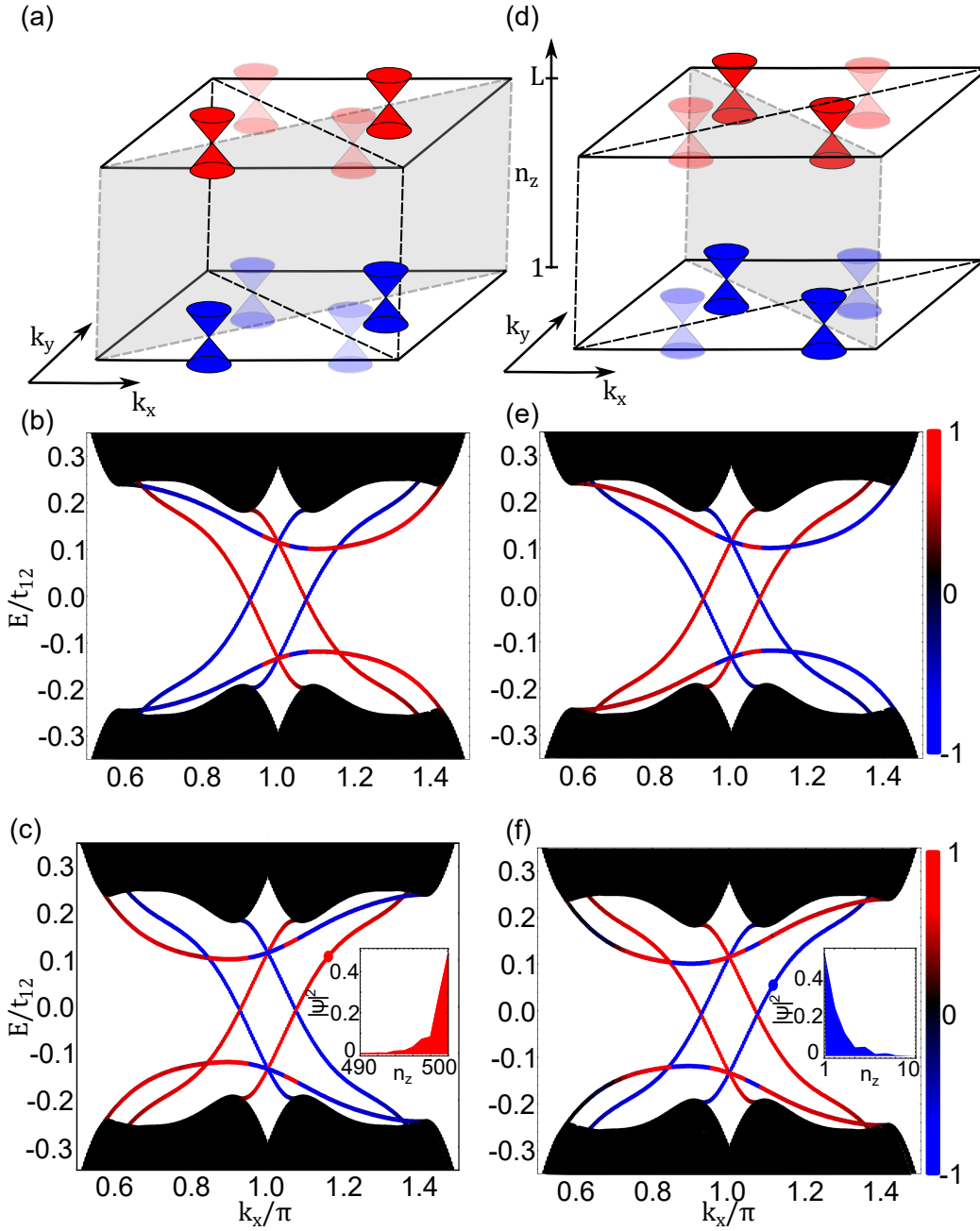
FIGURE 2.3: (a) and (d) Schematic views of the SnTe multilayers stacked in the (001) direction with with $L = 500$ layers. The shaded planes are M_{xy} and M_{yx} plane, respectively. (b)-(c) Dispersion relations of the first and second diagonal-block in M_{xy} eigenbasis. (e)-(f) Dispersion relations of the first and second diagonal-block in M_{yx} eigenbasis. Here, we set the next nearest hoping $t_{11} = -0.65t_{12}$. Blue/Red color indicate the projection of the eigenstates onto the first/last unit cells located at the lower (blue) and upper (red) surface of the system. Inset: Local density of states (LDOS) as a function of position n_z for the states shown with red and blue dots in (c) and (d).

Chapter 3

Gapless topological phases

In Chapter 1, while studying the BHZ model with anti-symmetric coupling between two layers, we encountered a gapless phase region while calculating the topological phase diagram. The primary objective of this chapter is to further explore the nature of this gapless topological phase and establish a foundation before proceeding to Chapter 5, where we will present our research results featuring the Weyl semimetal phase.

3.1 Classification of gapless topological phases

Fermi surfaces, Fermi points, and nodal lines are directly derived from the Pauli exclusion principle, which states that each quantum state can only accommodate one electron. In other words, they represent the points in momentum space where the energy dispersion $\epsilon(k)$ is equal to zero. These objects are collectively known as Fermi surfaces (FSs) for simplicity. If there is a FS present at any energy then the bulk system is considered gapless. FSs can be topologically stable, meaning that they cannot be fully closed by local perturbations in momentum space. This chapter provides a review of the topological classification of stable FSs in gapless semimetals, as discussed in recent papers [58, 99]. It is important to note that, in lattice systems, the concept of stability only applies to a "single" FS, which is isolated from other FSs in the Brillouin zone (BZ). Therefore, we focus on FSs that are located within a specific region of the BZ, rather than considering all FSs in the entire BZ. This is because in lattice systems, it is possible to close FSs in pairs by introducing perturbations that connect different FSs. Additionally, FSs with nontrivial topological charges in any lattice system are always accompanied by partners with opposite topological charges. As a result, the sum of the topological charges of all FSs in full BZ is zero. Consequently, the topological invariants for FSs are defined in terms of integrals along specific submanifolds of the BZ, rather than integrals over the entire BZ as in the case of TIs and TSCs discussed in previous Chapters.

In these gapless systems, the bulk-edge correspondence can be interpreted by considering the wave vector parallel to the system boundary, labeled as $\mathbf{k}_{||}$, as a parameter then establish the bulk-edge correspondence to the remaining lower-dimensional Hamiltonian. Whenever the line or plane corresponding to a constant $\mathbf{k}_{||}$ crosses a FS point (nodal, Dirac or Weyl points), the topological invariants of
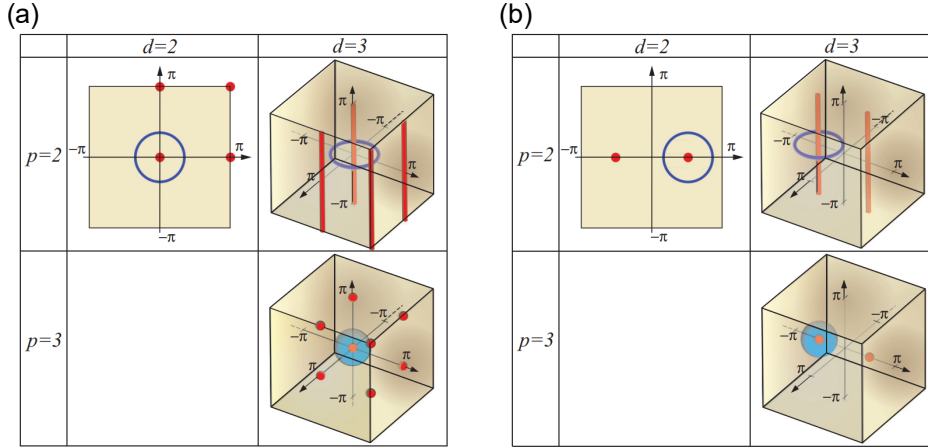
FIGURE 3.1: The way we classify "isolated" stable Fermi surfaces depends on how they change under global antiunitary symmetries. (a) Each Fermi surface (red point/line) remains unchanged under global nonspatial AZ symmetries. Blue circles/spheres represents the contour in which the topological invariants are defined. (b) Different Fermi surfaces are connected to each other in pairs through global symmetries. Adapted from [15].

the Hamiltonian $H(\mathbf{k}_{||})$ changes according to such as the winding of the Dirac point or chiralities of Weyl nodes. This means that zero energy edge states can emerge for specific momentum values that are parallel to the boundary.

The topological gapless system are classified by both the symmetry class of their Hamiltonians and the codimension p of the FS. In the scope of this chapter, we only focus on stable FSs protected by nonspatial AZ symmetries. Gapless phases, which are protected by spatial symmetries, will be briefly reviewed in the next chapter. The codimension is defined as:

$$p = d - d_{FS}, \tag{3.1}$$

in which d and d_{FS} are the dimension of the BZ and the "minimal" dimension of the FS, respectively. Here we define here d_{FS} as the smallest possible dimension of the band crossing when the Fermi energy is varied because the dimension of the FS can be different corresponding to different Fermi energies. For example, in Weyl semimetals, the Fermi surface is either zero dimensional (at the Weyl node) or two dimensional (when the Fermi energy is far away from the band crossing) so $d_{FS} = 0$. Notice that p cannot larger than d since d_{FS} is always positive. Furthermore, in another analysis of the topology of the system, it is crucial to distinguish whether the Fermi surfaces (FSs) remain unchanged by the non-spatial antiunitary AZ symmetries [58]. In Fig. 3.1, two different scenarios need examination:

   (i) Each individual FS is invariant under antiunitary AZ symmetries, denoted as FS1 [84, 99, 100].

   (ii) Different FSs are pairwise related to each other through AZ symmetries, referred to as FS2 [15, 58].

In the following section, we explore two cases in which we explore Fermi surfaces at or off high-symmetry points to gain a deeper understanding of the system.

3.2 Two dimensional nodal superconductor and Weyl semimetals

In this section, we illustrate two examples of gapless topological states. First, we present the tight-binding 2D Hamiltonian of the square lattice [15]:

$$H(\mathbf{k}) = \sigma_x \sin k_x + \sigma_y \sin k_y, \tag{3.2}$$

which describes a nodal superconductor with point nodes. The system preserves the time-reversal symmetry (TRS) $\mathcal{T} = \sigma_y \mathcal{K}, \mathcal{T}^2 = -1$, and particle-hole symmetry (PHS) $\mathcal{P} = \sigma_x \mathcal{K}, \mathcal{P}^2 = 1$, which, according to Table 1.1, belongs to the DIII class. At four time-reversal-invariant (TRI) momenta: $\tilde{\mathbf{k}} = (0,0), (0,\pi), (\pi,0), (\pi,\pi)$, the bulk spectrum exhibits four point nodes, as shown in Fig. 3.2(a). Fermi surfaces located at high-symmetry points in the Brillouin zone can be protected by invariants of $\mathbb{Z}$ or $\mathbb{Z}_2$ type [58, 99, 100]. In this case, these points are characterized by a winding number. In this case, Hamiltonian (3.2) preserve chiral symmetry $\mathcal{S} \sim \mathcal{T}\mathcal{P} \sim \sigma_y\sigma_x$ and can be transformed:

$$H'_{(k_y=0)} = \begin{pmatrix} 0 & \sin k_x - i \sin k_y \\ \sin k_x + i \sin k_y & 0 \end{pmatrix}, \tag{3.3}$$

in the eigenbasis of $\mathcal{S}$. Generalizes to any one dimensional class with $\mathcal{S}$, the winding number can be written as:

$$\nu = \frac{i}{2\pi} \int_C q^* dq, \text{ with } q = \frac{\sin k_x - i \sin k_y}{\sqrt{\sin^2 k_x + \sin^2 k_y}} \tag{3.4}$$

If C is a closed loop around one of the four nodal points ν is quantized to ± 1, and it is zero otherwise. It turns out that around the nodes $\mathbf{k} = (0,0)$ and (π,π) Eq. (3.4) yields 1, and for $\mathbf{k} = (0,\pi)$ and $(\pi,0)$ it gives -1, respectively. The bulk-edge correspondence will be characterized by flat-band edge states protected by TRS and PHS for all surfaces, except the (10) and (01) faces. To demonstrate this, we transform Hamiltonian (3.4) as follows:

$$H(k_x, k_y) \rightarrow H'(k_{||}, k'_y) = H(k_{||} - k'_y, k'_y). \tag{3.5}$$

Then, we quantize k'_y. The open spectrum shows that these edge states connect two nodal points with opposite winding numbers in the boundary Brillouin zone, as displayed in Fig. 3.2(b).

For the case in which FS is off high-symmetry points, we consider a four-band
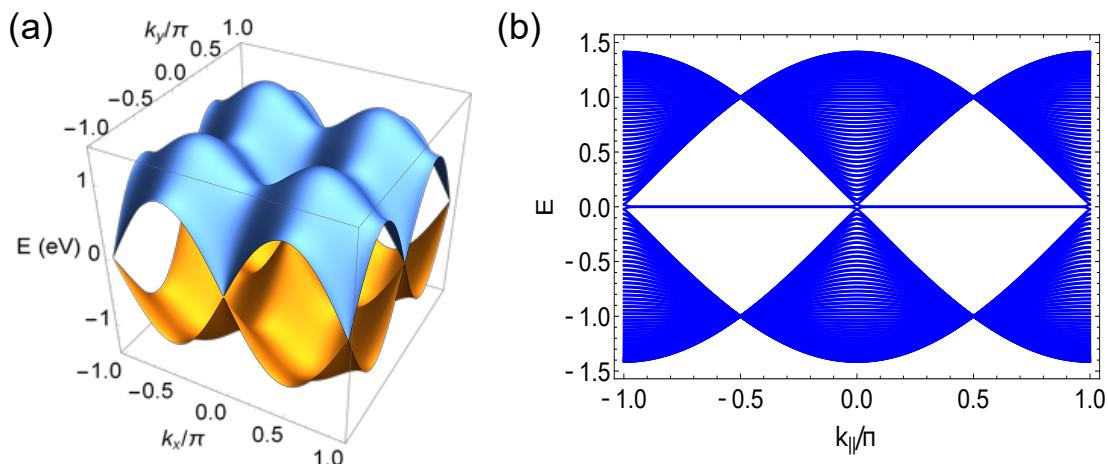
FIGURE 3.2: (a) The bulk spectrum of two dimensional SC exhibits four point nodes at TRI momenta. (b) Band structure of the nodal superconductor (3.2) as a function of edge momentum $k_{||}$. The flat-band edge states with system width $L = 100$ unit cells connect two projected nodal points with opposite winding number.

semimetal Hamiltonian with two Dirac points [14, 16]:

$$H(\mathbf{k}) = \tau_x \theta_x \sin k_x + \tau_x \theta_y \sin k_y + \tau_z \left(\cos k_x + \cos k_y + \cos k_z - m \right) \qquad (3.6)$$

where

$$\theta_{x,y,z} = \mathbb{1}_2 \otimes \sigma_{x,y,z} \qquad (3.7)$$
$$\tau_{x,y,z} = \sigma_{x,y,z} \otimes \mathbb{1}_2 \qquad (3.8)$$

are Pauli matrices acting on spin and orbital spaces, respectively. The model Hamiltonian (3.6) preserves TRS $\mathcal{T} = \theta_y \mathcal{K}, \mathcal{T}^2 = -1$, and inversion symmetry $I = \theta_z$. When one of these symmetries is broken, for example, by adding the Zeeman field $\theta_z \Delta'$ to break TRS, the Dirac cone will separate into two Weyl nodes. Here, we use the same idea to exemplify bulk-boundary correspondence and study the projection of the wave vector parallel to a specific continuous sample boundary, in this case is (100) surface where k_x is quantized. We consider a set of planes $\mathcal{N}_{k_z}$, where each of these planes can be interpreted as a 2D fully gapped Chern insulator with a chiral edge mode. The generic formula which derived from the Berry curvature $\mathcal{F}$ for the Chern number. However, for numerical simplicity, we utilize Eq. (1.18) with:

$$C^{(i)} = \frac{1}{2\pi} \sum_{n,m} \mathrm{F}_{(n,m)}, \qquad (3.9)$$

where $F_{(n,m)}$ is defined in Eq. (1.17). It is important to note that this Hamiltonian involves four bands, requiring us to take the sum of the two occupied bands, $i = 1, 2$. When $m = 2$ and $\Delta' = 0.5$ [1], and the $\mathcal{N}_{k_z}$ planes are positioned within

---

[1] positions of Weyl points depend on these parameters
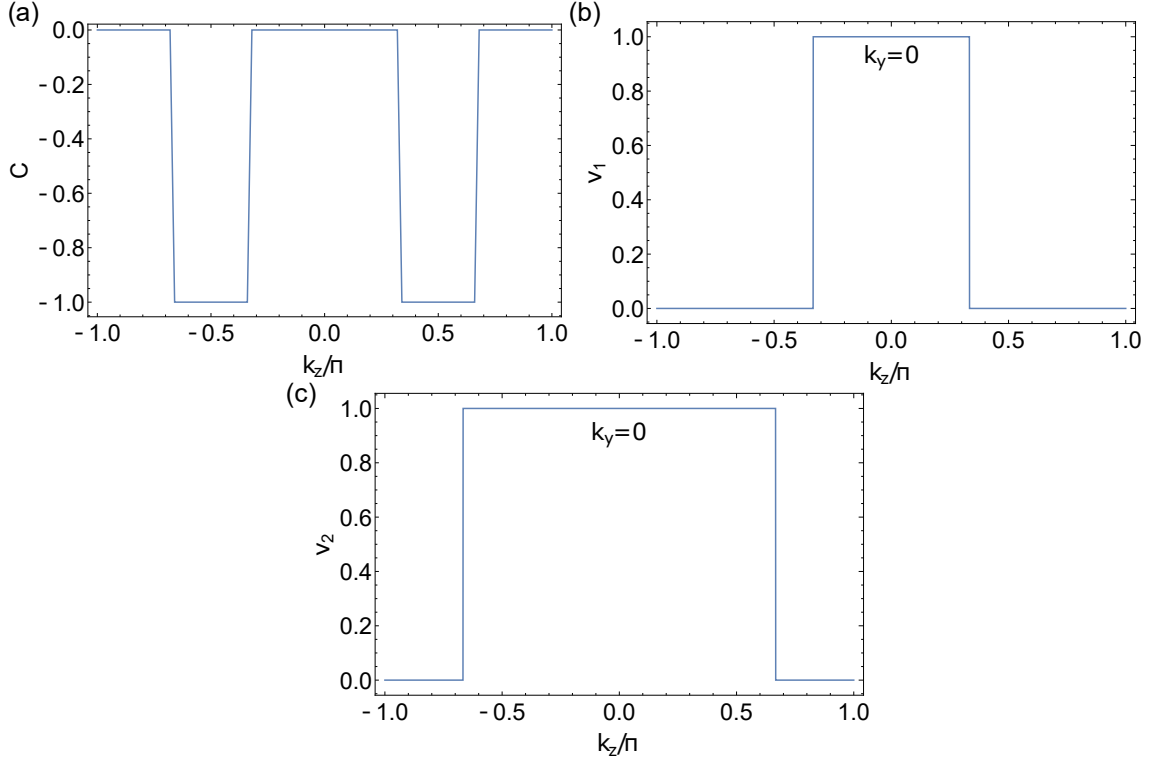
FIGURE 3.3: Topological phase diagrams of Hamiltonian. (3.6) with TRS breaking term $\theta_z \Delta'$ as functions momentum k_z: (a) Chern number C (b) and (c) are winding numbers of two block Hamiltonian in the eigenbasis of $\mathbf{R}$. Here we set $m = 2.0, \Delta' = 0.5$.

$\pi/3 < |k_z| < 2\pi/3$, between two Weyl nodes with opposite chiralities, the Chern number becomes nonzero, $C(k_z) = -1$, while it remains zero otherwise as shown in Fig. 3.3 (a).

Interestingly, we have also discovered additional hidden symmetries. On the high symmetry plane with $k_y = 0$, the two-dimensional Hamiltonian $H_{(k_y=0)} = H(k_x, 0, k_z)$ possesses a chiral symmetry $\mathcal{S} = \tau_y \cdot \theta_x$, where $\mathcal{S}H_{(k_y=0)}\mathcal{S} = -H_{(k_y=0)}$, and the bulk Hamiltonian $H(\mathbf{k})$ given by Eq. (3.6) commutes with the unitary operator $\mathbf{R} = \tau_z \cdot \theta_z$. It is worth noting that $\mathbf{R}$ also commutes with $\mathcal{S}$. In the eigenbasis of $\mathbf{R}$, both the chiral symmetry $\mathcal{S}$ and $H(\mathbf{k})$ take the block diagonal form:

$$\mathcal{S}' = \begin{pmatrix} 0 & -i & 0 & 0 \\ i & 0 & 0 & 0 \\ 0 & 0 & 0 & -i \\ 0 & 0 & i & 0 \end{pmatrix} = \begin{pmatrix} \mathcal{S}'_1 & 0 \\ 0 & \mathcal{S}'_1 \end{pmatrix} \tag{3.10}$$

$$H'_{(k_y=0)} = \begin{pmatrix} H'_1(k_x, k_z) & 0 \\ 0 & H'_2(k_x, k_z) \end{pmatrix} \tag{3.11}$$

where

$$H'_1(k_x, k_z) = \begin{pmatrix} -1 + m + \Delta' - \cos k_x - \cos k_z & \sin k_x \\ \sin k_x & 1 - m - \Delta' + \cos k_x + \cos k_z \end{pmatrix} \tag{3.12}$$

$$H'_2(k_x, k_z) = \begin{pmatrix} -1 + m - \Delta' - \cos k_x - \cos k_z & \sin k_x \\ \sin k_x & 1 - m + \Delta' + \cos k_x + \cos k_z \end{pmatrix} \tag{3.13}$$

Therefore, each block $H'_{1,2}$ possesses chirality and can be interpreted as a SSH model [87], with k_z as a parameter. In the eigenbasis of the chiral symmetry $\mathcal{S}'_1$, we obtain:

$$\tilde{H}'_1(k_x, k_z) = \beta_{\mathcal{S}'_1}^{-1} H'_1(k_x, k_z) \beta_{\mathcal{S}'_1} = \begin{pmatrix} 0 & z_1 \\ z_1^* & 0 \end{pmatrix} \tag{3.14}$$

$$\tilde{H}'_2(k_x, k_z) = \beta_{\mathcal{S}'_1}^{-1} H'_2(k_x, k_z) \beta_{\mathcal{S}'_1} = \begin{pmatrix} 0 & z_2 \\ z_2^* & 0 \end{pmatrix} \tag{3.15}$$

with $\beta_{\mathcal{S}'_1}$ are transforming the operators to the eigenbasis of $\mathcal{S}'_1$ and,

$$z_1 = 1 - m - \Delta' + \cos k_x + \cos k_z + i \sin k_x \tag{3.16}$$

$$z_2 = 1 - m + \Delta' + \cos k_x + \cos k_z + i \sin k_x \tag{3.17}$$

Their winding number for each subspaces can be written as:

$$\nu_{1,2} = \frac{1}{2\pi i} \int_{-\pi}^{\pi} dk_x \frac{1}{z_{1,2}} \frac{\partial z_{1,2}}{\partial k_x}, \tag{3.18}$$

Figure 3.3 (b) and (c) illustrate the winding number of $H'_{(k_y=0)}$ (3.11) in each subspace of the chiral symmetry $\mathcal{S}'$, denoted as $\nu_{1,2}$, as a function of k_z. In the region $\pi/3 < |k_z| < 2\pi/3$, our additional symmetry aligns with the Chern number Eq. (3.9), indicating a topologically nontrivial system. Within each $\mathcal{N}_{k_z}$ plane, there are two helical edge states that are connected through the gap, as illustrated in Fig. 3.4 (a) and (c). Notably, this behavior is particularly prominent in the first diagonal block where $\nu_1 = 0$ and $\nu_2 = 1$. However, in the region $|k_z| < \pi/3$, despite possessing a zero Chern number, as demonstrated in Fig.3.3 (a), the planes $k_y = 0$ exhibit $\nu_{1,2} = 1$, implying a gap closing. This results in two pairs of helical edge states crossing the bulk gap, as depicted in Fig.3.4 (b). In this region, the ensemble of $\mathcal{N}_{k_z}$ planes can be interpreted as the BHZ model, as discussed in section 1.2, specifically corresponding to $H_{\mathbf{k}}^{BHZ}$ (1.20) with zero coupling between two Chern insulators $\Delta = 0$. This discovery represents a refinement of the analysis presented in the Reviews of Modern Physics [16], where we proposed that the inclusion of additional symmetries $\mathbf{R}$ at time-reversal invariant (TRI) momenta, $k_y = 0$, would enforce chirality within the spectrum. Consequently, this region hosts four flat bands interconnecting between the two Weyl nodes at $(0, 0, \pm\pi/3)$.
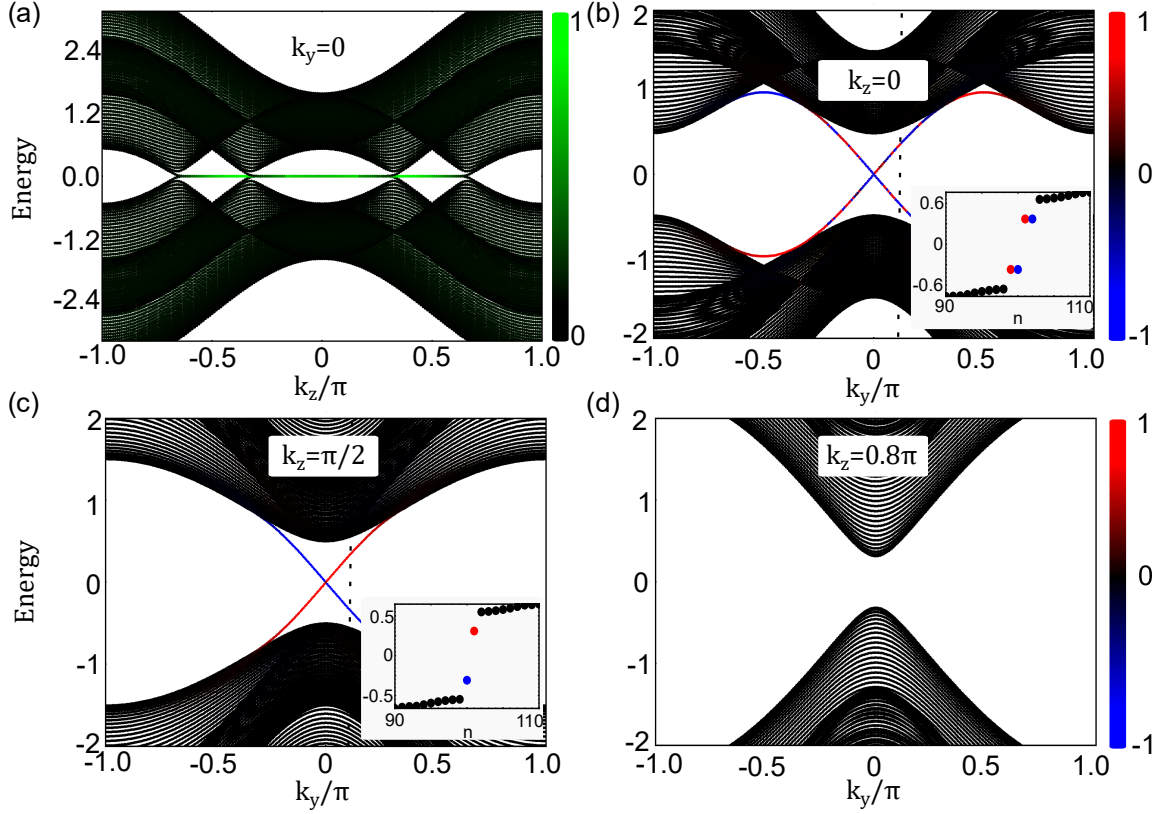
FIGURE 3.4: Surface spectrum of Hamiltonian. (3.6) with TRS breaking term $\theta_z \Delta'$ for (100) face with system width $L = 100$ unit cell as a function of surface momentum k_y, k_z (a) $k_y = 0$, green color indicate the projection of the eigenstates onto the edges of the system, (b) $k_z = 0$, (c) $k_z = \pi/2$, (d) $k_z = 0.8\pi$. Blue/Red color indicate the projection of the eigenstates onto the first/last unit cells located at the left (blue) and right (red) edge of the system. Inset (b) and (c): spectra at $k_y = 0.1\pi$, $k_z = 0$ and $k_z = \pi/2$, respectively. Here we set $m = 2.0, \Delta' = 0.5$.

Chapter 4

Higher order topological phases

4.1 Classification of higher order topological phases

The presence of different topological categories for band structures has an important practical implication: if the bulk band structure exhibits a nontrivial topology, it can suggest the presence of anomalous boundary states. These boundary states are referred to as "anomalous" because they cannot exist independently and rely on the topological properties of the bulk. These boundary states are resistant to local perturbations and can only be eliminated by a perturbation that either closes the energy gap in the bulk band structure or reduces its symmetry. This relationship between the nontrivial topology of the bulk band structure and the existence of anomalous boundary states is known as the bulk-boundary correspondence. In the case of topological phases that are governed solely by nonspatial symmetries like time-reversal symmetry or particle-hole antisymmetry found in the superconducting Bogoliubov-de Gennes Hamiltonian, the description of bulk-boundary correspondence is complete: Each topological class of a d-dimensional bulk band structure uniquely corresponds to an anomalous boundary state of dimension $d - 1$ and vice versa [44, 81]. As we have demonstrated in previous sections, for example from $d = 2$-nontrivial bulk to $d = 1$-boundary state in QWZ-BHZ model in section 1.2 or a bulk-boundary correspondence for topological phases that are also subject to spatial symmetries, such as mirror symmetries, in Chapter 2, there needs to be a certain level of compatibility between the crystal termination and the crystalline symmetries. Unfortunately, this criterion can be satisfied for only a few symmetry groups and limited to specific surface orientations. However, immediately after the discovery of topological crystalline band structures [32], it became apparent that the conventional bulk-boundary correspondence, where the anomalous boundary states of a crystal of dimension d possess a dimension of $d - 1$, is applicable only to topological crystalline insulators and not to strong topological insulators.

Recently, following pioneering work by Schindler et al. [80] it was realized that topological crystalline phases may also have anomalous boundary signatures of dimensions smaller than $d - 1$. For instance, anomalous states can emerge at the hinges or corners of three-dimensional crystals, or as anomalous corner states in two-dimensional crystals. Unlike the requirement for individual crystal faces to be invariant under crystalline symmetry, the condition that the overall crystal termination respects the crystalline symmetry group is a much weaker criterion on surface

orientations. Moreover,this condition can be satisfied for all crystalline symmetry groups. Such topological phases with these distinct boundary characteristics are referred to as higher-order topological phases. Or more precisely, topological phases which have boundary states of dimension $d - n$, are called "n^{th} order" where the order n^{th} indicates the codimension of the boundary states. For example, in chapter 2.2, the mirror symmetry protected surface states in topological crystalline insulators are called "first-order".

The boundary states that do (do not) have their origin in the topology of the bulk band structure are referred to as intrinsic (extrinsic). Even though extrinsic anomalous boundary states are associated with crystal termination, they still possess a certain level of topological protection. In particular, perturbations that respect the crystalline symmetries and do not close gaps along hinges or surfaces of the crystal cannot remove extrinsic corner states. Likewise, extrinsic hinge states remain immune to perturbations that preserve symmetry that do not close surface gaps. In this chapter, we provide a simplified model that has been featured in recent publications. This model demonstrates that a single mirror symmetry is enough to construct models for second-order topological insulators and superconductors.

4.2   Reflection-symmetric second-order topological phase

An explicit model realizing second-order topological topological superconductor with Majorana corner states is given by the four-band tight-binding Hamiltonian [48]:

$$H(\mathbf{k}) = (m - \cos k_1 - \cos k_2)\,\tau_y + \tau_x\theta_z \sin k_x + \tau_z \sin k_y + \lambda\tau_y\theta_x \qquad (4.1)$$

where

$$\theta_{x,y,z} \;\;=\;\; \mathbb{1}_2 \otimes \sigma_{x,y,z} \qquad\qquad (4.2)$$

$$\tau_{x,y,z} \;\;=\;\; \sigma_{x,y,z} \otimes \mathbb{1}_2 \qquad\qquad (4.3)$$

The system has particle-hole symmetry $\mathcal{P}$ and without loss of generality we may represent $\mathcal{P}$ by complex conjugation $\mathcal{K}$ and the reflection operation respect to k_x, $R = \theta_x$:

$$H(k_x, k_y) = -H^*(-k_x, -k_y) = \theta_x H(-k_x, k_y)\theta_x \qquad (4.4)$$

Additionally, there exists TRS: $\mathcal{T} = \theta_x \cdot \tau_x \mathcal{K}$. Therefore, we also have chiral symmetry. If we do not impose reflection symmetry, there is no topological property in BDI in two dimensions. With reflection symmetry, $H(k_x, k_y)$ commutes with R on the reflection symmetric plane, $k_x = 0, \pi$, and since reflection R commutes with chiral symmetry, the $M\mathbb{Z}$-topological invariant is defined by computing the winding number number in one of the eigenspaces of R. However, in terms of second order topology, at the TRI: $\tilde{\mathbf{k}} = (0,0), (0,\pi), (\pi,0), (\pi,\pi)$, $H(\mathbf{k})$ can be transformed into
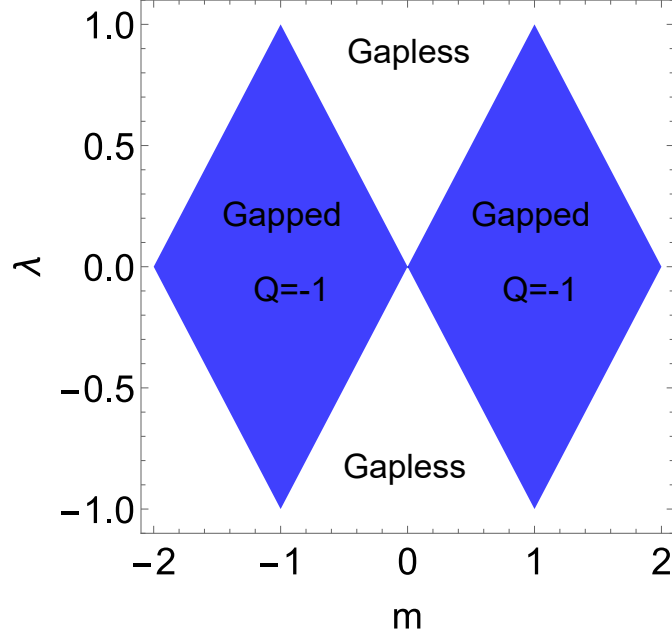
FIGURE 4.1: Phase diagram as function of the mass term m and spin-orbit coupling term λ. In the non-trivial region (shaded), the bulk spectrum is gapped and $\mathcal{Q} = -1$ independently on the choice of $\tilde{H}_{1,2}(\tilde{\mathbf{k}})$. The system is gapless in the white region.

antisymmetric form by the unitary operation:

$$\tilde{H}(\tilde{\mathbf{k}}) = \beta_R^{-1} H(\tilde{\mathbf{k}}) \beta_R = \begin{pmatrix} \tilde{H}_1 & 0 \\ 0 & \tilde{H}_2 \end{pmatrix} \tag{4.5}$$

$$\beta_R = \begin{pmatrix} 0 & -1 & 0 & 1 \\ 0 & 1 & 0 & 1 \\ -1 & 0 & 1 & 0 \\ 1 & 0 & 1 & 0 \end{pmatrix} \tag{4.6}$$

with β_R are transforming the operators to the eigenbasis of R. $\tilde{H}(\tilde{\mathbf{k}})$ take the two blocks diagonal form in which the two blocks of $\tilde{H}(\tilde{\mathbf{k}})$ are 2×2 antisymmetric matrices and on the reflection symmetric plane, $k_x = 0, \pi$, particle-hole symmetry $\mathcal{P}' = \mathcal{K}$ is the only relevant symmetry operation. Each block is a similar model to the Kitaev chains, which we have introduced in chapter 1. Thus, the second-order bulk topological invariant, $\mathbb{Z}_2$, can be defined by sign of the pfaffians at four TRI momenta of :

$$\begin{aligned} \mathcal{Q} &= \text{sign}\left(\prod_{\tilde{\mathbf{k}}} \text{Pf}\left[i\tilde{H}_1(\tilde{\mathbf{k}}) \right] \right) \\ &= \text{sign}\left[(2 - m + \lambda)(-m + \lambda)(-m + \lambda)(-2 - m + \lambda) \right] \end{aligned} \tag{4.7}$$

The phase diagram is shown in Fig. 4.1. The shaded region is the non-trivial phase,
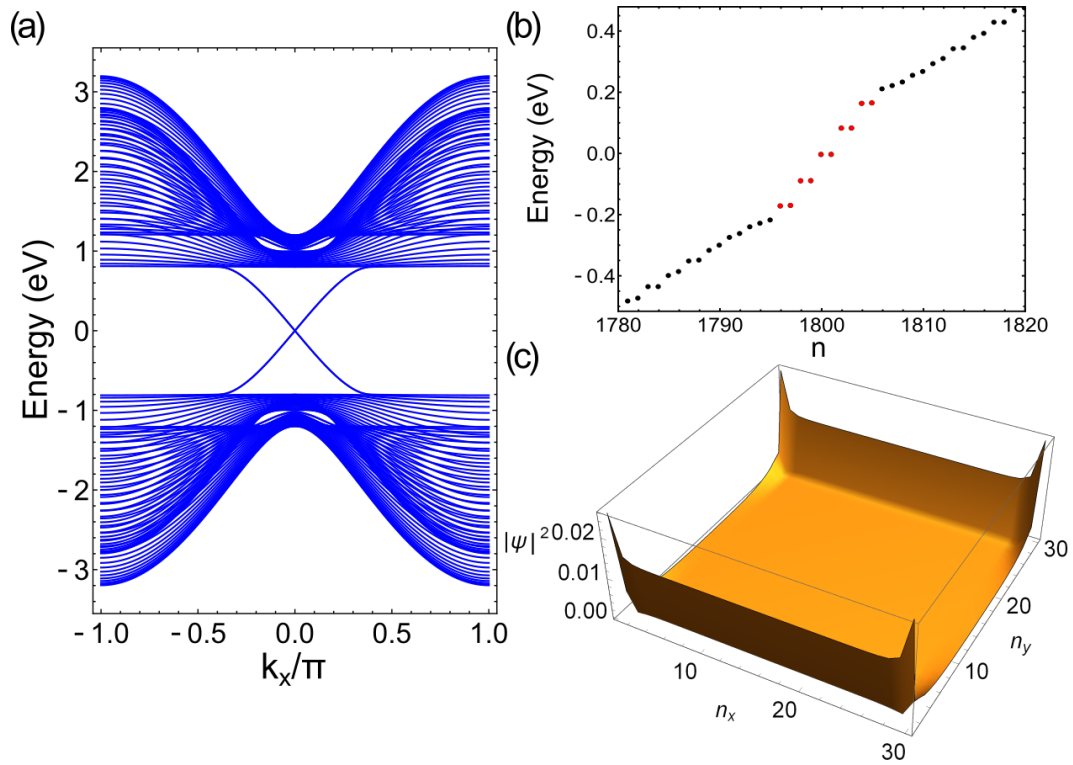
FIGURE 4.2: (a) Spectrum for a system with open boundary conditions in y-direction with system width $N_y = 30$ unit cells. A pair of gapless helical edge states connect through the gap. (b) Energy spectrum for a system with open boundary conditions in x- and y-directions. The size of the system is equal to $N_x = N_y = 30$ unit cells. The red dots are edge states. (c) LDOS of the in-gap states (red dots) in (b). Here we set $m = 1.0$ and $\lambda = 0.2$

$\mathcal{Q} < 0$. Notice that, in general, the choice of different eigenspaces of R: $\tilde{H}_1(\tilde{\mathbf{k}})$ (-1) or $\tilde{H}_2(\tilde{\mathbf{k}})$ $(+1)$ in Eq. (4.7) can lead to different topological invariants. However, it is important to highlight that in this shaded region the system is gapped and the results are identical. If we go to the lower dimension $d - 1$ with edge-termination compatible with the mirror symmetry, $\hat{y}$-quantized, we see a pair of helical edge states connected through the gapped and the open system spectrum hosting low-energy in-gap states localized at the edges respect to y-direction, shown in Fig. 4.2.

In order to construct second-order topological superconductors, the reflection symmetry has to be broken with a suitable choice of edge direction. Then the reflection symmetric topological crystalline phase, shown in Fig. 4.2, becomes trivial. Breaking the reflection symmetry can be obtained by a transformation:

$$H(k_x, k_y) \rightarrow H'(\tilde{k}_x, \tilde{k}_y) = H(\tilde{k}_x - \tilde{k}_y, \tilde{k}_y). \tag{4.8}$$

Now, the Hamiltonian no longer possesses reflection symmetry. The nontrivial topology of the corresponding AZ class in $d - 1$ dimensions ensures that the presence of a reflection-symmetry-breaking mass term, $m\tau_y$, that gaps out any boundary states existing, as shown in Fig. 4.3 (a), in the presence of reflection symmetry is unique. The open spectrum shows the appearance of zero-energy states at the two corners of the sample, since this mass term must be odd under reflection, as shown in Fig. 4.3 (b)-(c). As long as the bulk and edge gaps are not closed, these corner states are robust against a reflection-symmetry breaking perturbation.

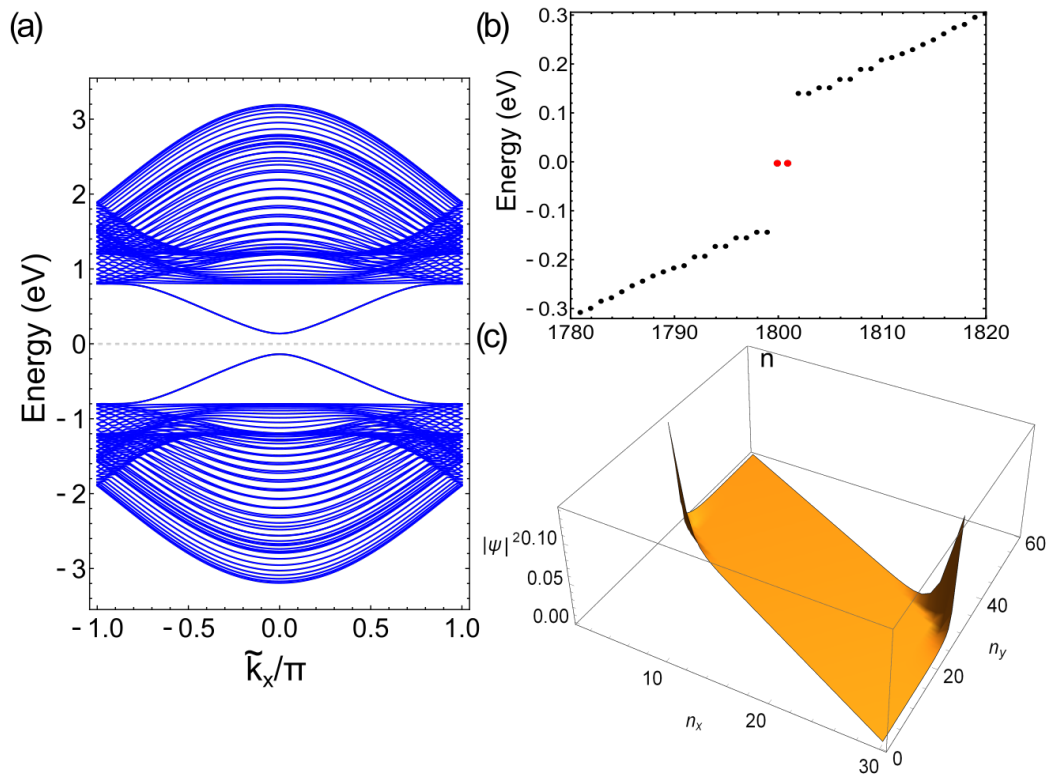FIGURE 4.3: (a) The spectrum of second order topologically nontrivial with system width $N_y = 30$ unit cell with the same model parameters as in Fig. 4.2. When the reflection-symmetry is broken, we observe an anti-crossing. (b) Spectrum for the case of open boundary conditions in both directions, $\tilde{N}_x = \tilde{N}_y = 30$, the red dots show the two zero-energy corner states. (c) LDOS of the corner states (red dots).

Chapter 5

Corner states, hinge states, and Majorana modes in SnTe nanowires

5.1 Summary

SnTe materials are renowned instances of experimentally achieved three-dimensional topological crystalline insulators [28, 38, 88, 96], as discussed in Chapter 2. Moreover, they have been predicted to facilitate diverse forms of lower-dimensional topological phases [10, 51, 52, 83] and higher-order topology [39, 80]. Notably, they hold promise for future investigations, given their demonstrated experimental potential to induce superconductivity [5, 9, 31, 71, 79, 98], generate significant Zeeman fields [25, 62, 63, 85, 86], and apply inversion-symmetry-breaking fields [13, 35, 42, 49, 73, 94]. In this paper, we have conducted a comprehensive investigation into the symmetries and topological properties of SnTe nanowires, proposing the utilization of adjustable symmetry-breaking fields to achieve various types of topological states. Upon describing the system, we analyze the effects of a parallel Zeeman field on the wire in the (001) direction, leading to four distinct phases depending on the Zeeman field magnitude and wire thickness: trivial insulator phase, one-dimensional Weyl semimetal phase, band-inverted insulator phase, and indirect semimetal phase. The band-inverted insulator regime is characterized by a pseudospin texture and hosts low-energy states localized at the corners of the wire, while the Weyl semimetal phase is protected by a non-symmorphic screw-axis rotation symmetry, with low-energy states localized at the hinges of the wire. The Weyl semimetal phase is a novel type of gapless topological phase, which has not been previously discussed in the classifications of gapless phases reviewed in Chapter. 3. We establish the relationship between these hinge states and the topological corner states found in two-dimensional Hamiltonians belonging to the Altland-Zirnbauer class DIII [1] with rotoinversion symmetry, and provide an analytical formula for the $\mathbb{Z}_2$ topological invariant characterizing their existence. The topological invariant discovered in this paper enriches the classification of higher order topological phases discussed in Chapter. 4. It is important to note that the topological nature of these states is related to the approximate symmetries of the SnTe nanowires, and the transverse mode energies do not follow simple parametric dependencies with respect to the nanowire thickness and the Zeeman field. This means that the SnTe nanowires cannot be described using a low-energy effective $k \cdot p$ theory as we have discovered. However, our approximations

are well-controlled, and our results are applicable for realistic nanowires. In the presence of superconductivity, we uncover inversion-symmetry-protected gapless topological bulk Majorana modes, leading to quantized thermal conductance in ballistic wires. Finally, by adding an inversion-symmetry-breaking field, the bulk Majorana modes become gapped and superconducting SnTe nanowires support topologically protected localized Majorana zero modes appearing at the ends of the wire. It worth noting that the strong topological invariant protecting the Majorana zero modes was discussed in Chapter. 1, but here we also provide a correspondence between a gapless topological phase in the presence of inversion symmetry and an appearance of a gapped topological phase upon breaking the inversion symmetry. Our results may open up new opportunities for controlling and creating Majorana zero modes by manipulating inversion-symmetry-breaking fields e.g. via ferroelectricity [13, 35, 42, 94]. We also propose various possibilities to experimentally probe the corner states, hinge states and Majorana modes.

5.2   Publication I

Date: 8 August 2023

STATEMENT

I declare that I am the co-author of the publication **N. M. Nguyen**, , W. Brzezicki ,T. Hyart, Corner states, hinge states, and Majorana modes in SnTe nanowires, PhysRevB.105, 075310 (2022).

My contribution was constructing the model, writing the codes, analyzing the results, preparing the figures and participating in writing the manuscripst.

Yours Faithfully,

Nguyen Minh Nguyen

Nguyen Minh Nguyen, Group ON-6.1 at the International Centre for Interfacing Magnetism and Superconductivity with Topological Matter (MagTop),
E-mail: nmnguyen@magtop.ifpan.edu.pl
Website: https://www.magtop.ifpan.edu.pl/resources/teams/

Date: 11 August 2023

STATEMENT

I declare that my contribution to the paper **N. M. Nguyen**, W. Brzezicki, T. Hyart, *Corner states, hinge states, and Majorana modes in SnTe nanowires*, Phys. Rev. B 105, 075310 (2022), has been related to the analysis of symmetries and formulation of topological invariants, formulation of the research questions for the project, exchange of ideas during regular meetings and writing part of the manuscript.

Yours Faithfully,

dr hab. Wojciech Brzezicki

Date: 6 August 2023

STATEMENT

I declare that my contribution to the paper **N. M. Nguyen**, W. Brzezicki, T. Hyart, Corner states, hinge states, and Majorana modes in SnTe nanowires, Phys. Rev. B 105, 075310 (2022), has been related to the formulation of the research questions for the project, exchange of ideas during regular meetings, writing part of the manuscript, and supervision of the project.

Yours Faithfully,

Timo Hyart

Timo Hyart
Research Fellow, Aalto University, E-mail: timo.hyart@aalto.fi
https://research.aalto.fi/en/persons/timo-hyart
https://scholar.google.fi/citations?user=fq1cObMAAAAJ&hl=fi

Corner states, hinge states, and Majorana modes in SnTe nanowires

Nguyen Minh Nguyen [1], Wojciech Brzezicki [1,2] and Timo Hyart[1,3]

[1]*International Research Centre MagTop, Institute of Physics, Polish Academy of Sciences,*
Aleja Lotnikow 32/46, PL-02668 Warsaw, Poland
[2]*Institute of Theoretical Physics, Jagiellonian University, ulica S. Łojasiewicza 11, PL-30348 Kraków, Poland*
[3]*Department of Applied Physics, Aalto University, 00076 Aalto, Espoo, Finland*

SnTe materials are one of the most flexible material platforms for exploring the interplay of topology and different types of symmetry breaking. We study symmetry-protected topological states in SnTe nanowires in the presence of various combinations of Zeeman field, s-wave superconductivity and inversion-symmetry-breaking field. We uncover the origin of robust corner states and hinge states in the normal state. In the presence of superconductivity, we find inversion-symmetry-protected gapless bulk Majorana modes, which give rise to quantized thermal conductance in ballistic wires. By introducing an inversion-symmetry-breaking field, the bulk Majorana modes become gapped and topologically protected localized Majorana zero modes appear at the ends of the wire.

I. INTRODUCTION

SnTe materials ($Sn_{1-x}Pb_xTe_{1-y}Se_y$) have already established themselves as paradigmatic systems for studying three-dimensional (3D) topological crystalline insulators and topological phase transitions, because the band inversion can be controlled with the Sn content [1–4], but they may have a much bigger role to play in the future investigations of topological effects. Robust 1D modes were experimentally observed at the surface atomic steps [5] and interpreted as topological flat bands using a model obeying a chiral symmetry [6]. Furthermore, the experiments indicate that these flat bands may lead to correlated states and an appearance of a robust zero-bias peak in the tunneling conductance at low temperatures [7]. Although, there has been a temptation to interpret the zero-bias anomaly as an evidence of topological superconductivity, all the observed phenomenology can be explained without superconductivity or Majorana modes [7–9]. On the other hand, the standard picture of competing phases in flat-band systems [10,11] indicates that in thin films of SnTe materials the tunability of the density with gate voltages may allow for the realization of both magnetism and superconductivity at the step defects.

The improvement of the fabrication of low-dimensional SnTe systems with a controllable carrier density has become increasingly pressing also because the theoretical calculations indicate that thin SnTe multilayer systems would support a plethora of 2D topological phases, including quantum spin Hall [12,13] and 2D topological crystalline insulator phases [8,14]. The realization of a 2D topological crystalline insulator phase would be particularly interesting, because in these systems a tunable breaking of the mirror symmetries would open a path for new device functionalities [14]. Indeed, the recent experiments in thin films of SnTe materials indicate that the transport properties of these systems can be controlled by intentionally breaking the mirror symmetry [15]. Furthermore, SnTe materials are promising candidate systems for studying the higher order topology [16,17]. Thus, it is an outstanding challenge to develop approaches for probing the hinge and corner states in these systems.

In addition to the rich topological properties, SnTe materials are also one of the most flexible platforms for studying the interplay of various types of symmetry breaking fields. The superconductivity can be induced via the proximity effect or by In-doping, and both theory and experiments indicate rich physics emerging as a consequence [18–25]. Interesting topological phases are predicted to arise also in the presence of a Zeeman field [26], which breaks the time-reversal symmetry. In experiments, the Zeeman field can be efficiently applied with the help of external magnetic field by utilizing the huge g factor $g \sim 50$ [27,28], or it can be introduced with the help of magnetic dopants [29–31]. While the magnetism and superconductivity are part of the standard toolbox for designing topologically nontrivial phases, the SnTe materials offer also unique opportunities for controlling the topological properties by breaking the crystalline symmetries. In particular, it is possible to break the inversion symmetry by utilizing ferroelectricity or a structure inversion asymmetry [32–37]. This has already enabled the realization of a giant Rashba effect, and it may be important also for the topology.

So far the topological properties of SnTe nanowires have received little attention experimentally, but this may soon change due to the continuous progress in their fabrication [38,39]. In this paper, we systematically study the symmetries and topological invariants in SnTe nanowires and propose to utilize the tunable symmetry-breaking fields for realizing different types of topological states. After describing the system (Sec. II), we consider Zeeman field parallel to the wire and show that depending on the Zeeman field magnitude and the wire thickness there exists four qualitatively

different behaviors around the charge neutrality point: trivial insulator regime, one-dimensional Weyl semimetal phase, band-inverted insulator regime and indirect semimetal phase (Sec. III). We show that the band-inverted insulator regime is characterized by a pseudospin texture and an appearance of low-energy states localized at the corners of the wire, whereas the Weyl semimetal phase is protected by a nonsymmorphic screw-axis rotation symmetry (fourfold rotational symmetry) in the case of even (odd) thicknesses, and the low-energy states are localized at the hinges of the wire. We uncover how these hinge states are related to the topological corner states appearing in two-dimensional Hamiltonians belonging to the Altland-Zirnbauer class DIII [40] in the presence of a rotoinversion symmetry, and we explicitly construct an analytical formula for a $\mathbb{Z}_2$ topological invariant describing their existence (Sec. IV). In the presence of superconductivity (Sec. V), we find inversion-symmetry-protected gapless topological bulk Majorana modes, which give rise to quantized thermal conductance in ballistic wires. Finally, we show that by introducing an inversion-symmetry-breaking field, the bulk Majorana modes become gapped and topologically protected localized Majorana zero modes appear at the ends of the wire.

II. HAMILTONIAN AND ITS SYMMETRIES

Our starting is the *p*-orbital tight-binding Hamiltonian

$$
\mathcal{H}(\mathbf{k}) = m\mathbb{1}_2 \otimes \mathbb{1}_3 \otimes \Sigma + t_{12} \sum_{\alpha=x,y,z} \mathbb{1}_2 \otimes (\mathbb{1}_3 - L_\alpha^2) \otimes h_\alpha(k_\alpha)
$$

$$
+ t_{11} \sum_{\alpha \neq \beta} \mathbb{1}_2 \otimes \left[\mathbb{1}_3 - \frac{1}{2}(L_\alpha + \epsilon_{\alpha\beta} L_\beta)^2 \right]
$$

$$
\otimes h_{\alpha,\beta}(k_\alpha, k_\beta)\Sigma + \sum_{\alpha=x,y,z} \lambda_\alpha \, \sigma_\alpha \otimes L_\alpha \otimes \mathbb{1}_8, \tag{1}
$$

which has been used for describing the bulk topological crystalline insulator phase in the SnTe materials [1] and various topological phases in lower dimensional systems [5,8]. Here we have chosen a cubic unit cell containing eight lattice sites (Fig. 1), Σ is a diagonal 8×8 matrix with entries $\Sigma_{i,i} = \mp 1$ at the two sublattices (Sn and Te atoms), $\varepsilon_{\alpha\beta}$ is Levi-Civita symbol, $L_\alpha = -i\varepsilon_{\alpha\beta\gamma}$ are the 3×3 angular momentum $L = 1$ matrices, σ_α are Pauli matrices, and $h_\alpha(k_\alpha)$ and $h_{\alpha,\beta}(k_\alpha, k_\beta)$ are 8×8 matrices describing hopping between the nearest-neighbors and next-nearest-neighbor sites, respectively (see Appendix A). In investigations of topological properties it is useful to allow the spin-orbit coupling to be anisotropic, hence λ_α, although the reference physical case is $\lambda_\alpha \equiv \lambda$. When not otherwise stated we use $m = 1.65$ eV, $t_{12} = 0.9$ eV, $t_{11} = 0.5$ eV, and $\lambda = 0.3$ eV.

We first consider an infinite nanowire along the z direction with $N_x = N_y$ unit cells in x and y directions. The Hamiltonian for the nanowire $\mathcal{H}^{1D}(k_z)$ can be constructed using Hamiltonian (1) and it satisfies a fourfold screw-axis symmetry (see Appendix A)

$$
S_c(k_z) = P_z \otimes e^{-i\frac{\pi}{4}\sigma_z} \otimes e^{-i\frac{\pi}{2}L_z} \otimes s_c(k_z), \tag{2}
$$

where P_z and $s_c(k_z)$ realize a transformation of the lattice sites, consisting of a translation by a half lattice vector and $\pi/2$ rotation with respect to the z axis (Fig. 1), between the unit
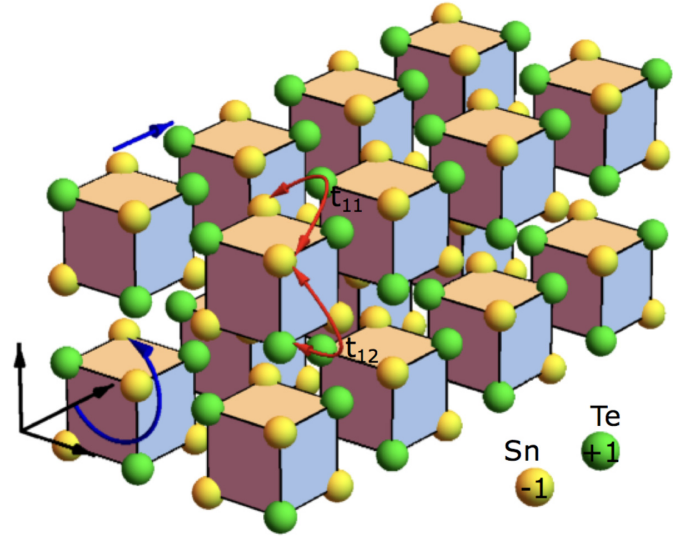

FIG. 1. Schematic view of the system. The blue arrow indicates the screw-axis operation, including a $\pi/2$ rotation with respect to the z axis and a half-lattice vector translation. The red arrows depict the nearest-neighbor (t_{12}) and the next-nearest-neighbor (t_{11}) hopping terms in Hamiltonian (1). The two sublattices, corresponding to Sn and Te atoms, have opposite on-site energies.

cells and inside the unit cell, respectively (see Appendix A). Additionally, there exists also glide plane symmetries $M_x(k_z)$ ($M_y(k_z)$) consisting of a mirror reflection with respect to the $\hat{x}$ ($\hat{y}$) plane and a half-lattice translation along the z axis and diagonal mirror symmetries M_{xy} (M_{yx}) with respect to the $\hat{x} + \hat{y}$ ($\hat{x} - \hat{y}$) planes. The product of $M_x(k_z)$ with $M_y(k_z)$ or M_{xy} with M_{yx} yields a twofold rotation symmetry with respect to the z axis. All these symmetry act at any k_z can be used to block diagonalize the 1D Hamiltonian. The mirror symmetry $M_z(k_z)$ with respect to the z plane acts on the Hamiltonian as $M_z(k_z)\mathcal{H}^{1D}(k_z)M_z(k_z)^\dagger = \mathcal{H}^{1D}(-k_z)$ and the inversion symmetry operator can be constructed as $I \propto M_x(k_z)M_y(k_z)M_z(k_z)$.

If the wire has odd number of atoms in x and y directions, it cannot be constructed from full unit cells, and this influences the symmetries of the system. In particular, for odd thicknesses the screw-axis rotation symmetry is replaced by an ordinary fourfold rotation symmetry.

III. TOPOLOGICAL STATES IN THE PRESENCE OF ZEEMAN FIELD

In this section, we study the properties of the system in the presence of Zeeman field $\mathcal{H}_Z = \mathbf{B} \cdot \vec{\sigma}$ applied along the wire $\mathbf{B} = (0, 0, B_z)$. This field breaks the time-reversal symmetry T and the mirror symmetries $M_x(k_z)$, $M_y(k_z)$, M_{xy} and M_{yx}, but it preserves the inversion symmetry I, the mirror symmetry $M_z(k_z)$ and the screw-axis symmetry $S_c(k_z)$. We find that as a function of Zeeman field magnitude and the wire thickness there exists four qualitatively different behaviors around the charge neutrality point: trivial insulator regime, 1D Weyl semimetal phase, band-inverted insulator regime and indirect semimetal phase (Fig. 2). The differences between these phases are summarized in Figs. 3–5.
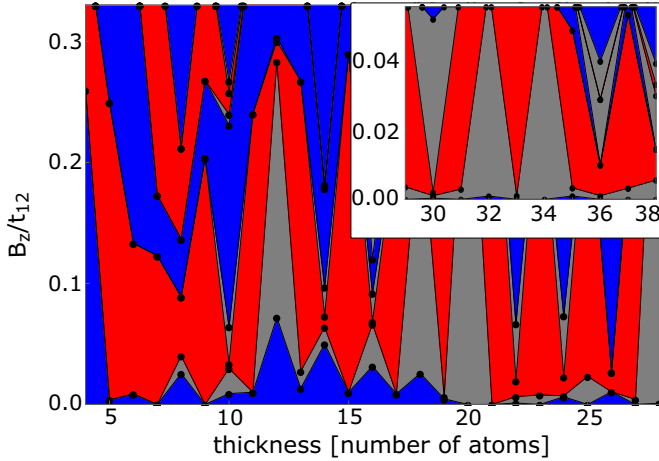
FIG. 2. Phase diagram as function of the nanowire thickness (dimensions of the square cross section) and Zeeman field B_z. The different phases are: insulator phase (blue), Weyl semimetal phase (red) and indirect semimetal phase (grey). In the regime of large Zeeman field the insulator phase supports a pseudospin texture due to band inversion, resulting in the appearance of localized corner states (see Fig. 5). Dots show the actually computed phase boundaries at discrete values of the wire thickness.

FIG. 4. (a) Low-energy band structure in the Weyl semimetal phase for a four-atoms-thick nanowire and $B_z = 0.3t_{12}$. The different colors indicate various S_c eigenvalue subspaces. (b) Band crossings around $k_z = \pi$. (c) Energy spectrum of 200-atoms long wire. (d) Band structure of 26-atoms-thick nanowire at $B_z = 0.012t_{12}$. At the band-crossing point (red dot) the states are localized in the hinges of the wire. Inset: LDOS (normalized with the maximum value) projected to the square cross section of the wire.

In the case of small Zeeman field B_z we find a trivial insulating phase or an indirect semimetal phase depending on the wire thickness. Neither of these phases supports in-gap states localized at the ends of the wire. By increasing B_z we find that there appears a Weyl semimetal phase for a range of wire thicknesses and Zeeman field magnitudes (Figs. 2 and 4). For even thicknesses of the wire the band crossings (Weyl points) are protected by the non-symmorphic screw-axis rotation symmetry $S_c(k_z)$, which allows us to decompose the Hamiltonian into four diagonal blocks, so that the energies of eigenstates belonging to different blocks (indicated with
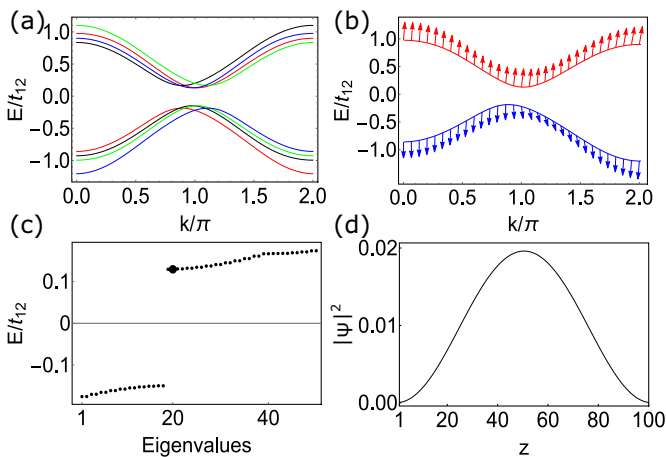
different colors in Fig. 4) can cross. Due to this reason a change in the number of eigenstates belonging to specific eigenvalues of the screw-axis rotation symmetry below the Fermi level as a function of k_z can be used as a topological invariant for the Weyl semimetal phase. In the case of odd thicknesses the screw-axis rotation symmetry is replaced by an ordinary fourfold rotational symmetry, but also this symmetry can be utilized to block diagonalize the Hamiltonian at any k_z, and therefore it can protect the Weyl semimetal phase

FIG. 3. (a) Low-energy band structure in the trivial insulator phase. The different colors indicate the various S_c eigenvalue subspaces. (b) The sublattice pseudospin texture for a pair of bands with the same S_c eigenvalue. The texture is in-plane because $\langle \tau_y \rangle$ is negligible. (c) Energy spectrum of 200 atoms long wire showing no end states. (d) LDOS for the bulk state highlighted in plot (c). The thickness of the wire is 4 atoms and $B_z = 0.1t_{12}$.

FIG. 5. (a) Low-energy band structure in the band-inverted insulator phase for the four-atoms-thick nanowire and $B_z = 0.4t_{12}$. (b) The sublattice pseudospin texture for a pair of bands with the same S_c eigenvalue. (c) Energy spectrum for 200 atoms long wire. The red points indicate eight corner states and black points are bulk states. (d) LDOS as a function of z for the corner states (red line) and a bulk state (black line). Inset: LDOS (normalized with the maximum value) as a function of x and y for the corner states in a 6 atoms thick nanowire.

in a analogous way. Note that due to non-symmorphic character of $S_c(k_z)$ the S_c subblocks of $\mathcal{H}^{1D}(k_z)$ are 4π-periodic and they transform into each other in 2π rotations. Because symmetries guarantee that the spectrum is symmetric around $k_z = \pi$, this elongated period leads to forced band crossings at $k_z = \pi$, see Figs. 3–5(a). However, the forced band crossings typically appear away from the zero energy (Figs. 3 and 5) and therefore they do not guarantee the existence of Weyl semimetal phase at the charge neutrality point. In the Weyl semimetal phase shown in Fig. 4 the crossings occur between an electronlike band and a holelike band carrying different S_c eigenvalues so that there necessarily exists states at all energies. As demonstrated by calculating the local density of states (LDOS) in Fig. 4(d) the states connecting the conduction and valence bands are often found to be localized at the hinges of the nanowire. We discuss the origin of these hinge states in Sec. IV.

By increasing B_z further we find another insulating phase for a wide range of wire thicknesses and Zeeman field magnitudes. In this case, the band dispersions have the camel's back shape [Fig. 5(a)] which typically appears in topologically nontrivial materials, but we have checked that these band structures can be adiabatically connected to the trivial insulator phase, and therefore the topological nature may only be related to an approximate symmetry of the system. Nevertheless, the bands support a nontrivial pseudospin texture $\langle \vec{\tau} \rangle_p = \langle \psi_p(k) | \vec{\tau} | \psi_p(k) \rangle$, where the pseudospin operators τ_α are the Pauli matrices acting in the sublattice space. In the high-field insulating phase the pseudospin component $\langle \tau_y \rangle_p$ is negligible and the pseudospin direction rotates in two-dimensional $(\langle \tau_x \rangle_p, \langle \tau_z \rangle_p)$ space so that its direction is inverted around $k_z = \pi$ [see Fig. 5(b)], whereas in the low-field insulator phase the sublattice pseudospin texture is trivial [Fig. 3(b)]. Therefore we call the insulating phases band-inverted and trivial insulators, respectively. The band-inverted insulator phase also supports subgap end states localized at the corners of the wire [Figs. 5(c) and 5(d)], whereas no subgap end states can be found in the trivial insulator phase [Figs. 3(c) and 3(d)].

We emphasize that the thin nanowires are used here only for illustration purposes because in these cases the strengths of the Zeeman fields required for realizing the different behaviors of the system are not experimentally feasible. However, with increasing thickness of the nanowires the Weyl semimetal and band-inverted phases occur at smaller values of B_z, so that in the case of a realistic thickness they can be accessed with feasible magnitudes of the Zeeman field. The inset of Fig. 2 shows a zoom into the experimentally most relevant regime of the phase diagram.

The Weyl points are protected by the screw-axis symmetry (or fourfold rotation symmetry) which is broken if the Zeeman field is rotated away from the z axis. However, if we utilize an approximation $\lambda_z = 0$ and $\lambda_x = \lambda_y = \lambda$, there exists also a nonsymmorphic chiral symmetry $S_z(k_z)$, and it is possible to combine it with $M_z(k_z)$ and time-reversal T to construct an antiunitary operator that anticommutes with $\mathcal{H}^{1D}(k_z)$ for any k_z. This operator squares to $+1$ and gives rise to a Pfaffian-protected Weyl semimetal phase also when the Zeeman field is not along the z axis (Appendix B). We also point out that if the screw-axis symmetry (or fourfold rotational symmetry) is broken so that the system supports
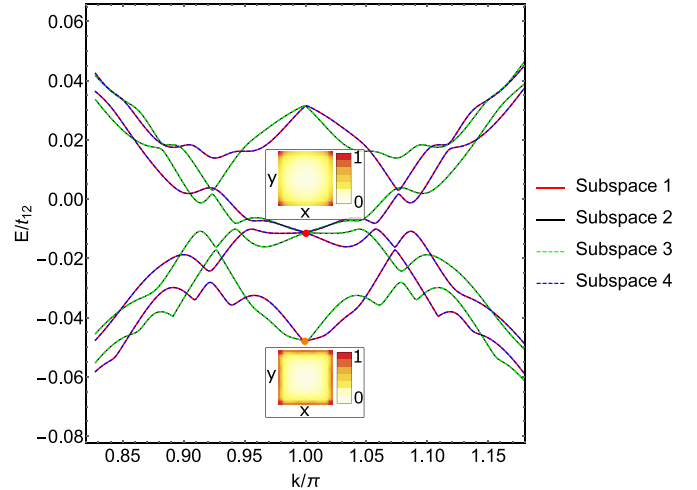

FIG. 6. Low-energy band structure and the LDOS (normalized with the maximum value) demonstrating the existence of hinge states in the absence of Zeeman field **B** = 0 for 50 atoms thick nanowire.

only a twofold rotational symmetry (e.g., due to anisotropic spin-orbit coupling or rectangular nanowires with $N_x \neq N_y$), the twofold rotational symmetry can still protect the existence of the Weyl points (Appendix C).

IV. HINGE STATES

We find that in addition to the Weyl semimetal phase at $B_z \neq 0$ [Fig. 4(d)], the hinge states appear also in the absence of Zeeman field [Fig. 6], and they resemble the protected states appearing in higher-order topological phases [16,41–43]. SnTe materials have been acknowledged as promising candidates for higher-order topological insulators but the gapless surface Dirac cones appearing at the mirror-symmetric surfaces make the experimental realization difficult [16]. This problem can be avoided if the system supports a 2D higher-order topological invariant for a specific high-symmetry plane in the **k** space where the surface states are gapped; this plane is shown in Fig. 7. To explore this possibility, we study the bulk Hamiltonian $\mathcal{H}(k_1, k_2, k_3)$ describing a system with inequivalent atoms at positions $(0, 0, \pm 1/2)$ and lattice vectors $a_1 = (1, 0, 1)$, $a_2 = (0, 1, 1)$ and $a_3 = (0, 0, 2)$ (see Appendix D1). We find that the 2D Hamiltonian $\mathcal{H}(k_1, k_2, \pi)$ with **B** = 0 supports edge states [red lines in Figs. 8(a) and 8(b)], but a small energy gap is opened due to $\lambda_x = \lambda_y = \lambda$ spin-orbit coupling terms. The spectrum is similar both for $\lambda_z = 0$ [Fig. 8(a)] and $\lambda_z = \lambda$ [Fig. 8(b)] so that neglecting λ_z is a good approximation. Moreover, the numerics indicates that two adjacent edges of the system are topologically distinct leading to appearance of zero-energy corner states at their intersection [Figs. 8(c) and 8(d)].

We find that the presence of the corner states is described by a $\mathbb{Z}_2$ topological invariant. To construct the invariant, we note that $\mathcal{H}(k_1, k_2, \pi)$ with $\lambda_z = 0$ obeys a chiral symmetry $S_z = \sigma_z \otimes \mathbb{1}_3 \otimes \tau_x$, where σ_z refers to spin, $\mathbb{1}_3$ to orbitals and τ_x to sublattice degrees of freedom. The Hamiltonian also obeys the time-reversal symmetry $T = \sigma_y \otimes \mathbb{1}_3 \otimes \mathbb{1}_2$, which anticommutes with S_z, so that the Hamiltonian belongs to
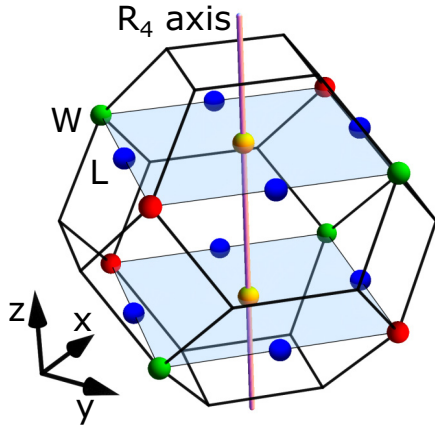
FIG. 7. Brillouin zone of the rocksalt crystals. The shaded planes form a $k_3 = \pi$ plane. The blue balls (L points) are the high-symmetry points $k_{1,2} = 0, \pi$ within the $k_3 = \pi$ plane. The yellow balls are the fourfold rotation R_4 centers at $(k_1, k_2) = (\pi, \pi)/2$ and $(k_1, k_2) = (3\pi, 3\pi)/2$. The red and green balls are the rotoinversion centers (W points) at $(k_1, k_2) = (\pi, 3\pi)/2$ and $(k_1, k_2) = (3\pi, \pi)/2$, respectively.

class DIII. In the eigenbasis of S_z the Hamiltonian and time-reversal operator have block-off-diagonal forms

$$\mathcal{H}(k_1, k_2, \pi) = \begin{pmatrix} 0 & u(k_1, k_2) \\ u^\dagger(k_1, k_2) & 0 \end{pmatrix} \quad (3)$$

and

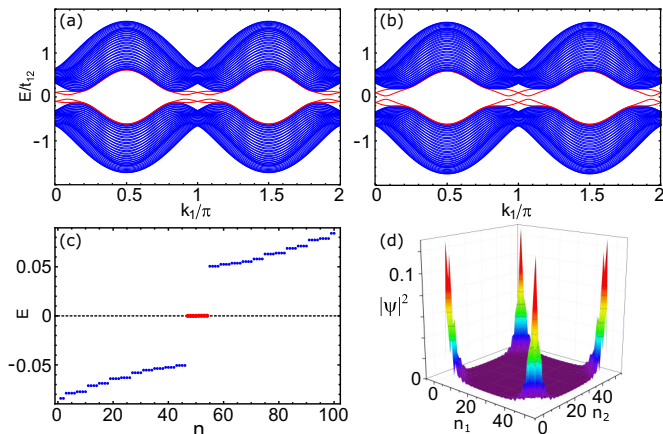$$T = \begin{pmatrix} 0 & -i\mathbb{1}_6 \\ i\mathbb{1}_6 & 0 \end{pmatrix}. \quad (4)$$

FIG. 8. (a) Low-energy spectrum of the Hamiltonian $\mathcal{H}(k_1, k_2, k_3 = \pi)$ for $\lambda_z = 0$ in the case of open boundary conditions in the a_2 direction. The width of the system is 50 unit cells. (b) The low-energy spectrum in the case of uniform spin-orbit coupling $\lambda_\alpha = \lambda$ ($\alpha = x, y, z$). (c) Spectrum for $\lambda_z = 0$ in the case of open boundary conditions in both a_1 and a_2 directions. The red dots show the eight zero-energy corner states. The system size is 50×50 unit cells. (d) LDOS of the corner states. Here, n_1 and n_2 label the unit cells in the directions of a_1 and a_2, respectively.

Thus, $u(k_1, k_2)^T = -u(-k_1, -k_2)$ and therefore we can define a Pfaffian at the time-reversal invariant points $\mathbf{K}$

$$p = \mathrm{Pf}\, u(\mathbf{K}) \quad (5)$$

By utilizing inversion symmetry $I = \mathbb{1}_2 \otimes \mathbb{1}_3 \otimes \tau_z$ we get that p is a real number (see Appendix D2). In our model p can be evaluated explicitly and it takes the form

$$p = (m - 4t_{11})(m + 2t_{11})^2 - 2m\lambda^2. \quad (6)$$

Notice that p is the same for all time-reversal invariant points $\mathbf{K}$ in the (k_1, k_2) plane due to the symmetries of the model (see Appendix D1). In the usual notation of the 3D Brillouin zone of the rocksalt crystals, the time-reversal invariant points $\mathbf{K}$ in the (k_1, k_2) plane correspond to the L points (see Fig. 7).

Interestingly, we find that p does not give a complete description of the presence of the corner states, because we also need to consider the high-symmetry point $\mathbf{K'} = (\pi/2, 3\pi/2)$. This point is a rotoinversion center, so that in the eigenbasis of the rotoinversion operator the Hamiltonian takes a block-diagonal form

$$\mathcal{H}(\mathbf{K'}) = \begin{pmatrix} h_1 & 0 & 0 & 0 \\ 0 & h_2 & 0 & 0 \\ 0 & 0 & h_3 & 0 \\ 0 & 0 & 0 & h_4 \end{pmatrix}. \quad (7)$$

By utilizing the chiral symmetry, inversion symmetry and time-reversal symmetry we find that (see Appendix D3)

$$\det[\mathcal{H}(\mathbf{K'})] = d^4, \quad (8)$$

where $d \equiv \det h_1 = \det h_4 = -\det h_2 = -\det h_3$, and therefore d changes sign at the zero-energy gap closing occurring at the momentum $\mathbf{K'}$. In our model d can be evaluated analytically and it takes the form

$$d = \det v_1 = m\big((m - 2t_{11})^2 + 4t_{12}^2\big) - 2(m - 2t_{11})\lambda^2. \quad (9)$$

In the usual notation of the 3D Brillouin zone of the rocksalt crystals, the rotoinversion centers $\mathbf{K'}$ are the W points (see Fig. 7).

The $\mathbb{Z}_2$ invariant ν can be determined using d and p as

$$\nu = (1 - \mathrm{sgn}(pd))/2. \quad (10)$$

The topological phase diagram in the m—λ plane is given in Fig. 9(a). By comparing to the corner state spectrum shown in Fig. 9(b), we find that ν describes the appearance of the corner states perfectly in our model. In the nontrivial phase $\nu = 1$, there are two localized states at every corner. They are Kramers partners and carry opposite chirality eigenvalues. We emphasized that the topological invariant (10) is not directly related to topological crystalline insulator invariant of the SnTe materials (see Fig. 10). Therefore, we expect that it is possible to find material compositions supporting the higher-order topological phase outside the topological crystalline insulator phase and vice versa.

V. MAJORANA MODES IN THE PRESENCE OF SUPERCONDUCTIVITY

Majorana zero modes are intensively searched non-Abelian quasiparticles which hold a promise for topological
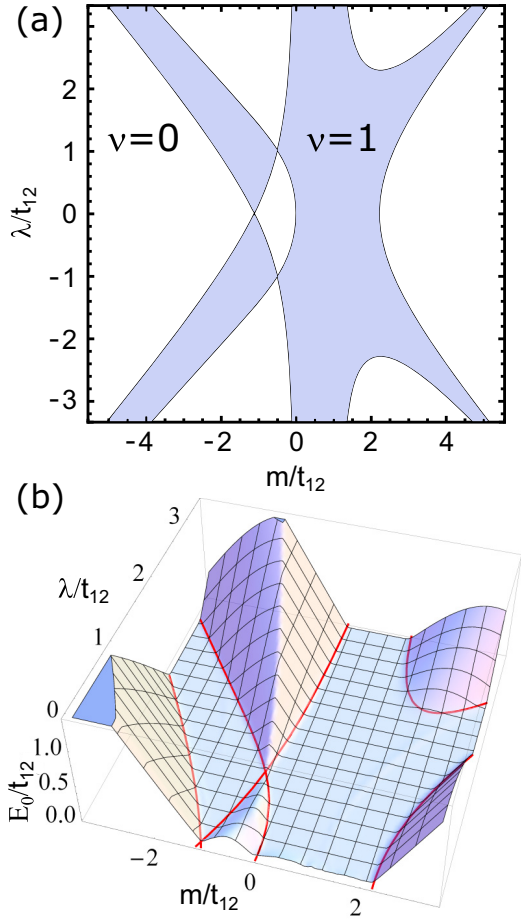
FIG. 9. (a) Topological invariant ν [Eq. (10)] of the 2D Hamiltonian $\mathcal{H}(k_1, k_2, \pi)$ in the chiral limit $\lambda_z = 0$ and $\lambda_x = \lambda_y = \lambda$ as function of m and λ. The shaded region is the non-trivial phase $\nu = 1$ supporting corner states. (b) Energy of a state being closest to the zero energy in the system with all edges open, as function of m and λ. The red lines are phase boundaries from (a). The system size is 50×50 unit cells.

FIG. 10. Topological phase diagram of Hamiltonian $\mathcal{H}(k_1, k_2, k_3)$ in the m—λ plane. Colors indicate different mirror M_{xy} Chern numbers C_+ defined in the k_1—k_3 plane (with $k_2 = k_1$). Areas bounded by the dashed line and filled with checkerboard pattern are nontrivial in the sense of ν invariant of Eq. (10), also shown in Fig. 9. The chiral limit is assumed with $\lambda_z = 0$ and $\lambda_x = \lambda_y = \lambda$.

quantum computing [44–46]. The key ingredients for realizing Majorana zero modes are usually thought to be spin-orbit coupling (spin-rotation-symmetry breaking field), magnetic field (time-reversal-symmetry breaking field), and superconductivity [47], and there exists a number of candidate platforms for studying Majorana zero modes including chains of adatoms [48–50] and various strong spin-orbit coupling materials in the presence of superconductivity and magnetism [51–54]. SnTe materials are particularly promising candidates for this purpose because in addition to the strong spin-orbit coupling they offer flexibility for introducing symmetry breaking fields such as superconductivity, magnetism, and inversion-symmetry breaking fields.

In the presence of induced s−wave superconductivity the Bogoliubov–de Gennes Hamiltonian for the nanowires has the form

$$H^{sc}(k_z) = \begin{pmatrix} \mathcal{H}^{1D}(k_z) - \mu & i\sigma^y \Delta \\ -i\sigma^y \Delta & -(\mathcal{H}^{1D}(-k_z)^T - \mu) \end{pmatrix}, \quad (11)$$
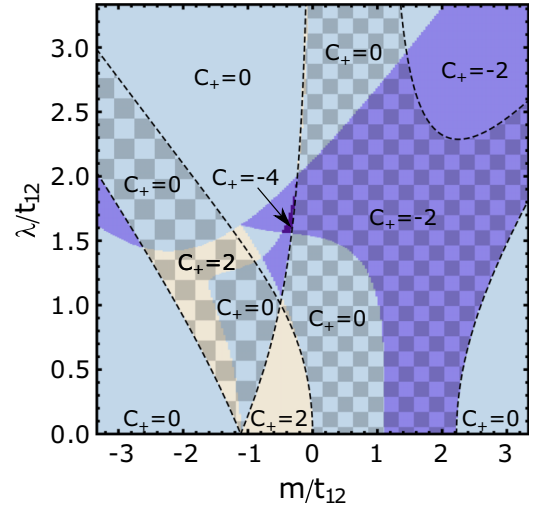
where σ_y acts in the spin space. This Hamiltonian obeys a particle-hole symmetry

$$C^{sc} H^{sc}(-k_z)^T C^{sc} = -H^{sc}(k_z), \quad (12)$$

where

$$C^{sc} = \begin{pmatrix} 0 & \mathbb{1} \\ \mathbb{1} & 0 \end{pmatrix}. \quad (13)$$

We can utilize C^{sc} to perform a unitary transformation on the Hamiltonian so that in the new basis the Hamiltonian $H_U^{sc}(k_z)$ is antisymmetric at $k_z = 0, \pi$ and $\text{Pf} H_U^{sc}(k_z = 0, \pi) \in \mathbb{R}$ (see Appendix E1). Since $iH_U^{sc}(0, \pi) \in \mathbb{R}$ we use real Schur decomposition to evaluate the Pfaffian in a numerically stable way, as suggested in Ref. [55]. Therefore, we can define a $\mathbb{Z}_2$ topological invariant as

$$\nu_{sc} = \left(1 - \text{sgn}\left[\text{Pf} H_U^{sc}(0)\text{Pf} H_U^{sc}(\pi)\right]\right)/2. \quad (14)$$

This is the strong topological invariant of 1D superconductors belonging to the class D. In fully gapped 1D superconductors the $\nu_{sc} = 1$ phase supports unpaired Majorana zero modes localized at the end of the wire.

The Hamiltonian (11) also satisfies an inversion symmetry

$$I^{sc}(k_z) = \begin{pmatrix} I(k_z) & 0 \\ 0 & I(k_z) \end{pmatrix}. \quad (15)$$

The product of C^{sc} and $I^{sc}(k_z)$ is an antiunitary chiral operator, which allows to perform another unitary transformation on the Hamiltonian, so that in the new basis the Hamiltonian $H_V^{sc}(k_z)$ is antisymmetric at all values of k_z and $\text{Pf} H_V^{sc}(k_z) \in \mathbb{R}$ (see Appendix E2). Therefore, consistently with classification of gapless topological phases [56], we can define an inversion-symmetry protected $\mathbb{Z}_2$ topological invariant for all values of k_z as

$$\nu_I(k_z) = \left(1 - \text{sgn}\left[\text{Pf} H_V^{sc}(k_z)\right]\right)/2. \quad (16)$$

If this invariant changes as a function of k_z there must necessarily be a gap closing. Thus, it enables the possibility of a topological phase supporting inversion-symmetry protected gapless bulk Majorana modes. Here, we use the term Majorana in the same way as it is standardly used in the physics literature, such as Refs. [57], so that it can be used to refer to all Bogoliubov quasiparticles in superconductors. In the presence of inversion symmetry the protection of the gapless Majorana bulk modes is similar to the Weyl points in Weyl semimetals: They can only be destroyed by merging them in a pairwise manner. The experimental signature of the Majorana bulk modes in ballistic wires is quantized thermal conductance $G_{\text{th}} = (G_0/2) \sum_n T_n$ in units of thermal conductance quantum $G_0 = \pi^2 k_B^2 T/(3h)$, because for ballistic wires with length larger than the decay length of the gapped modes the transmission eigenvalues for the gapless (gapped) modes are $T_n = 1$ ($T_n = 0$) and the number of gapless Majorana bulk modes (apart from phase transitions) is always even. Such a type of quantized thermal conductance is generically expected in ballistic wires in the normal state, but the appearance of quantized thermal conductance in superconducting wires is an exceptional property of this topological phase and it is not accompanied by quantized electric conductance.

It turns out that (see Appendix E3)

$$\text{Pf} H_U^{sc}(k_z = 0, \pi) = \text{Pf} H_V^{sc}(k_z = 0, \pi). \quad (17)$$

This means that in the presence of inversion symmetry the nontrivial topological invariant $\nu_{sc} = 1$ always leads to a change of $\nu_I(k_z)$ between $k_z = 0$ and $k_z = \pi$. Thus, in the presence of inversion symmetry there cannot exist a fully gapped topologically nontrivial superconducting phase supporting Majorana end modes, but instead $\nu_{sc} = 1$ guarantees the existence of a topologically nontrivial phase supporting gapless Majorana bulk modes. To get localized zero-energy Majorana end modes it is necessary to break the inversion symmetry.

The inversion symmetry can be broken in SnTe nanowires by utilizing ferroelectricity or a structure inversion asymmetry [32–37]. For the results obtained in this paper the explicit mechanism of the inversion symmetry breaking is not important. Therefore, for simplicity we consider a Rashba coupling term

$$H_R(\mathbf{k}) = \boldsymbol{\lambda}_R \cdot \sin \mathbf{k} \times \boldsymbol{\sigma}. \quad (18)$$

The magnitude of the Rashba coupling λ_R can be considered as the inversion-symmetry breaking field. For $\lambda_R = 0$ the inversion symmetry is obeyed and only the gapless topological phase can be realized, whereas for $\lambda_R \neq 0$ the gapless Majorana bulk modes are not protected and the opening of an energy gap can transform the system into a fully gapped topologically nontrivial superconductor supporting localized Majorana end modes.

In Fig. 11 we illustrate the dependence of the topological phase diagrams on the nanowire thickness. For very small thicknesses there exists a large insulating gap at the charge neutrality point in the normal state spectrum (Fig. 3), and therefore the topologically nontrivial phase can be reached only by having either a reasonably large chemical potential μ or Zeeman field B_z. However, with increasing thickness of the nanowire the insulating gap decreases and the nontrivial
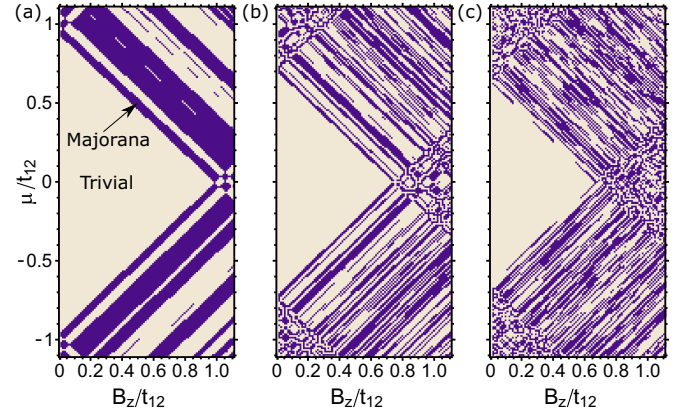

FIG. 11. Topological phase diagrams for SnTe nanowires in presence of induced superconductivity. The thicknesses of the nanowires are (a) 8, (b) 10, and (c) 18 atoms. The blue regions indicate parameter regimes where $\nu_{sc} = 1$. In the presence of inversion symmetry they correspond to a topological phase supporting gapless Majorana bulk modes. If the inversion symmetry is broken they correspond to fully gapped topological superconducting phase supporting Majorana end modes. In the numerical calculations we have used $\Delta = 0.01$ eV. The topological region always starts for $B_z > \Delta$ and the main effect of increasing (decreasing) Δ is to shift the nontrivial phases right (left) along B_z axis.

phases are distributed more uniformly in the parameter space. Similarly as in the case of the normal state phase diagram (Fig. 2), we expect that for realistic nanowire thicknesses the topologically nontrivial phase is accessible with experimentally feasible values of the chemical potential and Zeeman field. The structure of the topological phase diagram is quite complicated and it is not easy to extract simple conditions for the existence of the nontrivial phase. It is worth mentioning that the topological region always starts for $B_z > \Delta$ and the main effect of increasing (decreasing) Δ is to shift the nontrivial phases right (left) along B_z axis.

As discussed above, in the presence of inversion symmetry the $\nu_{sc} = 1$ regions in Fig. 11 correspond to the gapless topological phase. This is indeed the case as demonstrated with explicit calculation in Fig. 12(a). Moreover, if inversion-symmetry breaking field is introduced our numerical calculations confirm the opening of an energy gap in the bulk spectrum and the appearance of the zero-energy Majorana modes localized at the end of the superconducting nanowire [Figs. 12(b) and 12(c)].

As illustrated in Fig. 11 the topological phase becomes fragmented into smaller and smaller regions in the parameter space upon increasing the wire thickness. Therefore, one might be concerned about the experimental feasibility to observe the topological superconductivity in these systems. The systematic analysis of the dependence of the topological gap on the wire thickness goes beyond the scope of this paper, but in Fig. 13 we have focused on one of the fragmented topological regions in the case of 18 atoms thick nanowires. Our results show that also in this case it is possible to achieve a topological gap on the order of 1 K and to realize Majorana zero modes at the end of the wire by breaking the inversion symmetry. Therefore, at least in 18 atoms thick nanowires the
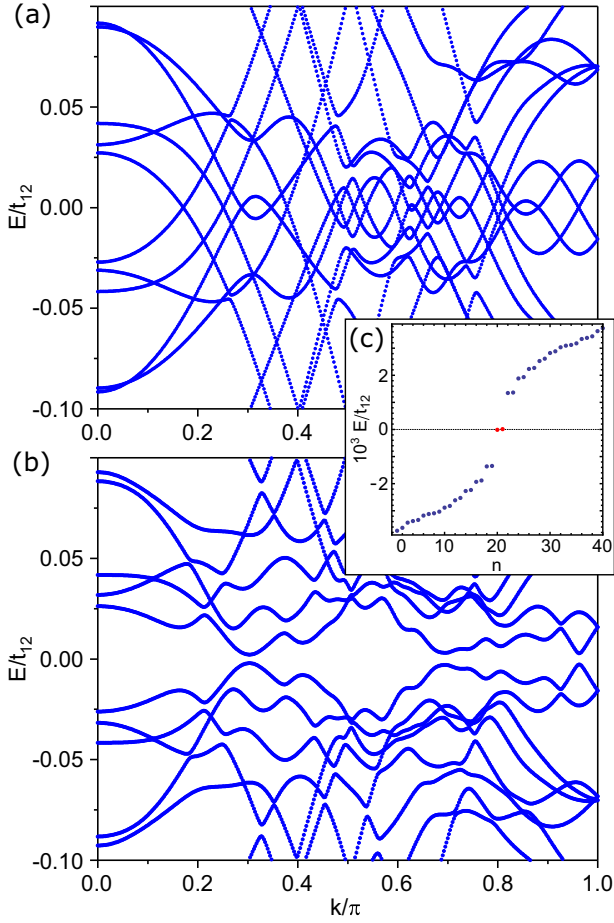
FIG. 12. Band structures for eight-atoms-thick superconducting nanowires (a) in the presence of inversion symmetry $\lambda_R = 0$ and (b) in the absence of inversion symmetry $\lambda_R = (0, 0.05, 0)$ eV. (c) The spectrum for 400-atoms-long superconducting nanowire, for $\lambda_R = (0, 0.05, 0)$ eV, demonstrating the existence of zero-energy Majorana modes localized at the end of the wire (red dots). For illustration purposes, we have computed the spectra for very thin nanowires with $B_z = 0.16$ eV, $\mu = 0.91$ eV and $\Delta = 0.1$ eV. However, due to the general arguments presented in the text, qualitatively similar results are expected also for experimentally feasible values of B_z, μ and Δ in thicker nanowires.

observation of the Majorana zero modes is still experimentally feasible.

VI. DISCUSSION AND CONCLUSIONS

We have shown that SnTe materials support robust corner states and hinge states in the normal state. The topological nature of these states is related to the approximate symmetries of the SnTe nanowires. Some of the approximations, such as the introduction of anisotropic spin-orbit coupling, are quite abstract technical tricks, but they are extremely useful because they allow us to construct well-defined topological invariants. Moreover, we have checked that our approximations are well-controlled and our results are applicable for realistic multivalley nanowires. We have also shown that the higher-order topological invariant, describing the existence of hinge states, is not directly related to the topological crystalline insulator
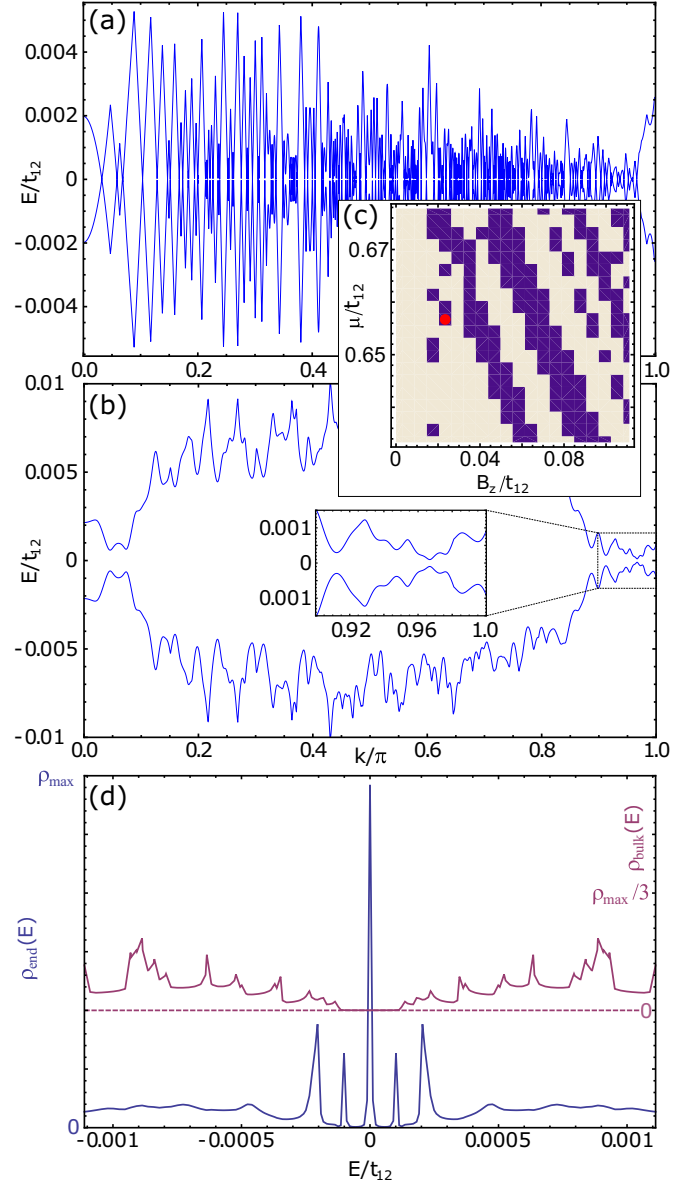
FIG. 13. Low-energy band structures for eighteen-atoms-thick superconducting nanowires (a) in the presence of inversion symmetry $\lambda_R = 0$ and (b) in the absence of inversion symmetry $\lambda_R = (0.02, 0.03, 0)$ eV. (c) Zoom into the relevant regime of the phase diagram. We have chosen $B_z = 0.02$ eV, $\mu = 0.5913$ eV and $\Delta = 0.01$ eV (indicated by the red dot in the phase diagram). (d) Local density of states in the bulk $\rho_{bulk}(E)$ and at the end $\rho_{end}(E)$ (normalized with the maximum value ρ_{max}) of the wire calculated using the Green's function method described in Ref. [58].

invariant. Therefore, the nontrivial crystalline insulator and higher-order topologies can appear either separately or together. If they appear together the surface states appearing due to topological crystalline insulator phase can coexist with the hinge states appearing due to higher-order topological phase. The higher-order topological invariant is a 2D invariant related to a high-symmetry plane in the momentum space. This plane corresponds to a fixed value of k_z and we have found that both the 2D bulk and the 1D edge are gapped within this plane, so that only the corner states appear. From the practical

point of view this means that the surface states arising from the topological crystalline insulator phase and the hinge states arising from the higher-order topological phase are separated in the momentum k_z so that they can coexist in ballistic wires where k_z is a good quantum number.

We have concentrated on relatively thin nanowires. Since the wave functions of the transverse modes transform as a function of the momentum k_z and energy from hinge states to surface states and bulk states, the transverse mode energies do not obey simple parametric dependencies as a function of the nanowire thickness and the Zeeman field. This means that the SnTe nanowires cannot be described by using a low-energy effective $k \cdot p$ theory. This is illustrated in the complicated phase diagram of nanowires, which we have discovered. Nevertheless, from the general trends in the thickness dependence we can extrapolate that for realistic nanowire thicknesses the topologically nontrivial phases can be reached with experimentally feasible values of the Zeeman field.

Finally, we have found that the superconducting SnTe nanowires support gapless bulk Majorana modes in the presence of inversion symmetry, and by introducing inversion-symmetry-breaking field, the bulk Majorana modes become gapped and topologically protected localized Majorana zero modes appear at the ends of the wire. This finding opens up new possibilities to control and create Majorana zero modes by controlling the inversion-symmetry breaking fields.

There exists various possibilities to experimentally probe the corner states, hinge states, and Majorana modes. High-quality transport studies are definitely the best way to study these systems. Ideally, the SnTe bulk materials would be insulators where the Fermi level is inside the insulating gap. The interesting physics, including the topological surface states, hinge states, and corner states all appear in this range of energies in the nanowires. Unfortunately, in reality the SnTe bulk materials typically have a large residual carrier density due to defects, which poses a significant obstacle for the studies of topological transport effects. Therefore it is of crucial importance to improve the control of the carrier density in SnTe materials. In comparison to the bulk systems the nanowires have the advantage that the carrier density can be more efficiently controlled with gate voltages. Tunneling measurements are possible also in the presence of a large carrier density because one can probe the local density of states as a function of energy by voltage-biasing the tip. One may also try to observe the hinge states and corner states using nano-angle-resolved photoemission spectroscopy but obtaining simultaneously both high-spatial and high-energy resolution is a difficult experimental challenge. The topologically protected gapless Majorana bulk modes could be probed via thermal conductance measurements, and they may also be detectable by measuring electrical shot-noise power or magnetoconductance oscillations in a ring geometry [59]. The Majorana zero modes give rise to various effects, such as a robust zero-bias peak in the conductance [60] and 4π Josephson effect [52,61], but the ultimate goal in the physics of Majorana zero modes is of course to observe effects directly related to the non-Abelian Majorana statistics [45–47]. The Majorana zero modes can be realized even if a significant

residual carrier density is present as illustrated in our phase diagrams. However, the new experimental challenge in this case is that the topologically nontrivial phase becomes more and more fragmented in thick wires.

APPENDIX A: CONSTRUCTION OF THE NANOWIRE HAMILTONIAN AND THE SYMMETRY OPERATIONS

In this section we give explicit expressions for the different symmetry operators of the nanowire Hamiltonian. Our starting point is the bulk Hamiltonian (1). The nearest-neighbor hopping matrices are

$$h_x(k_x) = \begin{pmatrix} 0 & 0 & 0 & 0 & \gamma_{k_x}^- & 0 & 0 & 0 \\ 0 & 0 & 0 & 0 & 0 & \gamma_{k_x}^+ & 0 & 0 \\ 0 & 0 & 0 & 0 & 0 & 0 & \gamma_{k_x}^- & 0 \\ 0 & 0 & 0 & 0 & 0 & 0 & 0 & \gamma_{k_x}^+ \\ \gamma_{k_x}^+ & 0 & 0 & 0 & 0 & 0 & 0 & 0 \\ 0 & \gamma_{k_x}^- & 0 & 0 & 0 & 0 & 0 & 0 \\ 0 & 0 & \gamma_{k_x}^+ & 0 & 0 & 0 & 0 & 0 \\ 0 & 0 & 0 & \gamma_{k_x}^- & 0 & 0 & 0 & 0 \end{pmatrix},$$

(A1)

$$h_y(k_y) = \begin{pmatrix} 0 & 0 & 0 & 0 & 0 & \gamma_{k_y}^- & 0 & 0 \\ 0 & 0 & 0 & 0 & \gamma_{k_y}^+ & 0 & 0 & 0 \\ 0 & 0 & 0 & 0 & 0 & 0 & 0 & \gamma_{k_y}^+ \\ 0 & 0 & 0 & 0 & 0 & 0 & \gamma_{k_y}^- & 0 \\ 0 & \gamma_{k_y}^- & 0 & 0 & 0 & 0 & 0 & 0 \\ \gamma_{k_y}^+ & 0 & 0 & 0 & 0 & 0 & 0 & 0 \\ 0 & 0 & 0 & \gamma_{k_y}^+ & 0 & 0 & 0 & 0 \\ 0 & 0 & \gamma_{k_y}^- & 0 & 0 & 0 & 0 & 0 \end{pmatrix},$$

(A2)

and

$$h_z(k_z) = \begin{pmatrix} 0 & 0 & 0 & 0 & 0 & 0 & 0 & \gamma_{k_z}^+ \\ 0 & 0 & 0 & 0 & 0 & 0 & \gamma_{k_z}^+ & 0 \\ 0 & 0 & 0 & 0 & 0 & \gamma_{k_z}^- & 0 & 0 \\ 0 & 0 & 0 & 0 & \gamma_{k_z}^- & 0 & 0 & 0 \\ 0 & 0 & 0 & \gamma_{k_z}^+ & 0 & 0 & 0 & 0 \\ 0 & 0 & \gamma_{k_z}^+ & 0 & 0 & 0 & 0 & 0 \\ 0 & \gamma_{k_z}^- & 0 & 0 & 0 & 0 & 0 & 0 \\ \gamma_{k_z}^- & 0 & 0 & 0 & 0 & 0 & 0 & 0 \end{pmatrix},$$

(A3)

where $\gamma_{k_\alpha}^+ = 1 + e^{ik_\alpha}$ and $\gamma_{k_\alpha}^- = 1 + e^{-ik_\alpha}$. The next-nearest-neighbor hopping matrices are

$h_{xy}(k_x, k_y)$

$$
= \begin{pmatrix}
0 & \phi_{-x,-y} & 0 & 0 & 0 & 0 & 0 & 0 \\
\phi_{x,y} & 0 & 0 & 0 & 0 & 0 & 0 & 0 \\
0 & 0 & 0 & \theta_{-x,y} & 0 & 0 & 0 & 0 \\
0 & 0 & \theta_{x,-y} & 0 & 0 & 0 & 0 & 0 \\
0 & 0 & 0 & 0 & 0 & \theta_{x,-y} & 0 & 0 \\
0 & 0 & 0 & 0 & \theta_{-x,y} & 0 & 0 & 0 \\
0 & 0 & 0 & 0 & 0 & 0 & 0 & \phi_{x,y} \\
0 & 0 & 0 & 0 & 0 & 0 & \phi_{-x,-y} & 0
\end{pmatrix},
$$

(A4)

$h_{yx}(k_x, k_y)$

$$
= \begin{pmatrix}
0 & \theta_{-x,-y} & 0 & 0 & 0 & 0 & 0 & 0 \\
\theta_{x,y} & 0 & 0 & 0 & 0 & 0 & 0 & 0 \\
0 & 0 & 0 & \phi_{-x,y} & 0 & 0 & 0 & 0 \\
0 & 0 & \phi_{x,-y} & 0 & 0 & 0 & 0 & 0 \\
0 & 0 & 0 & 0 & 0 & \phi_{-x,-y} & 0 & 0 \\
0 & 0 & 0 & 0 & \phi_{-x,y} & 0 & 0 & 0 \\
0 & 0 & 0 & 0 & 0 & 0 & 0 & \theta_{x,y} \\
0 & 0 & 0 & 0 & 0 & 0 & \theta_{-x,-y} & 0
\end{pmatrix},
$$

(A5)

$h_{yz}(k_y, k_z)$

$$
= \begin{pmatrix}
0 & 0 & \theta_{-y,z} & 0 & 0 & 0 & 0 & 0 \\
0 & 0 & 0 & \phi_{y,z} & 0 & 0 & 0 & 0 \\
\theta_{y,-z} & 0 & 0 & 0 & 0 & 0 & 0 & 0 \\
0 & \phi_{-y,-z} & 0 & 0 & 0 & 0 & 0 & 0 \\
0 & 0 & 0 & 0 & 0 & 0 & \theta_{-y,z} & 0 \\
0 & 0 & 0 & 0 & 0 & 0 & 0 & \phi_{y,z} \\
0 & 0 & 0 & 0 & \theta_{y,-z} & 0 & 0 & 0 \\
0 & 0 & 0 & 0 & 0 & \phi_{-y,-z} & 0 & 0
\end{pmatrix},
$$

(A6)

$h_{zy}(k_y, k_z)$

$$
= \begin{pmatrix}
0 & 0 & \phi_{-y,z} & 0 & 0 & 0 & 0 & 0 \\
0 & 0 & 0 & \theta_{y,z} & 0 & 0 & 0 & 0 \\
\phi_{y,-z} & 0 & 0 & 0 & 0 & 0 & 0 & 0 \\
0 & \theta_{-y,-z} & 0 & 0 & 0 & 0 & 0 & 0 \\
0 & 0 & 0 & 0 & 0 & 0 & \phi_{-y,z} & 0 \\
0 & 0 & 0 & 0 & 0 & 0 & 0 & \theta_{y,z} \\
0 & 0 & 0 & 0 & \phi_{y,-z} & 0 & 0 & 0 \\
0 & 0 & 0 & 0 & 0 & \theta_{-y,-z} & 0 & 0
\end{pmatrix},
$$

(A7)

$h_{zx}(k_x, k_z)$

$$
= \begin{pmatrix}
0 & 0 & 0 & \theta_{-x,z} & 0 & 0 & 0 & 0 \\
0 & 0 & \phi_{x,z} & 0 & 0 & 0 & 0 & 0 \\
0 & \phi_{-x,-z} & 0 & 0 & 0 & 0 & 0 & 0 \\
\theta_{x,-z} & 0 & 0 & 0 & 0 & 0 & 0 & 0 \\
0 & 0 & 0 & 0 & 0 & 0 & 0 & \phi_{x,z} \\
0 & 0 & 0 & 0 & 0 & 0 & \theta_{-x,z} & 0 \\
0 & 0 & 0 & 0 & 0 & \theta_{x,-z} & 0 & 0 \\
0 & 0 & 0 & 0 & \phi_{-x,-z} & 0 & 0 & 0
\end{pmatrix},
$$

(A8)

and

$h_{xz}(k_x, k_z)$

$$
= \begin{pmatrix}
0 & 0 & 0 & \phi_{-x,z} & 0 & 0 & 0 & 0 \\
0 & 0 & \theta_{x,z} & 0 & 0 & 0 & 0 & 0 \\
0 & \theta_{-x,-z} & 0 & 0 & 0 & 0 & 0 & 0 \\
\phi_{x,-z} & 0 & 0 & 0 & 0 & 0 & 0 & 0 \\
0 & 0 & 0 & 0 & 0 & 0 & 0 & \theta_{x,z} \\
0 & 0 & 0 & 0 & 0 & 0 & \phi_{-x,z} & 0 \\
0 & 0 & 0 & 0 & 0 & \phi_{x,-z} & 0 & 0 \\
0 & 0 & 0 & 0 & \theta_{-x,-z} & 0 & 0 & 0
\end{pmatrix},
$$

(A9)

where $\theta_{\pm\alpha,\pm\beta} = e^{\pm ik_\alpha} + e^{\pm ik_\beta}$ and $\phi_{\pm\alpha,\pm\beta} = 1 + e^{i(\pm k_\alpha \pm k_\beta)}$.

To obtain the lower dimensional Hamiltonians, we can first expand the Hamiltonian as

$$
\mathcal{H}(\mathbf{k}) = H_0(k_y, k_z) + e^{-ik_x} H_1(k_y, k_z) + e^{ik_x} H_1^\dagger(k_y, k_z).
$$

Then the 2D Hamiltonian obtained by assuming a finite thickness N_x in the x direction is given by a $48N_x \times 48N_x$ matrix

$$
\mathcal{H}^{2D}(k_y, k_z) = \begin{pmatrix}
H_0 & H_1^\dagger & 0 & 0 & 0 & \cdots & 0 \\
H_1 & H_0 & H_1^\dagger & 0 & 0 & \cdots & 0 \\
0 & H_1 & H_0 & H_1^\dagger & 0 & \cdots & 0 \\
\vdots & & & \ddots & & & \vdots \\
\vdots & & & & \ddots & & \vdots \\
0 & \cdots & \cdots & 0 & 0 & H_0 & H_1^\dagger \\
0 & \cdots & \cdots & 0 & 0 & H_1 & H_0
\end{pmatrix}.
$$

(A10)

Similarly, we can decompose this 2D Hamiltonian as

$$
\mathcal{H}^{2D}(k_y, k_z) = H_0'(k_z) + e^{-ik_y} H_1'(k_z) + e^{ik_y} H_1'^\dagger(k_z), \quad \text{(A11)}
$$

where $H_{0(1)}'$ are $48N_x \times 48N_x$ matrices. The Hamiltonian for the nanowire with a finite thickness N_x (N_y) in x (y) direction is given by $48N_x N_y \times 48N_x N_y$ matrix

$$
\mathcal{H}^{1D}(k_z) = \begin{pmatrix}
H_0' & H_1'^\dagger & 0 & 0 & 0 & \cdots & 0 \\
H_1' & H_0' & H_1'^\dagger & 0 & 0 & \cdots & 0 \\
0 & H_1' & H_0' & H_1'^\dagger & 0 & \cdots & 0 \\
\vdots & & & \ddots & & & \vdots \\
\vdots & & & & \ddots & & \vdots \\
0 & \cdots & \cdots & 0 & 0 & H_0' & H_1'^\dagger \\
0 & \cdots & \cdots & 0 & 0 & H_1' & H_0'
\end{pmatrix}.
$$

(A12)

Assuming that $N_x = N_y$, the nanowire has a screw-axis symmetry, which is described by an operator

$$
S_c(k_z) = P_z \otimes \exp\left(-i\frac{\pi}{4}\sigma_z\right) \otimes \exp\left(-i\frac{\pi}{2}L_z\right) \otimes s_c(k_z).
$$

(A13)

Here P_z is a $N_x N_y \times N_x N_y$ matrix that realizes the fourfold rotation of the unit cells. For general $N_x = N_y$ we have P_z such that $(P_z)_{i,j} = 1$ for $i = q + (p-1)N_x$ and $j = p + (N_x - q)N_x$ $(p, q = 1, \ldots, N_x)$ and $(P_z)_{i,j} = 0$

otherwise. $s_c(k_z)$ is the 8×8 matrix acting inside the unit cell

$$s_c(k_z) = \begin{pmatrix} 0 & 0 & 1 & 0 & 0 & 0 & 0 & 0 \\ 0 & 0 & 0 & 1 & 0 & 0 & 0 & 0 \\ 0 & e^{-ik_z} & 0 & 0 & 0 & 0 & 0 & 0 \\ e^{-ik_z} & 0 & 0 & 0 & 0 & 0 & 0 & 0 \\ 0 & 0 & 0 & 0 & 0 & 0 & 0 & 1 \\ 0 & 0 & 0 & 0 & 0 & 0 & 1 & 0 \\ 0 & 0 & 0 & 0 & e^{-ik_z} & 0 & 0 & 0 \\ 0 & 0 & 0 & 0 & 0 & e^{-ik_z} & 0 & 0 \end{pmatrix}.$$

(A14)

The mirror symmetry operators corresponding to the mirror planes perpendicular to x, y and z are

$$M_x(k_z) = \mathbb{1}_{N_y} \otimes m_x \otimes \sigma_x \otimes (2L_x^2 - \mathbb{1}_3) \otimes g(-k_z)\mathcal{P}_z\mathcal{P}_x,$$

$$M_y(k_z) = m_y \otimes \mathbb{1}_{N_x} \otimes \sigma_y \otimes (2L_y^2 - \mathbb{1}_3) \otimes g(-k_z)\mathcal{P}_z\mathcal{P}_y,$$

$$M_z(k_z) = \mathbb{1}_{N_y} \otimes \mathbb{1}_{N_x} \otimes \sigma_z \otimes (2L_z^2 - \mathbb{1}_3) \otimes g(k_z), \quad \text{(A15)}$$

where $g(k_z) = \text{diag}(e^{-ik_z}, e^{-ik_z}, 1, 1, e^{-ik_z}, e^{-ik_z}, 1, 1)$,

$$\mathcal{P}_x = \begin{pmatrix} 0 & 0 & 0 & 0 & 1 & 0 & 0 & 0 \\ 0 & 0 & 0 & 0 & 0 & 1 & 0 & 0 \\ 0 & 0 & 0 & 0 & 0 & 0 & 1 & 0 \\ 0 & 0 & 0 & 0 & 0 & 0 & 0 & 1 \\ 1 & 0 & 0 & 0 & 0 & 0 & 0 & 0 \\ 0 & 1 & 0 & 0 & 0 & 0 & 0 & 0 \\ 0 & 0 & 1 & 0 & 0 & 0 & 0 & 0 \\ 0 & 0 & 0 & 1 & 0 & 0 & 0 & 0 \end{pmatrix},$$

(A16)

$$\mathcal{P}_y = \begin{pmatrix} 0 & 0 & 0 & 0 & 0 & 1 & 0 & 0 \\ 0 & 0 & 0 & 0 & 1 & 0 & 0 & 0 \\ 0 & 0 & 0 & 0 & 0 & 0 & 0 & 1 \\ 0 & 0 & 0 & 0 & 0 & 0 & 1 & 0 \\ 0 & 1 & 0 & 0 & 0 & 0 & 0 & 0 \\ 1 & 0 & 0 & 0 & 0 & 0 & 0 & 0 \\ 0 & 0 & 0 & 1 & 0 & 0 & 0 & 0 \\ 0 & 0 & 1 & 0 & 0 & 0 & 0 & 0 \end{pmatrix},$$

(A17)

$$\mathcal{P}_z = \begin{pmatrix} 0 & 0 & 0 & 0 & 0 & 0 & 0 & 1 \\ 0 & 0 & 0 & 0 & 0 & 0 & 1 & 0 \\ 0 & 0 & 0 & 0 & 0 & 1 & 0 & 0 \\ 0 & 0 & 0 & 0 & 1 & 0 & 0 & 0 \\ 0 & 0 & 0 & 1 & 0 & 0 & 0 & 0 \\ 0 & 0 & 1 & 0 & 0 & 0 & 0 & 0 \\ 0 & 1 & 0 & 0 & 0 & 0 & 0 & 0 \\ 1 & 0 & 0 & 0 & 0 & 0 & 0 & 0 \end{pmatrix},$$

(A18)

and

$$m_x = m_y = \begin{pmatrix} 0 & \dots & 0 & 1 \\ \vdots & & 1 & 0 \\ \vdots & \ddots & & \vdots \\ 1 & \dots & 0 & 0 \end{pmatrix}.$$

(A19)

APPENDIX B: WEYL SEMIMETAL PHASE FOR $\lambda_z = 0$

Setting $\lambda_z = 0$ is a good approximation in thin nanowires. In this case, there exists a nonsymmorphic chiral symmetry $S_z(k_z)$ given by,

$$S_z(k_z) = \mathbb{1}_{N_y} \otimes \mathbb{1}_{N_x} \otimes \sigma_z \otimes \mathbb{1}_3 \otimes \Sigma\mathcal{P}_z g(k_z), \quad \text{(B1)}$$

and it is possible to combine it with $M_z(k_z)$ and time-reversal T to construct an antiunitary operator that anticommutes with $\mathcal{H}^{1D}(k_z)$ for any k_z. This operator squares to $+1$ and therefore it can give rise to a Pfaffian-protected Weyl semimetal phase
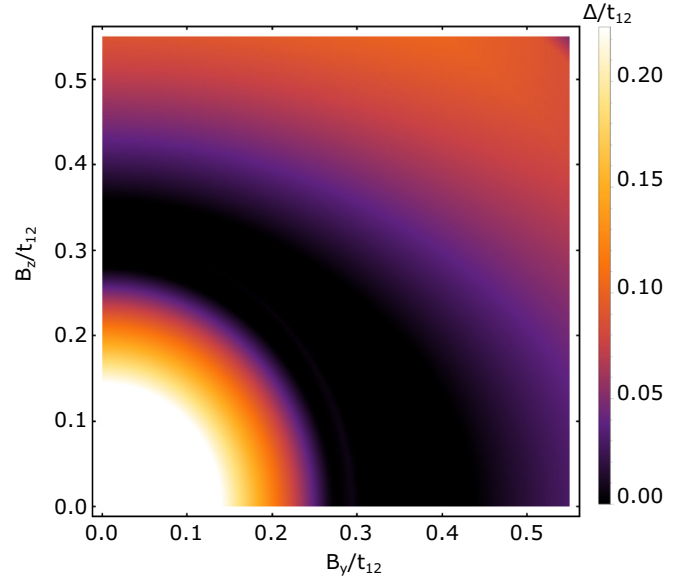
FIG. 14. The direct band gap Δ as function of B_y and B_z for 4 atoms thick nanowire and $\lambda_z = 0$. In the black region $\Delta = 0$ and the system is in a 1D Weyl semimetal phase.

also when the Zeeman field is not along the z axis. Figure 14 shows that there exists a Weyl semimetal phase for a range of Zeeman field magnitudes for all Zeeman field directions in the yz plane.

APPENDIX C: EFFECTS OF ANISOTROPIC SPIN-ORBIT COUPLING

We can study the effects of breaking spatial symmetries by considering anisotropic spin-orbit couplings. In Fig. 15(a) we show the phase diagram of eight atoms thick nanowire as function of λ_z and B_z for $\lambda_x = \lambda_y = \lambda$. In this case the system still obeys the screw-axis symmetry so that the phase diagram contains the Weyl semimetal phase in addition to the insulator
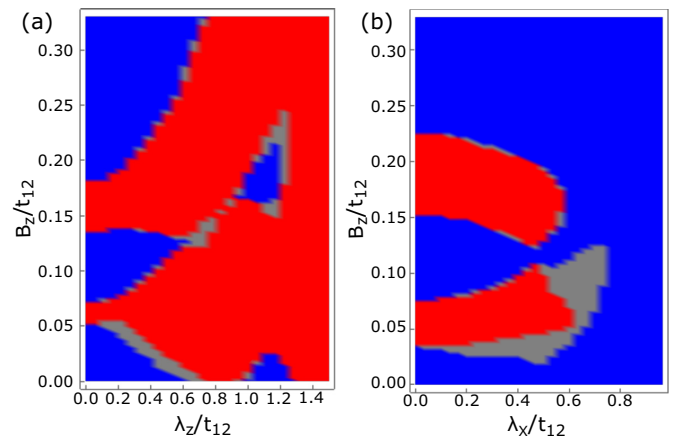
FIG. 15. Phase diagram as function of (a) λ_z and B_z for $\lambda_x = \lambda_y = \lambda$ and (b) λ_x and B_z for $\lambda_y = \lambda_z = \lambda$. The different phases are: insulator phase (blue), Weyl semimetal phase (red) and indirect semimetal phase (grey). The thickness of the nanowire is eight atoms.

and indirect semimetal phases. The phase boundaries depend on λ_z.

On the other hand, the screw-axis symmetry is broken if $\lambda_x \neq \lambda_y = \lambda_z$. Nevertheless, the system still obeys a twofold rotational symmetry, which can protect the existence of Weyl points. Indeed, the phase diagram as a function of λ_x and B_z for $\lambda_y = \lambda_z = \lambda$ also contains the Weyl semimetal phase as shown in Fig. 15(b).

## APPENDIX D: HIGHER-ORDER TOPOLOGICAL INVARIANT

1. Hamiltonian and symmetries in the $k_3 = \pi$ plane

In this section we consider the Hamiltonian for a system with atoms at positions $(0, 0, \pm 1/2)$ and translation vectors $a_1 = (1, 0, 1)$, $a_2 = (0, 1, 1)$ and $(0, 0, 2)$. For this unit cell the hopping matrices in the bulk Hamiltonian $\mathcal{H}(\mathbf{k})$ of Eq. (1) are

$$h_x(\mathbf{k}) = \begin{pmatrix} 0 & e^{ik_1} + e^{i(k_3-k_1)} \\ e^{-ik_1} + e^{i(k_1-k_3)} & 0 \end{pmatrix}, \quad \text{(D1)}$$

$$h_y(\mathbf{k}) = \begin{pmatrix} 0 & e^{ik_2} + e^{i(k_3-k_2)} \\ e^{-ik_2} + e^{i(k_2-k_3)} & 0 \end{pmatrix}, \quad \text{(D2)}$$

$$h_z(\mathbf{k}) = \begin{pmatrix} 0 & 1 + e^{ik_3} \\ 1 + e^{-ik_3} & 0 \end{pmatrix}, \quad \text{(D3)}$$

and

$$h_{xy}(\mathbf{k}) = 2\cos(k_1 + k_2 - k_3)\mathbb{1}_2,$$
$$h_{yx}(\mathbf{k}) = 2\cos(k_1 - k_2)\mathbb{1}_2,$$
$$h_{xz}(\mathbf{k}) = 2\cos(k_1)\mathbb{1}_2,$$
$$h_{zx}(\mathbf{k}) = 2\cos(k_1 - k_3)\mathbb{1}_2,$$
$$h_{yz}(\mathbf{k}) = 2\cos(k_2)\mathbb{1}_2,$$
$$h_{zy}(\mathbf{k}) = 2\cos(k_2 - k_3)\mathbb{1}_2, \quad \text{(D4)}$$

and the symmetries discussed above are

$$I = \mathbb{1}_2 \otimes \mathbb{1}_3 \otimes \exp\left(-i\frac{k_3}{2}\tau_z\right),$$

$$M_\alpha = \sigma_\alpha \otimes (2L_\alpha^2 - \mathbb{1}_3) \otimes \mathbb{1}_2, \quad \alpha = x, y,$$

$$M_z = \sigma_z \otimes (2L_z^2 - \mathbb{1}_3) \otimes \exp\left(-i\frac{k_3}{2}\tau_z\right),$$

$$M_{xy} = \frac{\sigma_x - \sigma_y}{\sqrt{2}} \otimes \left(2\left(\frac{L_x - L_y}{\sqrt{2}}\right)^2 - \mathbb{1}_3\right) \otimes \mathbb{1}_2.$$

Moreover, we also have a fourfold rotation

$$R_4 = \exp\left(i\frac{\pi}{2}\frac{1}{2}\sigma_z\right) \otimes \exp\left(i\frac{\pi}{2}L_z\right) \otimes \mathbb{1}_2,$$

and the time-reversal symmetry

$$T = \sigma_y \otimes \mathbb{1}_3 \otimes \mathbb{1}_2.$$

These symmetries act on the Hamiltonian as

$$I\mathcal{H}(k_1, k_2, k_3)I^\dagger = \mathcal{H}(-k_1, -k_2, -k_3),$$
$$M_x\mathcal{H}(k_1, k_2, k_3)M_x^\dagger = \mathcal{H}(k_3 - k_1, k_2, k_3),$$

$$M_y\mathcal{H}(k_1, k_2, k_3)M_y^\dagger = \mathcal{H}(k_1, k_3 - k_2, k_3),$$
$$M_z\mathcal{H}(k_1, k_2, k_3)M_z^\dagger = \mathcal{H}(k_1 - k_3, k_2 - k_3, -k_3),$$
$$M_{xy}\mathcal{H}(k_1, k_2, k_3)M_{xy}^\dagger = \mathcal{H}(k_2, k_1, k_3),$$
$$R_4\mathcal{H}(k_1, k_2, k_3)R_4^\dagger = \mathcal{H}(k_3 - k_2, k_1, k_3),$$
$$T\mathcal{H}(\mathbf{k})T^\dagger = \mathcal{H}(-\mathbf{k})^T. \quad \text{(D5)}$$

We concentrate on the $k_3 = \pi$ plane. In this case, the standard high-symmetry points are related as

$$M_x\mathcal{H}(0, 0, \pi)M_x^\dagger = \mathcal{H}(\pi, 0, \pi),$$
$$M_y\mathcal{H}(0, 0, \pi)M_y^\dagger = \mathcal{H}(0, \pi, \pi),$$
$$M_yM_x\mathcal{H}(0, 0, \pi)M_x^\dagger M_y^\dagger = \mathcal{H}(\pi, \pi, \pi). \quad \text{(D6)}$$

Moreover, the $k_3 = \pi$ plane has four special points $(k_1, k_2) = (\pi/2 + n_1\pi, \pi/2 + n_2\pi)$ $(n_{1,2} = 0, 1)$ obeying

$$\left[M_x, \mathcal{H}\left(\frac{\pi}{2} + n_1\pi, \frac{\pi}{2} + n_2\pi\right)\right] = 0,$$
$$\left[M_y, \mathcal{H}\left(\frac{\pi}{2} + n_1\pi, \frac{\pi}{2} + n_2\pi\right)\right] = 0. \quad \text{(D7)}$$

Among these points we find two fourfold rotation centers

$$\left[R_4, \mathcal{H}\left(\frac{\pi}{2}, \frac{\pi}{2}, \pi\right)\right] = \left[R_4, \mathcal{H}\left(\frac{3\pi}{2}, \frac{3\pi}{2}, \pi\right)\right] = 0, \quad \text{(D8)}$$

and two fourfold rotoinversion centers

$$\left[Q_4, \mathcal{H}\left(\frac{\pi}{2}, \frac{3\pi}{2}, \pi\right)\right] = \left[Q_4, \mathcal{H}\left(\frac{3\pi}{2}, \frac{\pi}{2}, \pi\right)\right] = 0, \quad \text{(D9)}$$

where

$$Q_4 = IR_4. \quad \text{(D10)}$$

The rotoinversion centers are mapped onto each other by the fourfold rotation or diagonal mirror

$$R_4\mathcal{H}\left(\frac{\pi}{2}, \frac{3\pi}{2}, \pi\right)R_4^\dagger = \mathcal{H}\left(\frac{3\pi}{2}, \frac{\pi}{2}, \pi\right),$$
$$M_{xy}\mathcal{H}\left(\frac{\pi}{2}, \frac{3\pi}{2}, \pi\right)M_{xy}^\dagger = \mathcal{H}\left(\frac{3\pi}{2}, \frac{\pi}{2}, \pi\right), \quad \text{(D11)}$$

and the rotation centers are related by the inversion symmetry

$$I\mathcal{H}\left(\frac{\pi}{2}, \frac{\pi}{2}, \pi\right)I^\dagger = \mathcal{H}\left(\frac{3\pi}{2}, \frac{3\pi}{2}, \pi\right). \quad \text{(D12)}$$

Finally, the product of M_x and M_y yields a twofold rotation R_2 with respect to the z axis

$$R_2 = iM_xM_y = \sigma_z \otimes (2L_z^2 - \mathbb{1}_3) \otimes \mathbb{1}_2, \quad \text{(D13)}$$

and the rotation and rotoinversion centers are also twofold rotation centers

$$\left[R_2, \mathcal{H}\left(\frac{\pi}{2} + n_1\pi, \frac{\pi}{2} + n_2\pi\right)\right] = 0, \quad n_{1,2} = 0, 1. \quad \text{(D14)}$$

2. Pfaffian at the high-symmetry points in the $k_3 = \pi$ plane with $\lambda_z = 0$ approximation

By assuming that $\lambda_z = 0$ and $\lambda_x = \lambda_y = \lambda$ we find that the Hamiltonian $\mathcal{H}(k_1, k_2, \pi)$ satisfies a chiral symmetry

$S_z \mathcal{H}(k_1, k_2, \pi) S_z^\dagger = -\mathcal{H}(k_1, k_2, \pi)$, where

$$S_z = \sigma_z \otimes \mathbb{1}_3 \otimes \tau_x. \qquad (D15)$$

Therefore, the symmetry class of $\mathcal{H}(k_1, k_2, \pi)$ is DIII so that we can find an eigenbasis of S_z in which the Hamiltonian takes the form of

$$\mathcal{H}(k_1, k_2, \pi) = \begin{pmatrix} 0 & u(k_1, k_2) \\ u^\dagger(k_1, k_2) & 0 \end{pmatrix}, \qquad (D16)$$

and the time-reversal symmetry operator is

$$T = \begin{pmatrix} 0 & -i\mathbb{1}_6 \\ i\mathbb{1}_6 & 0 \end{pmatrix}. \qquad (D17)$$

Thus, the Hamiltonian satisfies a particle-hole symmetry

$$C\mathcal{H}(k_1, k_2, \pi)C^\dagger = -\mathcal{H}(-k_1, -k_2, \pi)^T, \qquad (D18)$$

where

$$C = TS_z = \begin{pmatrix} 0 & \mathbb{1}_6 \\ \mathbb{1}_6 & 0 \end{pmatrix}, \qquad (D19)$$

so that

$$u(k_1, k_2) = -u(-k_1, -k_2)^T. \qquad (D20)$$

Therefore, at the high-symmetry points $\mathbf{K} = (n_1 \pi, n_2 \pi)$ $(n_{1,2} = 0, 1)$

$$u(\mathbf{K})^T = -u(\mathbf{K}), \qquad (D21)$$

and we can define a Pfaffian

$$p = \mathrm{Pf}\, u(\mathbf{K}). \qquad (D22)$$

Note that all high-symmetry points $\mathbf{K}$ are equivalent. The possible values of p are restricted because of the inversion symmetry operator, which can be written in the present basis as

$$I = \begin{pmatrix} 0 & o \\ o^T & 0 \end{pmatrix}, \qquad (D23)$$

where

$$o = \begin{pmatrix} 0 & \mathbb{1}_3 \\ -\mathbb{1}_3 & 0 \end{pmatrix} \qquad (D24)$$

is an orthogonal matrix. By applying it to the Hamiltonian at the $\mathbf{K}$ point we get

$$u(\mathbf{K}) = ou(\mathbf{K})^\dagger o = ou(\mathbf{K})^* o^T, \qquad (D25)$$

where we have used Eq. (D20) and $o^T = -o$. Using the general properties of the Pfaffian we get

$$p = \mathrm{Pf}\, u(\mathbf{K}) = \mathrm{Pf}[ou(\mathbf{K})^* o^T] = \det o\; \mathrm{Pf}\, u(\mathbf{K})^* = p^\star. \qquad (D26)$$

This means that p is a real number.

3. Determinant at the rotation points in the $k_3 = \pi$ plane with $\lambda_z = 0$ approximation

At the fourfold rotation and rotoinversion points we can use these symmetries to decompose the Hamiltonian into diagonal blocks. We first focus on the rotoinversion center $\mathbf{K}' =$

$(\pi/2, 3\pi/2, \pi)$ point. In the eigenbasis of Q_4 the Hamiltonian takes a block-diagonal form

$$\mathcal{H}(\mathbf{K}') = \begin{pmatrix} h_1 & 0 & 0 & 0 \\ 0 & h_2 & 0 & 0 \\ 0 & 0 & h_3 & 0 \\ 0 & 0 & 0 & h_4 \end{pmatrix}, \qquad (D27)$$

where $h_{1,\dots,4}$ are the 3×3 blocks. By ordering the eigenvalues of Q_4 in a suitable way, the chiral symmetry takes a block form

$$S_z = \begin{pmatrix} 0 & s_1 & 0 & 0 \\ s_2 & 0 & 0 & 0 \\ 0 & 0 & 0 & s_3 \\ 0 & 0 & s_4 & 0 \end{pmatrix}, \qquad (D28)$$

with s_i being 3×3 unitary block. This form follows from the fact that Q_4 and S_z anticommute. The spectrum of each individual block h_i is not symmetric around zero, but the spectrum of h_1 (h_3) is opposite to the spectrum of h_2 (h_4). Since the blocks also have an odd dimension, the determinants satisfy $\det h_1 = -\det h_2$ and $\det h_3 = -\det h_4$. The spectrum of the whole Hamiltonian $\mathcal{H}(\mathbf{K}')$ is twice degenerate because of the presence of the symmetry $\Pi = IT$ with the property $\Pi\Pi^\star = -1$ that gives Kramer denegeracy at every $\mathbf{k}$ point. This symmetry in the present basis takes a block form of

$$\Pi = IT = \begin{pmatrix} 0 & 0 & 0 & k_1 \\ 0 & 0 & k_2 & 0 \\ 0 & k_2^\dagger & 0 & 0 \\ k_1^\dagger & 0 & 0 & 0 \end{pmatrix}. \qquad (D29)$$

This implies that the blocks h_1 and h_4 (h_2 and h_3) have the same spectrum. From this it follows that

$$\det[\mathcal{H}(\mathbf{K}')] = d^4, \qquad (D30)$$

where $d \equiv \det h_1 = \det h_4 = -\det h_2 = -\det h_3$, and therefore d changes sign at the zero-energy gap closing occurring at the momentum $\mathbf{K}'$.

Finally, it is worth noticing that the above construction does not work for the fourfold rotation points. In the eigenbasis of R_4 the Hamiltonian consists of four diagonal blocks $h_{1,\dots,4}$, where $h_{1,2}$ ($h_{3,4}$) are 2×2 (4×4) matrices. The rotation R_4 commutes with S_z, so that in this basis

$$S_z = \begin{pmatrix} s_1 & 0 & 0 & 0 \\ 0 & s_2 & 0 & 0 \\ 0 & 0 & s_3 & 0 \\ 0 & 0 & 0 & s_4 \end{pmatrix}. \qquad (D31)$$

From this structure it follows that $\{h_i, s_i\} = 0$ so that spectrum of each block h_i is symmetric around zero. Thus, the determinants always satisfy $\det h_{1,2} \leqslant 0$ and $\det h_{3,4} \geqslant 0$, and therefore they cannot change sign in a gap closing.

APPENDIX E: TOPOLOGICAL INVARIANTS IN THE PRESENCE OF SUPERCONDUCTIVITY

1. Topological invariant of 1D superconductors belonging to class D

In the presence of induced superconductivity the BdG Hamiltonian $H^{sc}(k_z)$ always satisfies a particle-hole symmetry $C^{sc}(H^{sc}(-k_z))^T C^{sc} = -H^{sc}(k_z)$, where C^{sc} can be written in

the Nambu space as

$$C^{sc} = \begin{pmatrix} 0 & \mathbb{1} \\ \mathbb{1} & 0 \end{pmatrix}. \tag{E1}$$

We can utilize C^{sc} to perform a unitary transformation on the Hamiltonian

$$H_U^{sc}(k_z) = U^\dagger H^{sc}(k_z) U, \; U = \beta \sqrt{\Lambda_C}^{-1}, \tag{E2}$$

where the columns of matrix β are the eigenvectors of C^{sc} and Λ_C is a diagonal matrix containing the eigenvalues of C^{sc}, so that

$$C^{sc}\beta = \beta \Lambda_C. \tag{E3}$$

Because $C^{sc}C^{sc*} = 1$, which follows from the D symmetry class, and C^{sc} is unitary we can choose the eigenvectors so that they satisfy $\beta = \beta^*$. From this it follows that at $k_0 = 0, \pi$

$$\begin{aligned} \left(H_U^{sc}(k_0)\right)^T &= \sqrt{\Lambda_C}^{-1} \beta^T (H^{sc}(k_0))^T \beta \sqrt{\Lambda_C} \\ &= \sqrt{\Lambda_C} \beta^T C^{sc}(H^{sc}(k_0))^T C^{sc} \beta \sqrt{\Lambda_C}^{-1} \\ &= -\sqrt{\Lambda_C} \beta^T H^{sc}(k_0) \beta \sqrt{\Lambda_C}^{-1} = -H_U^{sc}(k_0), \end{aligned} \tag{E4}$$

and the particle-hole operator in the new basis becomes identity matrix

$$U^T C^{sc} U = \sqrt{\Lambda_C}^{-1} \beta^T C^{sc} \beta \sqrt{\Lambda_C}^{-1} = 1. \tag{E5}$$

Since the Hamiltonian is antisymmetric at $k_0 = 0, \pi$ we can define a Pfaffian, which is real because

$$\left[\text{Pf} H_U^{sc}(k_0)\right]^* = \text{Pf} H_U^{sc}(k_0)^T = \text{Pf}\left[H_U^{sc}(k_0)\right]. \tag{E6}$$

Therefore we can define a $\mathbb{Z}_2$ topological invariant as

$$\nu_{sc} = \left(1 - \text{sgn}\left[\text{Pf} H_U^{sc}(0) \text{Pf} H_U^{sc}(\pi)\right]\right)/2. \tag{E7}$$

This is the strong topological invariant of 1D superconductors belonging to the class D.

2. Topological invariant for inversion-symmetry protected gapless Majorana bulk modes

We can also combine C^{sc} with the inversion symmetry $I^{sc}(k_z)$ to produce an operator

$$A^{sc}(k_z) = C^{sc} I^{sc}(k_z), \tag{E8}$$

whose action on the Hamiltonian is

$$A_{k_z}^{sc\dagger}(H^{sc}(k_z))^T A_{k_z}^{sc} = -H^{sc}(k_z). \tag{E9}$$

From the double application of the above equation it follows that $A^{sc} A^{sc*} = \pm 1$, where $+1$ and -1 define different symmetry classes, in analogy to the particle hole symmetry. In our case we get $A^{sc} A^{sc*} = +1$, following from the D symmetry class $[C^{sc}, I^{sc}] = 0$ and $I^{sc} I^{sc*} = 1$.

Note that it is enough to know that A^{sc} is unitary and $A^{sc} A^{sc*} = +1$ to prove that it can be diagonalized by an orthogonal transformation. From unitarity we have $A^{sc} = \exp(iB)$ with B being Hermitian. From the latter property we get $\exp(-iB) = \exp(-iB^T)$, which gives $B^T = B + 2n\pi$. By taking the trace of this equation we get that $n = 0$ so B must be real symmetric. Then A^{sc} can be diagonalized by by an

orthogonal transformation. Then we find the real eigenbasis $\gamma(k_z)$ of $A^{sc}(k_z)$, we have

$$A^{sc}(k_z)\gamma(k_z) = \gamma(k_z)\Lambda_A(k_z). \tag{E10}$$

We define a unitary transformation

$$V(k_z) = \gamma(k_z)\sqrt{\Lambda_A(k_z)}^{-1}, \tag{E11}$$

and following the same derivation as in Eq. (E4) we can prove that the transformed Hamiltonian

$$H_V^{sc}(k_z) = V(k_z)^\dagger H^{sc}(k_z) V(k_z), \tag{E12}$$

is antisymmetric for any k_z. By utilizing the fact that the Pfaffian of the Hamiltonian is real valued, we can now define an inversion-symmetry protected $\mathbb{Z}_2$ topological invariant for all values of k_z as

$$\nu_I(k_z) = \left(1 - \text{sgn}\left[\text{Pf} H_V^{sc}(k_z)\right]\right)/2. \tag{E13}$$

If this invariant changes as a function of k_z there must necessarily be a gap closing. Therefore, there exists a 1D topological phase supporting inversion-symmetry protected gapless bulk Majorana modes. In the presence of inversion symmetry these gapless Majorana bulk modes can only be destroyed by merging them in a pairwise manner.

3. Relationship between the two Pfaffians

We have two antisymmetric forms of Hamiltonian. $H_U^{sc}(k_z)$ is antisymmetric at $k_z = 0, \pi$ and $H_V^{sc}(k_z)$ is antisymmetric for all values of k_z. These antisymmetric Hamiltonians allow us to define topological invariants with the help of their Pfaffians, and thus it is important to know how these Pfaffians are related to each other. Assume we have two antisymmetric Hamiltonians H' and H related by a change of basis as $H' = Q^\dagger H Q$. Then from antisymmetry of H' and H we have that $[H, QQ^T] = 0$. Then we have two options, either $QQ^T = 1$ and then $\text{Pf} H' = \det Q \text{Pf} H$ or QQ^T is equal to a symmetry operator of H and then the Pfaffians of H and H' do not have to be proportional. The latter case could lead to two independent invariants.

Coming back to our case, we find that

$$V(k_z = 0, \pi)V(k_z = 0, \pi)^T \neq 1, \tag{E14}$$

and this operator is indeed related to the inversion symmetry

$$V(k_z = 0, \pi)V(k_z = 0, \pi)^T = I^{sc}(k_z = 0, \pi), \tag{E15}$$

but it turns out that also a stronger property holds, namely

$$(V(k_z)V(k_z)^T)^\star = I^{sc}(k_z). \tag{E16}$$

From the last equation we obtain

$$V(k_z)^\dagger = V(k_z)^T I^{sc}(k_z). \tag{E17}$$

Consequently,

$$H_V^{sc}(k_z) = V(k_z)^T I^{sc}(k_z) H_U^{sc}(k_z) V(k_z). \tag{E18}$$

Thus the Pfaffians can be related as

$$\text{Pf} H_V^{sc}(k_z) = \det V(k_z) \text{Pf}\left[I^{sc}(k_z) H_U^{sc}(k_z)\right]. \tag{E19}$$

Both sides of the equations are well defined because $H_V^{sc}(k_z)$ is antisymmetric for any k_z and $I^{sc}(k_z) H_U^{sc}(k_z)$ is also antisymmetric for any k_z despite $H_U^{sc}(k_z)$ alone being symmetric

only at high-symmetry points. For the right-hand side we get $\det V(k_z) = \exp[24iN_xN_yk_z]$ so we always have $\det V(0) = \det V(\pi) = 1$. To calculate the Pfaffian on the right-hand side

at $k_0 = 0, \pi$ we can utilize the operator $\gamma(k_0) = \gamma(k_0)^*$, satisfying $\det \gamma(k_0) = 1$ and $\gamma(k_0)^T I^{sc}(k_0) \gamma(k_0)$ is a diagonal matrix, to obtain

$$\mathrm{Pf} H_V^{sc}(k_0) = \mathrm{Pf}\left[\gamma(k_0)^T I^{sc}(k_0)\gamma(k_0)\gamma(k_0)^T H_U^{sc}(k_0)\gamma(k_0)\right] = \mathrm{Pf}\left[-\gamma_-(k_0)^T H_U^{sc}(k_0)\gamma_-(k_0)\right]\mathrm{Pf}\left[\gamma_+(k_0)^T H_U^{sc}(k_0)\gamma_+(k_0)\right]$$
$$= (-1)^{d_-/2}\mathrm{Pf}\left[\gamma_-(k_0)^T H_U^{sc}(k_0)\gamma_-(k_0)\right]\mathrm{Pf}\left[\gamma_+(k_0)^T H_U^{sc}(k_0)\gamma_+(k_0)\right] = \mathrm{Pf} H_U^{sc}(k_0).$$

Here, $\gamma(k_0) = [\gamma_+(k_0), \gamma_-(k_0)]$, the columns of $\gamma_\pm(k_0)$ are the eigenvectors of $I^{sc}(k_0)$ corresponding to eigenvalues ± 1 and we have utilized the fact that the dimension d_- of the eigen-

value -1 subspace is always a multiple of 4. Therefore, the two Pfaffians are always equal at the high-symmetry momenta $k_0 = 0, \pi$.

[1] T. H. Hsieh, H. Lin, J. Liu, W. Duan, A. Bansil, and L. Fu, Topological crystalline insulators in the SnTe material class, Nat. Commun. **3**, 982 (2012).

[2] P. Dziawa, B. J. Kowalski, K. Dybko, R. Buczko, A. Szczerbakow, M. Szot, E. Lusakowska, T. Balasubramanian, B. M. Wojek, M. H. Berntsen, O. Tjernberg, and T. Story, Topological crystalline insulator states in $Pb_{1-x}Sn_xSe$, Nat. Mater. **11**, 1023 (2012).

[3] Y. Tanaka, Z. Ren, T. Sato, K. Nakayama, S. Souma, T. Takahashi, K. Segawa, and Y. Ando, Experimental realization of a topological crystalline insulator in SnTe, Nat. Phys. **8**, 800 (2012).

[4] S.-Y. Xu, C. Liu, N. Alidoust, M. Neupane, D. Qian, I. Belopolski, J. Denlinger, Y. Wang, H. Lin, L. Wray, G. Landolt, B. Slomski, J. Dil, A. Marcinkova, E. Morosan, Q. Gibson, R. Sankar, F. Chou, R. Cava, A. Bansil *et al.*, Observation of a topological crystalline insulator phase and topological phase transition in $Pb_{1-x}Sn_xTe$, Nat. Commun. **3**, 1192 (2012).

[5] P. Sessi, D. Di Sante, A. Szczerbakow, F. Glott, S. Wilfert, H. Schmidt, T. Bathon, P. Dziawa, M. Greiter, T. Neupert, G. Sangiovanni, T. Story, R. Thomale, and M. Bode, Robust spin-polarized midgap states at step edges of topological crystalline insulators, Science **354**, 1269 (2016).

[6] R. Rechciński and R. Buczko, Topological states on uneven (Pb,Sn)Se (001) surfaces, Phys. Rev. B **98**, 245302 (2018).

[7] G. P. Mazur, K. Dybko, A. Szczerbakow, J. Z. Domagala, A. Kazakov, M. Zgirski, E. Lusakowska, S. Kret, J. Korczak, T. Story, M. Sawicki, and T. Dietl, Experimental search for the origin of low-energy modes in topological materials, Phys. Rev. B **100**, 041408(R) (2019).

[8] W. Brzezicki, M. M. Wysokiński, and T. Hyart, Topological properties of multilayers and surface steps in the SnTe material class, Phys. Rev. B **100**, 121107(R) (2019).

[9] W. Brzezicki and T. Hyart, Topological domain wall states in a nonsymmorphic chiral chain, Phys. Rev. B **101**, 235113 (2020).

[10] T. Löthman and A. M. Black-Schaffer, Universal phase diagrams with superconducting domes for electronic flat bands, Phys. Rev. B **96**, 064505 (2017).

[11] R. Ojajärvi, T. Hyart, M. A. Silaev, and T. T. Heikkilä, Competition of electron-phonon mediated superconductivity and Stoner magnetism on a flat band, Phys. Rev. B **98**, 054515 (2018).

[12] J. Liu and L. Fu, Electrically tunable quantum spin Hall state in topological crystalline insulator thin films, Phys. Rev. B **91**, 081407(R) (2015).

[13] S. Safaei, M. Galicka, P. Kacman, and R. Buczko, Quantum spin Hall effect in IV-VI topological crystalline insulators, New J. Phys. **17**, 063041 (2015).

[14] J. Liu, T. H. Hsieh, P. Wei, W. Duan, J. Moodera, and L. Fu, Spin-filtered edge states with an electrically tunable gap in a two-dimensional topological crystalline insulator, Nat. Mater. **13**, 178 (2014).

[15] A. Kazakov, W. Brzezicki, T. Hyart, B. Turowski, J. Polaczynski, Z. Adamus, M. Aleszkiewicz, T. Wojciechowski, J. Z. Domagala, O. Caha, A. Varykhalov, G. Springholz, T. Wojtowicz, V. V. Volobuev, and T. Dietl, Dephasing by mirror-symmetry breaking and resulting magnetoresistance across the topological transition in $Pb_{1-x}Sn_xSe$, Phys. Rev. B **103**, 245307 (2021).

[16] F. Schindler, A. M. Cook, M. G. Vergniory, Z. Wang, S. S. P. Parkin, B. A. Bernevig, and T. Neupert, Higher-order topological insulators, Sci. Adv. **4**, eaat0346 (2018).

[17] C.-H. Hsu, P. Stano, J. Klinovaja, and D. Loss, Majorana Kramers Pairs in Higher-Order Topological Insulators, Phys. Rev. Lett. **121**, 196801 (2018).

[18] S. Sasaki, Z. Ren, A. A. Taskin, K. Segawa, L. Fu, and Y. Ando, Odd-Parity Pairing and Topological Superconductivity in a Strongly Spin-Orbit Coupled Semiconductor, Phys. Rev. Lett. **109**, 217004 (2012).

[19] G. Balakrishnan, L. Bawden, S. Cavendish, and M. R. Lees, Superconducting properties of the In-substituted topological crystalline insulator SnTe, Phys. Rev. B **87**, 140507(R) (2013).

[20] C. Fang, M. J. Gilbert, and B. A. Bernevig, New Class of Topological Superconductors Protected by Magnetic Group Symmetries, Phys. Rev. Lett. **112**, 106401 (2014).

[21] P. Kumaravadivel, G. A. Pan, Y. Zhou, Y. Xie, P. Liu, and J. J. Cha, Synthesis and superconductivity of In-doped SnTe nanostructures, APL Mater. **5**, 076110 (2017).

[22] H. Yang, Y.-Y. Li, T.-T. Liu, H.-Y. Xue, D.-D. Guan, S.-Y. Wang, H. Zheng, C.-H. Liu, L. Fu, and J.-F. Jia, Superconductivity of topological surface states and strong proximity effect in $Sn_{1-x}Pb_xTe$-Pb heterostructures, Adv. Mater. **31**, 1905582 (2019).

[23] A. Bliesener, J. Feng, A. A. Taskin, and Y. Ando, Superconductivity in $Sn_{1-x}In_xTe$ thin films grown by molecular beam epitaxy, Phys. Rev. Materials **3**, 101201(R) (2019).

[24] B. Rachmilowitz, H. Zhao, H. Li, A. LaFleur, J. Schneeloch, R. Zhong, G. Gu, and I. Zeljkovic, Proximity-induced superconductivity in a topological crystalline insulator, Phys. Rev. B **100**, 241402(R) (2019).

[25] C. J. Trimble, M. T. Wei, N. F. Q. Yuan, S. S. Kalantre, P. Liu, H.-J. Han, M.-G. Han, Y. Zhu, J. J. Cha, L. Fu, and J. R. Williams, Josephson detection of time reversal symmetry broken superconductivity in SnTe nanowires, npj Quantum Materials **6**, 61 (2021).

[26] C. Fang, M. J. Gilbert, and B. A. Bernevig, Large-Chern-Number Quantum Anomalous Hall Effect in Thin-Film Topological Crystalline Insulators, Phys. Rev. Lett. **112**, 046801 (2014).

[27] K. Dybko, M. Szot, A. Szczerbakow, M. U. Gutowska, T. Zajarniuk, J. Z. Domagala, A. Szewczyk, T. Story, and W. Zawadzki, Experimental evidence for topological surface states wrapping around a bulk SnTe crystal, Phys. Rev. B **96**, 205129 (2017).

[28] G. Nimtz and B. Schlicht, Narrow-gap lead salts, in *Narrow-Gap Semiconductors,* Springer Tracts in Modern Physics, Vol. 98 (Springer, Berlin, 1983).

[29] T. Story, R. R. Gałązka, R. B. Frankel, and P. A. Wolff, Carrier-Concentration-Induced Ferromagnetism in PbSnMnTe, Phys. Rev. Lett. **56**, 777 (1986).

[30] T. Story, G. Karczewski, L. Świerkowski, and R. R. Gałązka, Magnetism and band structure of the semimagnetic semiconductor Pb-Sn-Mn-Te, Phys. Rev. B **42**, 10477 (1990).

[31] M. D. Nielsen, E. M. Levin, C. M. Jaworski, K. Schmidt-Rohr, and J. P. Heremans, Chromium as resonant donor impurity in PbTe, Phys. Rev. B **85**, 045210 (2012).

[32] K. Chang, J. Liu, H. Lin, N. Wang, K. Zhao, A. Zhang, F. Jin, Y. Zhong, X. Hu, W. Duan, Q. Zhang, L. Fu, Q.-K. Xue, X. Chen, and S.-H. Ji, Discovery of robust in-plane ferroelectricity in atomic-thick SnTe, Science **353**, 274 (2016).

[33] J. Kim, K.-W. Kim, D. Shin, S.-H. Lee, J. Sinova, N. Park, and H. Jin, Prediction of ferroelectricity-driven Berry curvature enabling charge- and spin-controllable photocurrent in tin telluride monolayers, Nat. Commun. **10**, 3965 (2019).

[34] Z. Fu, M. Liu, and Z. Yang, Substrate effects on the in-plane ferroelectric polarization of two-dimensional SnTe, Phys. Rev. B **99**, 205425 (2019).

[35] V. V. Volobuev, P. S. Mandal, M. Galicka, O. Caha, J. Sánchez-Barriga, D. Di Sante, A. Varykhalov, A. Khiar, S. Picozzi, G. Bauer, P. Kacman *et al.* Giant Rashba splitting in $Pb_{1-x}Sn_xTe$ (111) topological crystalline insulator films controlled by Bi doping in the bulk, Adv. Mater. **29**, 1604185 (2017).

[36] H. Lee, J. Im, and H. Jin, Emergence of the giant out-of-plane Rashba effect and tunable nanoscale persistent spin helix in ferroelectric SnTe thin films, Appl. Phys. Lett. **116**, 022411 (2020).

[37] R. Rechciński, M. Galicka, M. Simma, V. V. Volobuev, O. Caha, J. Sánchez-Barriga, P. S. Mandal, E. Golias, A. Varykhalov, O. Rader *et al.*, Structure inversion asymmetry and Rashba effect in quantum confined topological crystalline insulator heterostructures, Adv. Funct. Mater. **31**, 2008885 (2021).

[38] P. Liu, H. J. Han, J. Wei, D. Hynek, J. L. Hart, M. G. Han, C. J. Trimble, J. Williams, Y. Zhu, and J. J. Cha, Synthesis of narrow SnTe nanowires using alloy nanoparticles, ACS Appl. Elec. Mater. **3**, 184 (2021).

[39] J. Sadowski, P. Dziawa, A. Kaleta, B. Kurowska, A. Reszka, T. Story, and S. Kret, Defect-free SnTe topological crystalline insulator nanowires grown by molecular beam epitaxy on graphene, Nanoscale **10**, 20772 (2018).

[40] A. Altland and M. R. Zirnbauer, Nonstandard symmetry classes in mesoscopic normal-superconducting hybrid structures, Phys. Rev. B **55**, 1142 (1997).

[41] L. Trifunovic and P. W. Brouwer, Higher-Order Bulk-Boundary Correspondence for Topological Crystalline Phases, Phys. Rev. X **9**, 011012 (2019).

[42] M. Geier, P. W. Brouwer, and L. Trifunovic, Symmetry-based indicators for topological Bogoliubov–de Gennes Hamiltonians, Phys. Rev. B **101**, 245128 (2020).

[43] L. Trifunovic and P. W. Brouwer, Higher-order topological band structures, Phys. Status Solidi B **258**, 2000090 (2021).

[44] C. Nayak, S. H. Simon, A. Stern, M. Freedman, and S. Das Sarma, Non-Abelian anyons and topological quantum computation, Rev. Mod. Phys. **80**, 1083 (2008).

[45] S. D. Sarma, M. Freedman, and C. Nayak, Majorana zero modes and topological quantum computation, npj Quantum Inf. **1**, 15001 (2015).

[46] C. W. J. Beenakker, Search for non-Abelian Majorana braiding statistics in superconductors, SciPost Phys. Lect. Notes 15 (2020).

[47] K. Flensberg, F. von Oppen, and A. Stern, Engineered platforms for topological superconductivity and Majorana zero modes, Nat. Rev. Mater. **6**, 944 (2021).

[48] T.-P. Choy, J. M. Edge, A. R. Akhmerov, and C. W. J. Beenakker, Majorana fermions emerging from magnetic nanoparticles on a superconductor without spin-orbit coupling, Phys. Rev. B **84**, 195442 (2011).

[49] S. Nadj-Perge, I. K. Drozdov, J. Li, H. Chen, S. Jeon, J. Seo, A. H. MacDonald, B. A. Bernevig, and A. Yazdani, Observation of Majorana fermions in ferromagnetic atomic chains on a superconductor, Science **346**, 602 (2014).

[50] L. Kimme and T. Hyart, Existence of zero-energy impurity states in different classes of topological insulators and superconductors and their relation to topological phase transitions, Phys. Rev. B **93**, 035134 (2016).

[51] L. Fu and C. L. Kane, Superconducting Proximity Effect and Majorana Fermions at the Surface of a Topological Insulator, Phys. Rev. Lett. **100**, 096407 (2008).

[52] R. M. Lutchyn, J. D. Sau, and S. Das Sarma, Majorana Fermions and a Topological Phase Transition in Semiconductor-Superconductor Heterostructures, Phys. Rev. Lett. **105**, 077001 (2010).

[53] Y. Oreg, G. Refael, and F. von Oppen, Helical Liquids and Majorana Bound States in Quantum Wires, Phys. Rev. Lett. **105**, 177002 (2010).

[54] V. Mourik, K. Zuo, S. M. Frolov, S. R. Plissard, E. P. A. M. Bakkers, and L. P. Kouwenhoven, Signatures of Majorana fermions in hybrid superconductor-semiconductor nanowire devices, Science **336**, 1003 (2012).

[55] M. Wimmer, Algorithm 923 Efficient numerical computation of the Pfaffian for dense and banded skew-symmetric matrices, ACM Trans. Math. Software **38**, 1 (2012).

[56] Y. X. Zhao, A. P. Schnyder, and Z. D. Wang, Unified Theory of *pt* and *cp* Invariant Topological Metals and Nodal Superconductors, Phys. Rev. Lett. **116**, 156402 (2016).

[57] C. Chamon, R. Jackiw, Y. Nishida, S.-Y. Pi, and L. Santos, Quantizing Majorana fermions in a superconductor, Phys. Rev. B **81**, 224515 (2010); C. W. J. Beenakker, Annihilation of Colliding Bogoliubov Quasiparticles Reveals Their Majorana Nature, Phys. Rev. Lett. **112**, 070604 (2014).

[58] M. P. L. Sancho, J. M. L. Sancho, J. M. L. Sancho, and J. Rubio, Highly convergent schemes for the calculation of bulk and surface Green functions, J. Phys. F **15**, 851 (1985).

[59] A. R. Akhmerov, J. P. Dahlhaus, F. Hassler, M. Wimmer, and C. W. J. Beenakker, Quantized Conductance at the Majorana Phase Transition in a Disordered Superconducting Wire, Phys. Rev. Lett. **106**, 057001 (2011).

[60] K. T. Law, P. A. Lee, and T. K. Ng, Majorana Fermion Induced Resonant Andreev Reflection, Phys. Rev. Lett. **103**, 237001 (2009).

[61] A. Y. Kitaev, Unpaired Majorana fermions in quantum wires, Phys. Usp. **44**, 131 (2001).

Chapter 6

Unprotected edge modes in quantum spin Hall insulator candidate materials

6.1 Summary

Numerous materials have been anticipated to exhibit the QSH insulator phase [7, 37, 50, 69] which predicts the existence of helical edge modes, which are topologically protected against elastic backscattering from all perturbations obeying the time-reversal symmetry. Experimental evidence of edge mode transport has been observed in several materials like HgTe/CdTe quantum wells [46], InAs/GaSb bilayers [24], and WTe_2 [95]. However, experimental studies have also revealed inconsistencies with simple theoretical models. For example, in WTe_2, the edge transport protection length is only a few tens of nanometers [95], while in the more extensively studied InAs/GaSb and HgTe/CdTe quantum wells, the best protection lengths achieved so far are on the order of a few micrometers [24] and a few tens of micrometers [56], respectively. The interpretation of these short protection lengths is still a topic of debate, with various mechanisms, such as magnetic impurities [89], phonons [12], dynamic nuclear polarization [19, 57], spontaneous time-reversal symmetry breaking [65, 66], charge puddles [93], charge dopants [22], and interaction effects [23], potentially contributing to the collapse of topological protection. It is worth mentioning that a recent theoretical study on InAs/GaSb heterostructures also reported the existence of trivial helical states [55]. The theoretical analysis of the edge modes in these materials has so far been based on effective models such as the Bernevig-Hughes-Zhang model discussed in Chapter. 1 of this thesis.

In this paper, we use first-principles calculations to derive an effective tight-binding model for HgTe/CdTe, HgS/CdTe and InAs/GaSb heterostructures. Our investigation reveals that these materials exhibit additional edge states that are influenced by the edge termination. Importantly, these edge modes are not captured by the Bernevig-Hughes-Zhang model, and therefore their existence has not been discussed in the existing literature. We show that the origin of these states can be traced back to a minimal model of a buckled honeycomb lattice of anions and cations, which serves as the fundamental building block for constructing these heterostructures. This minimal model supports flat bands with nontrivial quantum

geometry, resulting in polarization charges at the edges [74]. More precisely, we go beyond the theory described in Ref. [74] by showing that in this system the polarization charge is determined by the sum of Zak phases of multiple flat bands so that the boundary charge increases proportionally to the width of the system. When the flat bands are coupled with each other and other states to form the Hamiltonian describing the full heterostructure, the polarization charges transform into the additional edge states in the full heterostructure. In HgTe/CdTe quantum wells, the additional edge states lie far from the Fermi level, thus not contributing significantly to transport. However, in HgS/CdTe and InAs/GaSb heterostructures, these states appear within the bulk energy gap, enabling the possibility of multi-mode edge transport, consistent with experimental observations [18, 61]. Notably, we have found that these additional edge states are not topological. Therefore, by applying an edge potential, it may be possible to eliminate them from the energy gap between the valence and conduction bands. This observation sheds light on the improvement of the quality of the quantum spin Hall effect through impurity doping in InAs/GaSb bilayers [24] and gate training in HgTe/CdTe quantum wells [56]. In our paper, we have also shown that the edge termination and stacking direction influence the properties of the nontopological edge modes, but the edge modes are quite generically present in heterostructures grown along various different directions. Moreover, we have established a theoretical framework, which can be utilized in the more detailed future investigations of the influences of choices of materials, stacking direction and edge termination on the nontopological edge modes, hopefully leading to the improvement of the quality of the quantum spin Hall effect.

6.2   Publication II

Date: 8 August 2023

STATEMENT

I declare that I am the co-author of the publication **N. M. Nguyen**, G. Cuono, R. Islam, C. Autieri, T. Hyart, W. Brzezicki, Unprotected edge modes in quantum spin Hall insulator candidate materials, Phys. Rev. B 107, 045138 (2023), arXiv:2209.06912 (2022).

My contribution was analyzing the model, writing the codes, preparing the figures and participating in writing the manuscripst.

Yours Faithfully,

Nguyen Minh Nguyen

Nguyen Minh Nguyen, Group ON-6.1 at the International Centre for Interfacing Magnetism and Superconductivity with Topological Matter (MagTop),
E-mail: nmnguyen@magtop.ifpan.edu.pl
Website: https://www.magtop.ifpan.edu.pl/resources/teams/

Date: 6 August 2023

STATEMENT

I declare that my contribution to the paper **N. M. Nguyen**, G. Cuono, R. Islam, C. Autieri, T. Hyart, W. Brzezicki, Unprotected edge modes in quantum spin Hall insulator candidate materials, Phys. Rev. B 107, 045138 (2023), arXiv:2209.06912 (2022), has been related to discussion on the scientific project and writing one section related to density functional theory.

Yours Faithfully,

Carmine Autieri

Assoc. Prof. Dr. hab. Carmine Autieri, Group leader of ON-6.5 at the International Centre for Interfacing Magnetism and Superconductivity with Topological Matter (MagTop),
E-mail: autieri@MagTop.ifpan.edu.pl
Website: https://www.magtop.ifpan.edu.pl/resources/teams/
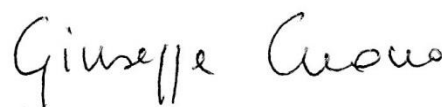Google Scholar profile: https://scholar.google.it/citations?user=83pF0ywAAAA
ResearchGate profile: https://www.researchgate.net/profile/Carmine_Autieri

Date: 6 August 2023

STATEMENT

I declare that my contribution to the paper **N. M. Nguyen**, G. Cuono, R. Islam, C. Autieri, T. Hyart, W. Brzezicki, Unprotected edge modes in quantum spin Hall insulator candidate materials, Phys. Rev. B 107, 045138 (2023), arXiv:2209.06912 (2022), has been related to discussion on the scientific project and writing one section related to density functional theory.

Yours Faithfully,

Giuseppe Cuono

Dr. Giuseppe Cuono
Young Doctor,
ON-6.5, International Research Centre MagTop, Institute of Physics, Polish Academy of Sciences,
aleja Lotników 32/46, Warsaw, Poland
E-mail: gcuono@magtop.ifpan.edu.pl
Website: https://www.magtop.ifpan.edu.pl/resources/teams/
Google Scholar profile: https://scholar.google.com/citations?user=lXZP7u4AAAAJ&hl=it
Research gate profile: https://www.researchgate.net/profile/Giuseppe_Cuono

Date: 6 August 2023

STATEMENT

I Rajibul Islam declare that my contribution to the paper **N. M. Nguyen**, G. Cuono, R. Islam, C. Autieri, T. Hyart, W. Brzezicki, Unprotected edge modes in quantum spin Hall insulator candidate materials, Phys. Rev. B 107, 045138 (2023), arXiv:2209.06912 (2022), has been related to discussion on the scientific project and writing one section related to density functional theory.

Yours Faithfully,

Dr.Rajibul Islam ,   ON-6.5 at the International Centre for Interfacing Magnetism and Superconductivity with Topological Matter (MagTop),
E-mail: rislam2@uab.edu
Website: https://sites.google.com/view/quantum-world-with-islam/home
Google Scholar profile: https://scholar.google.pl/citations?user=or0ONZgAAAAJ&hl=en
ResearchGate profile: https://www.researchgate.net/profile/Rajibul-Islam

Date: 6 August 2023

STATEMENT

I declare that my contribution to the paper **N. M. Nguyen**, G. Cuono, R. Islam, C. Autieri, T. Hyart, W. Brzezicki, Unprotected edge modes in quantum spin Hall insulator candidate materials, Phys. Rev. B 107, 045138 (2023) has been related to the formulation of the research questions for the project, exchange of ideas during regular meetings, writing part of the manuscript, and supervision of the project.

Yours Faithfully,

Timo Hyart

Timo Hyart
Research Fellow, Aalto University, E-mail: timo.hyart@aalto.fi
https://research.aalto.fi/en/persons/timo-hyart
https://scholar.google.fi/citations?user=fq1cObMAAAAJ&hl=fi

Date: 11 August 2023

STATEMENT

I declare that my contribution to the paper **N. M. Nguyen**, G. Cuono, R. Islam, C. Autieri, T. Hyart, W. Brzezicki, *Unprotected edge modes in quantum spin Hall insulator candidate materials*, Phys. Rev. B 107, 045138 (2023), has been related to the analysis of symmetries and formulation of topological invariants, formulation of the research questions for the project, exchange of ideas during regular meetings and writing part of the manuscript.

Yours Faithfully,

dr hab. Wojciech Brzezicki

Unprotected edge modes in quantum spin Hall insulator candidate materials

Nguyen Minh Nguyen [1], Giuseppe Cuono [1], Rajibul Islam,[1] Carmine Autieri [1,2,*]
Timo Hyart [3,4,1,†] and Wojciech Brzezicki [1,5,‡]

[1]*International Research Centre MagTop, Institute of Physics, Polish Academy of Sciences, Aleja Lotników 32/46, PL-02668 Warsaw, Poland*
[2]*Consiglio Nazionale delle Ricerche CNR-SPIN, UOS Salerno, I-84084 Fisciano (Salerno), Italy*
[3]*Computational Physics Laboratory, Physics Unit, Faculty of Engineering and Natural Sciences,*
Tampere University, FI-33014 Tampere, Finland
[4]*Department of Applied Physics, Aalto University, FI-00076 Aalto, Espoo, Finland*
[5]*Institute of Theoretical Physics, Jagiellonian University, ulica S. Łojasiewicza 11, PL-30348 Kraków, Poland*

The experiments in quantum spin Hall insulator candidate materials, such as HgTe/CdTe and InAs/GaSb heterostructures, indicate that in addition to the topologically protected helical edge modes, these multilayer heterostructures may also support additional edge states, which can contribute to scattering and transport. We use first-principles calculations to derive an effective tight-binding model for HgTe/CdTe, HgS/CdTe, and InAs/GaSb heterostructures, and we show that all these materials support additional edge states which are sensitive to edge termination. We trace the microscopic origin of these states back to a minimal model supporting flat bands with a nontrivial quantum geometry that gives rise to polarization charges at the edges. We show that the polarization charges transform into additional edge states when the flat bands are coupled to each other and to the other states to form the Hamiltonian describing the full heterostructure. Interestingly, in HgTe/CdTe quantum wells the additional edge states are far away from the Fermi level so that they do not contribute to the transport, but in the HgS/CdTe and InAs/GaSb heterostructures they appear within the bulk energy gap, giving rise to the possibility of multimode edge transport. Finally, we demonstrate that because these additional edge modes are nontopological it is possible to remove them from the bulk energy gap by modifying the edge potential, for example, with the help of a side gate or chemical doping.

I. INTRODUCTION

The theory of the quantum spin Hall (QSH) effect predicts the existence of helical edge modes, which are topologically protected against elastic backscattering from all perturbations obeying time-reversal symmetry, and various materials have been predicted to support the QSH insulator phase [1–4]. Experimentally, signatures of edge mode transport have been observed in several of the candidate materials such as HgTe/CdTe quantum wells [5], InAs/GaSb bilayers [6], and WTe$_2$ [7]. However, experimental studies have also led to discrepancies with the simple theoretical models. In WTe$_2$ the protection length of the edge transport is only a few tens of nanometers [7], and even in the more extensively studied InAs/GaSb and HgTe/CdTe quantum wells the best protection lengths reached so far are on the order of a few micrometers [6] and a few tens of micrometers [8], respectively. There is still no consensus about the interpretation of the observed short protection lengths but various mechanisms, such as magnetic impurities [9], phonons [10], dynamic nuclear polarization [11,12], spontaneous time-reversal sym-

metry breaking [13,14], charge puddles [15], charge dopants [16], and interaction effects [17], may contribute to the breakdown of topological protection.

The quality of the edge transport can be improved with the help of impurity doping in InAs/GaSb bilayers [6] and gate training in HgTe/CdTe quantum wells [8], indicating that there likely exist some additional unprotected low-energy states, which are contributing to the breakdown of the topological protection and which are influenced by these sample preparation techniques. In certain experiments unprotected edge states have been observed also more directly. Namely, in InAs/GaSb bilayers, in the absence of impurity doping, multimode edge transport has been experimentally observed in the trivial regime [18]. In HgTe/CdTe quantum wells the additional states seem to be sufficiently far away from the Fermi level so that they do not contribute to transport, but the dynamical properties suggest that the topological edge states are surrounded by additional states contributing to scattering [19]. The microscopic origin of these additional states remains unknown in both materials.

In this paper, we use first-principles calculations to derive an effective tight-binding model for HgTe/CdTe, HgS/CdTe, and InAs/GaSb heterostructures, and we show that all these materials support additional edge states which are sensitive to the edge termination. We trace the microscopic origin of these states back to a minimal model of a buckled honeycomb

TABLE I. Tight-binding parameters (in eV) of different materials.

Parameters	HgTe	HgS	CdTe	InAs	GaSb	AlSb
V_{s_a}	-5.8329	-12.1315	-6.1832	-7.8000	-5.4804	-4.2606
V_{s_c}	0.2069	-1.5535	1.6395	-3.5834	-5.5334	-3.0847
V_{p_a}	3.1483	-1.1909	2.3251	-0.1424	-0.2514	0.4210
V_{p_c}	7.6916	5.4898	7.4584	4.1314	2.8382	3.9110
$V_{ss\sigma}$	-1.2569	-0.1162	-1.2431	-0.1424	-0.2514	0.4210
$V_{s_a p_c \sigma}$	1.7229	2.8306	1.6379	-1.4257	-1.5325	-1.6150
$V_{s_c p_a \sigma}$	1.4834	1.1517	1.5463	1.4669	1.2761	1.3486
$V_{pp\sigma}$	2.2132	1.5759	2.0139	2.2223	2.200	2.0384
$V_{pp\pi}$	-0.9830	-0.4231	-0.9875	-1.1509	-1.1513	-1.1146
λ_a	$0.3943/2$	$-0.0159/2$	$0.5350/2$	$0.2083/2$	$0.4423/2$	$0.4237/2$
λ_c	$0.7216/2$	$0.7651/2$	$0.1950/2$	$0.2856/2$	$0.1246/2$	$0.0306/2$
E_f	3.32248	-1.33027	3.32331	0.173742	0.293268	1.71368

lattice of anions and cations. This system is the minimal building block for constructing HgTe/CdTe, HgS/CdTe, and InAs/GaSb heterostructures, and it supports flat bands with nontrivial quantum geometry that gives rise to polarization charges at the edges [20]. We show that the polarization charges transform into additional edge states when the flat bands are coupled to each other and to the other states to form the Hamiltonian describing the full heterostructure. In HgTe/CdTe quantum wells the additional edge states are far away from the Fermi level so that they do not contribute to the transport, but in the HgS/CdTe and InAs/GaSb heterostructures they appear within the bulk energy gap, giving rise to the possibility of multimode edge transport, in agreement with experiments [18,19]. Finally, we demonstrate that because these additional edge modes are nontopological, it is possible

to remove them from the bulk energy gap by modifying the edge potential, for example, with the help of a side gate or chemical doping, providing a possible explanation for the mysterious improvement of the quality of the QSH effect with the help of impurity doping in InAs/GaSb bilayers [6] and gate training in HgTe/CdTe quantum wells [8]. We note that trivial helical states were also reported in a recent theoretical work on InAs/GaSb heterostructures [21].

II. HETEROSTRUCTURE HAMILTONIAN AND NONTOPOLOGICAL EDGE STATES

Our starting point are the Hamiltonians for HgTe, HgS, CdTe, InAs, GaSb, and AlSb bulk crystals,

$$
\mathcal{H}(\mathbf{k}) = \mathbb{1}_2 \otimes h_A \otimes \begin{pmatrix} 0 & e^{ik_3} \\ 0 & 0 \end{pmatrix} + \mathbb{1}_2 \otimes h_B \otimes \begin{pmatrix} 0 & e^{ik_1} \\ 0 & 0 \end{pmatrix} + \mathbb{1}_2 \otimes h_C \otimes \begin{pmatrix} 0 & 1 \\ 0 & 0 \end{pmatrix} + \mathbb{1}_2 \otimes h_D \otimes \begin{pmatrix} 0 & e^{i(k_3 - k_2)} \\ 0 & 0 \end{pmatrix} + \text{H.c.}
$$

$$
+ \mathbb{1}_2 \otimes E_c \otimes \begin{pmatrix} 1 & 0 \\ 0 & 0 \end{pmatrix} + \mathbb{1}_2 \otimes E_a \otimes \begin{pmatrix} 0 & 0 \\ 0 & 1 \end{pmatrix} - \sum_{\alpha=1,2,3} \sigma_\alpha \otimes L_\alpha \otimes \begin{pmatrix} \lambda_c & 0 \\ 0 & \lambda_a \end{pmatrix} - E_f \otimes \mathbb{1}_{16}, \tag{1}
$$

$$
h_A = h\left(\frac{1}{\sqrt{3}}, \frac{1}{\sqrt{3}}, \frac{1}{\sqrt{3}}\right), \quad h_B = h\left(\frac{1}{\sqrt{3}}, -\frac{1}{\sqrt{3}}, -\frac{1}{\sqrt{3}}\right), \quad h_C = h\left(-\frac{1}{\sqrt{3}}, \frac{1}{\sqrt{3}}, -\frac{1}{\sqrt{3}}\right), \quad h_D = h\left(-\frac{1}{\sqrt{3}}, -\frac{1}{\sqrt{3}}, \frac{1}{\sqrt{3}}\right), \tag{2}
$$

$$
h(l, m, n) = \begin{pmatrix} V_{ss\sigma} & l V_{s_c p_a \sigma} & m V_{s_c p_a \sigma} & n V_{s_c p_a \sigma} \\ -l V_{s_a p_c \sigma} & l^2 (V_{pp\sigma} - V_{pp\pi}) + V_{pp\pi} & lm(-V_{pp\pi} + V_{pp\sigma}) & ln(-V_{pp\pi} + V_{pp\sigma}) \\ -m V_{s_a p_c \sigma} & lm(-V_{pp\pi} + V_{pp\sigma}) & m^2 (V_{pp\sigma} - V_{pp\pi}) + V_{pp\pi} & mn(-V_{pp\pi} + V_{pp\sigma}) \\ -n V_{s_a p_c \sigma} & ln(-V_{pp\pi} + V_{pp\sigma}) & mn(-V_{pp\pi} + V_{pp\sigma}) & n^2 (V_{pp\sigma} - V_{pp\pi}) + V_{pp\pi} \end{pmatrix}, \tag{3}
$$

$$
L_x = i \begin{pmatrix} 0 & 0 & 0 & 0 \\ 0 & 0 & 1 & 0 \\ 0 & -1 & 0 & 0 \\ 0 & 0 & 0 & 0 \end{pmatrix}, \quad L_y = i \begin{pmatrix} 0 & 0 & 0 & 0 \\ 0 & 0 & 0 & -1 \\ 0 & 0 & 0 & 0 \\ 0 & 1 & 0 & 0 \end{pmatrix}, \quad L_z = i \begin{pmatrix} 0 & 0 & 0 & 0 \\ 0 & 0 & 0 & 0 \\ 0 & 0 & 0 & 1 \\ 0 & 0 & -1 & 0 \end{pmatrix}, \quad E_{a(c)} = \begin{pmatrix} V_{s_{a(c)}} & 0 & 0 & 0 \\ 0 & V_{p_{a(c)}} & 0 & 0 \\ 0 & 0 & V_{p_{a(c)}} & 0 \\ 0 & 0 & 0 & V_{p_{a(c)}} \end{pmatrix}, \tag{4}
$$

where the tight-binding parameters for each material, given in Table I, have been derived from first-principles density-functional theory (DFT) calculations. To obtain the tight-binding with first-neighbor hopping parameters, we impose to the tight-binding model to fit the DFT band structure at the high-symmetry points extracting the on-site energies,

the hopping amplitudes, and the spin-orbit couplings as fitting parameters. More technical information is provided in Appendixes A and B. Here, the unit cell of the zinc-blende crystal structure contains two lattice sites, anions and cations, at positions $(0,0,0)$ and $(1/2, 1/2, 1/2)$ with lattice translation vectors being $\mathbf{n}_1 = (1, 1, 0)$, $\mathbf{n}_2 = (-1, 1, 0)$, and
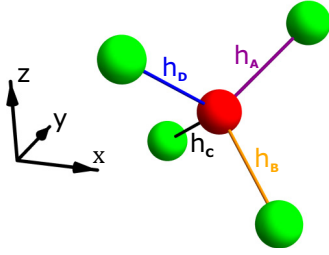
FIG. 1. Schematic illustration of the hopping matrices h_α ($\alpha = A, B, C, D$) between the nearest-neighbor lattice sites in zinc-blende crystals. Each cation (green) and anion (red) supports one s orbital and three p orbitals so that h_i are 4×4 matrices.

$\mathbf{n}_3 = (0, 1, 1)$. Each site in the unit cell supports one s orbital and three p orbitals, h_α are 4×4 matrices describing the hopping amplitudes between the different orbitals of cations and anions [parametrized by $V_{ss\sigma}$, $V_{s_a p_c \sigma}$, $V_{s_c p_a \sigma}$, $V_{pp\sigma}$, and $V_{pp\pi}$ in Eq. (3)] along the different directions $\alpha = A, B, C, D$ as depicted in Fig. 1, matrices $E_{a(c)}$ contain the on-site energies $V_{s_{a(c)}}$ and $V_{p_{a(c)}}$ of the s and p orbitals of the anions (cations), σ_α are Pauli spin matrices, L_α are the 4×4 angular momentum matrices, $\lambda_{a(c)}$ is the spin-orbit coupling strength at the anion (cation) site, and E_f is the Fermi energy.

The two-dimensional (2D) Hamiltonian $\mathcal{H}^{2D}(k_1, k_2)$ of a quantum heterostructure $X_{W_X}/Y_{W_Y}/X_{W_X}$, consisting of W_X unit cells of material X (insulating barrier), W_Y unit cells of material Y (quantum well), and W_X unit cells of material X (insulating barrier), stacked along the $\mathbf{n}_3$ direction, can be written as

$$\mathcal{H}^{2D}(k_1, k_2) = \sum_i |i\rangle\langle i| \otimes H_0(k_1, k_2, i)$$
$$+ \left(\sum_i |i\rangle\langle i+1| \otimes H_1(k_1, k_2, i) + \text{H.c.} \right), \quad (5)$$

where $|i\rangle$ is the basis state for the ith unit cell along the $\mathbf{n}_3$ direction, and

$$H_0(k_1, k_2, i) = \begin{cases} H_0^X, & 0 < i \leqslant W_X, \\ H_0^y, & W_X < i \leqslant W_X + W_Y, \\ H_0^X, & W_X + W_Y < i \leqslant 2W_X + W_Y, \end{cases} \quad (6)$$

$$H_1(k_1, k_2, i) = \begin{cases} H_1^X, & 0 < i < W_X, \\ H_1^{XY}, & i = W_X, \\ H_1^y, & W_X < i < W_X + W_Y, \\ H_1^{XY}, & i = W_X + W_Y, \\ H_1^X, & W_X + W_Y < i \leqslant 2W_X + W_Y, \end{cases} \quad (7)$$

with $H_0^X(k_1, k_2)$ and $H_1^X(k_1, k_2)$ obtained from the Fourier decomposition of $\mathcal{H}(\mathbf{k})$ [Eq. (1)] of material X,

$$\mathcal{H}(\mathbf{k}) = H_0(k_1, k_2) + e^{ik_3} H_1(k_1, k_2) + e^{-ik_3} H_1^\dagger(k_1, k_2). \quad (8)$$

We assume that the hopping matrices between the different materials H_1^{XY} can be written as

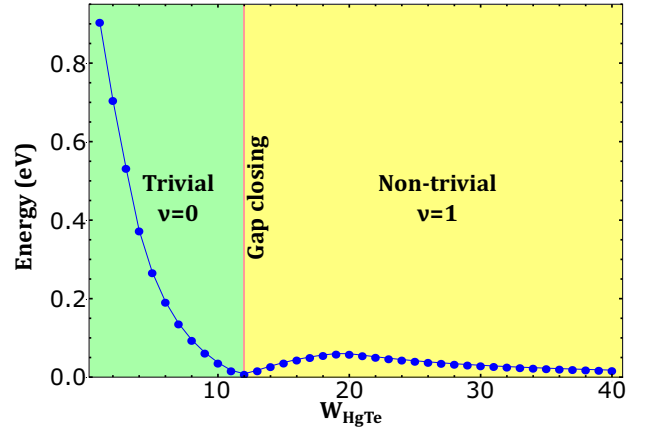$$H_1^{XY} = (1 - x) \frac{H_1^X + H_1^y}{2}, \quad (9)$$

FIG. 2. Energy gap E_{gap} and topological invariant ν as a function of the quantum well thickness W_{HgTe} in a CdTe$_{10}$/HgTe$_{W_{HgTe}}$/CdTe$_{10}$ heterostructure. The transition from the topologically trivial $\nu = 0$ to nontrivial $\nu = 1$ phase takes place at $W_{HgTe,c} = 12$ unit cells.

allowing us to turn the coupling between the materials on and off by changing x continuously from 0 to 1. This is useful in the following when we study the microscopic origin of the nontopological edge modes. If not otherwise stated we use $x = 0$ so that the coupling is turned on. We have benchmarked the tight-binding model by studying the topological phase transition in CdTe/HgTe/CdTe quantum wells. As shown in Fig. 2 we obtain a transition from a topologically trivial to nontrivial phase at $W_{HgTe,c} = 12$ unit cells in approximate agreement with previous studies [2,3].

To study the edge state spectra of these materials we consider one-dimensional ribbons of width W' along the $\mathbf{n}_2$ direction,

$$\mathcal{H}^{1D}(k_1) = \mathbb{1}_{W'} \otimes H_0'(k_1) + D \otimes H_1'(k_1) + D^\mathsf{T} \otimes H_1'^\dagger(k_1), \quad (10)$$

where

$$D = \sum_{i=1}^{W'-1} |i\rangle\langle i+1|, \quad (11)$$

and $H_0'(k_1)$ and $H_1'(k_1)$ are obtained from the Fourier decomposition

$$\mathcal{H}^{2D}(k_1, k_2) = H_0'(k_1) + e^{ik_2} H_1'(k_1) + e^{-ik_2} H_1'^\dagger(k_1). \quad (12)$$

Based on previous studies we expect that CdTe/HgTe/CdTe quantum wells support a pair of counterpropagating helical edge states connecting through the bulk gap in the topologically nontrivial regime $W_{HgTe} > W_{HgTe,c}$ [2,3,5], whereas we expect that there are no edge states in the trivial regime $W_{HgTe} < W_{HgTe,c}$. However, we find that the spectra of CdTe/HgTe/CdTe and CdTe/HgS/CdTe compounds support additional edge states as shown in Figs. 3 and 4, respectively. In the case of CdTe/HgTe/CdTe, the additional edge states appear at energies far away from the bulk gap so that they do not contribute to the transport, but in CdTe/HgS/CdTe the edge states are observed inside the bulk gap, giving rise to the possibility of multimode edge transport. We find that these additional edge states can appear in nontrivial and trivial heterostructures, and in Fig. 4 we also demonstrate that
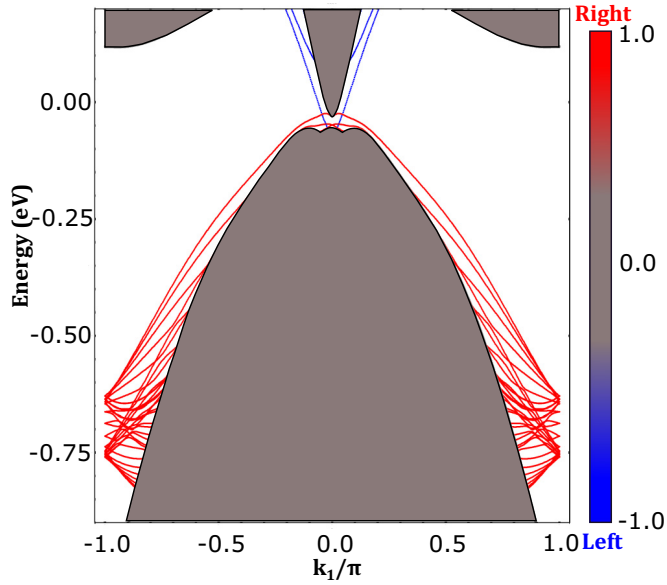
FIG. 3. Edge state spectrum of a topologically nontrivial $CdTe_{10}/HgTe_{16}/CdTe_{10}$ heterostructure with width $W' = 300$ unit cells. The colors (normalized to maximum absolute values) indicate the projection of the eigenstates onto 20 unit cells located at the left (blue) and right (red) edges of the system. Two pairs of topological helical edge states connect the conduction and valence band through the bulk gap. Additionally, there exists a large number of nontopological edge states far away from the Fermi level.
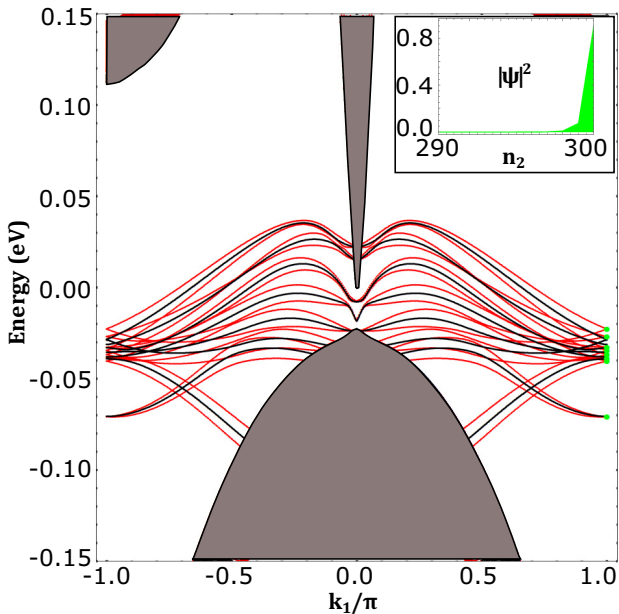

FIG. 5. Edge state spectrum of a topologically trivial $AlSb_{10}/InAs_{10}/GaSb_{10}/AlSb_{10}$ heterostructure with width $W' = 300$ unit cells.

spin-orbit coupling does not play a significant role in the appearance of nontopological edge states. Finally, in Fig. 5 we demonstrate that this type of nontopological edge states appear also in topologically trivial AlSb/InAs/GaSb/AlSb heterostructures inside the bulk gap, giving rise to the possibility of multimode edge transport. In our calculations the nontopological edge modes are mostly localized on one of the edges because we have used particular edge terminations, determined by Eq. (10), in the construction of the ribbons. The dependence on the termination highlights the nontopological nature of the edge modes, but in real materials the edges are not expected to be perfectly ordered, and therefore we expect that the nontopological edge modes are distributed on both edges. In fact, for another stacking direction we indeed find that the edge states appear on both sides of the system (see Appendix C). The rest of the paper is devoted to the understanding of the microscopic origin and the other properties of the nontopological edge states.

FIG. 4. Edge state spectrum of a topologically trivial $CdTe_{10}/HgS_8/CdTe_{10}$ heterostructure with width $W' = 300$ unit cells. In the presence of spin-orbit coupling we have used the same colors as in Fig. 3 (states localized at the right edge are red), whereas in the absence of spin-orbit coupling ($\lambda_{1,2} = 0$) the projection on the right-hand side is indicated with black. Inset: Local density of states (LDOS) as a function of position n_2 close to the right edge for the edge states at $k_1 = \pi$ (green dots).
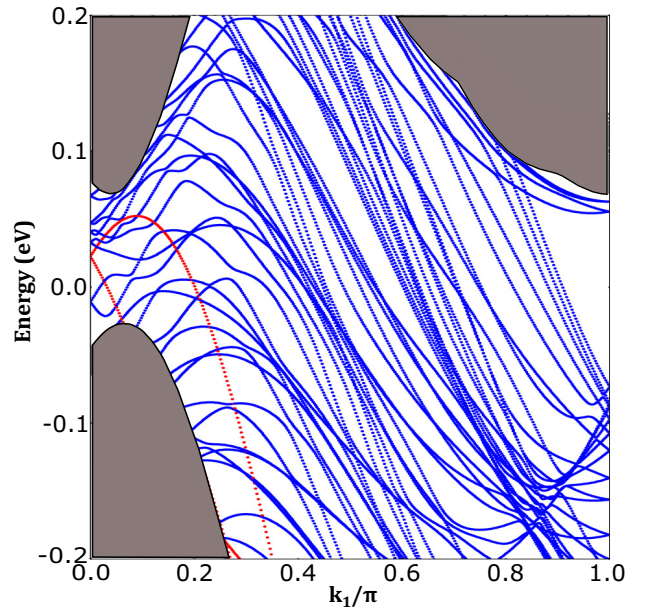
III. MINIMAL MODEL

In order to understand the microscopic origin of the nontopological edge modes, in this section we consider a model for a buckled honeycomb lattice of anions and cations, which can be considered to be the minimal building block for constructing HgTe/CdTe, HgS/CdTe, and InAs/GaSb heterostructures. We note that this minimal model supports flat bands with nontrivial quantum geometry that gives rise to polarization charges at the edges [20]. In Sec. IV we demonstrate that the polarization charges transform into additional edge states when the flat bands are coupled to each other and to the other states to form the Hamiltonian describing the full heterostructure.

The minimal model can obtained from the full three-dimensional Hamiltonian [Eq. (1)] by projecting the model to
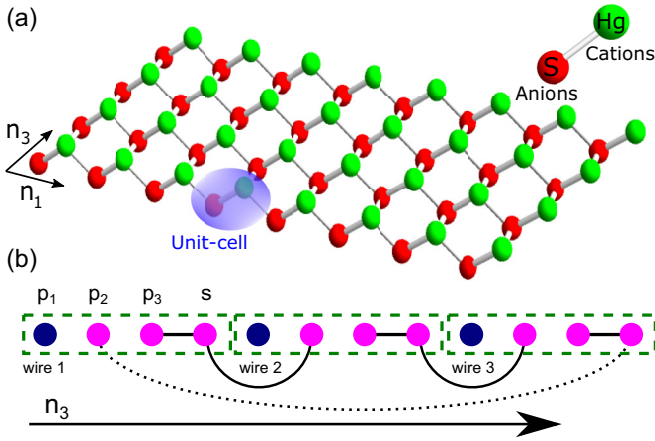
FIG. 6. (a) Buckled honeycomb lattice of anions (red) and cations (green) describing the minimal model. The directions in this two-dimensional system correspond to n_1 and n_3 in the original three-dimensional model [Eq. (1)]. (b) The Zak phases of the flat bands of the model give rise to an accumulated end charge proportional to the width of the ribbon W because of an additional symmetry that allows for the decomposition of the Hamiltonian into diagonal blocks. Each dashed rectangle represents four states, labeled as p_1, p_2, p_3, and s due to their orbital contents, of a single zigzag chain. The states represented by purple (blue) disks form 3×3 (1×1) diagonal blocks after decomposition. The black lines indicate that the states connected by them go to the same block. The dashed black line denotes a coupling, which is present only in the cylinder geometry with periodic boundary conditions in the transverse direction.

s orbitals of cations and p orbitals of anions, neglecting the spin-orbit coupling terms and setting $k_2 = \pi$. Furthermore, we set $E_f = 0$ for simplicity. This way we obtain a buckled honeycomb lattice shown in Fig. 6(a). The 2D bulk Hamiltonian of this system is

$$\mathcal{H}^{2D}(k_1, k_3) = H_\parallel(k_1) + (e^{ik_3} H_\perp + \text{H.c.}), \quad (13)$$

and the 1D Hamiltonian of a W unit cells wide ribbon is

$$\mathcal{H}^{1D}(k_1) = \mathbb{1}_W \otimes H_\parallel(k_1) + (D \otimes H_\perp + \text{H.c.}), \quad (14)$$

where

$$\frac{H_\parallel(k_1)}{E_0} = \begin{pmatrix} \eta_s & e^{ik_1} - 1 & -e^{ik_1} + 1 & -e^{ik_1} - 1 \\ e^{-ik_1} - 1 & \eta_p & 0 & 0 \\ -e^{-ik_1} + 1 & 0 & \eta_p & 0 \\ -e^{-ik_1} - 1 & 0 & 0 & \eta_p \end{pmatrix},$$

$$\frac{H_\perp}{E_0} = \begin{pmatrix} 0 & 2 & 2 & 0 \\ 0 & 0 & 0 & 0 \\ 0 & 0 & 0 & 0 \\ 0 & 0 & 0 & 0 \end{pmatrix}, \quad E_0 = \frac{V_{s_c p_a \sigma}}{\sqrt{3}}, \quad \eta_s = \frac{V_{s_c}}{E_0}, \quad \eta_p = \frac{V_{p_a}}{E_0}.$$

Here, D is a $W \times W$ matrix of the form (11). If we assume a periodic boundary condition in the transverse direction, corresponding to a cylinder geometry instead of a ribbon, the matrix D is replaced by

$$T = \sum_{i=1}^{W-1} |i\rangle\langle i+1| + |W\rangle\langle 1| = D + |W\rangle\langle 1|. \quad (15)$$

The spectrum of $\mathcal{H}(k_1, k_3)$ is flat in the direction of k_3 and there are two completely flat bands,

$$E_{1,2}(k_1) = \tfrac{1}{2}[\eta_p + \eta_s \mp \sqrt{56 + (\eta_p - \eta_s)^2 - 8\cos k_1}],$$
$$E_3 = E_4 = \eta_p. \quad (16)$$

According to our knowledge the Hamiltonian $\mathcal{H}(k_1, k_3)$ is topologically trivial in all classifications. Nevertheless, we find end states, evolving from the dispersive states $|E_1(k_1)\rangle$ and $|E_2(k_1)\rangle$, when the system is finite along the k_1 direction. The end states are localized on one end of the system and they can be constructed analytically using the non-Bloch wave ansatz described in Ref. [22] (see Appendix D). The charge density of the end states has a decay length

$$\xi = \frac{1}{2\ln 3}, \quad (17)$$

and the energies of the end states are given by

$$E_{1,2}(-i\ln 3) = \frac{1}{2}\left(\eta_p + \eta_s \mp \sqrt{\frac{128}{3} + (\eta_p - \eta_s)^2}\right). \quad (18)$$

Importantly, we obtain these end states with the same energies $E_{1(2)}$ and localization length ξ for all values of k_3 so that the number of end modes is proportional to the width W of the ribbon. The existence of the end modes depends on the lattice termination, so that with the termination used in Appendix D all of the end modes are localized at the right end of the system.

The non-Bloch wave ansatz [22] tells us that there cannot be end states evolving from the flat bands E_3 and E_4, because the energies generically must be of the form $E_n(q)$ with some complex q, so that the flat bands cannot give rise to a state of energy different than η_p. However, the flat bands can still lead to a charge accumulation at the ends of the system due to the Zak phase [20]. Typically, such a kind of quantum geometric effect on the charge accumulation is small because the Zak phase is only defined modulo 2π but we find that in our system the accumulated charge scales with the width W of the ribbon because of an additional symmetry of the system.

Namely, we can transform the ribbon Hamiltonian (14) [and the cylinder Hamiltonian with periodic boundary conditions (15)] as

$$\mathcal{H}^{1D}(k_1) \to \mathcal{U}^\dagger \mathcal{H}^{1D}(k_1)\mathcal{U}, \quad \mathcal{U} = \mathbb{1}_W \otimes U, \quad (19)$$

where

$$U = \begin{pmatrix} 0 & 0 & 0 & 1 \\ \frac{\cos\frac{k_1}{2}}{\sqrt{3-\cos k_1}} & \frac{1}{\sqrt{2}} & \frac{-i\sin\frac{k_1}{2}e^{-i\frac{k_1}{2}}}{\sqrt{\frac{3-\cos k_1}{2}}} & 0 \\ \frac{-\cos\frac{k_1}{2}}{\sqrt{3-\cos k_1}} & \frac{1}{\sqrt{2}} & \frac{i\sin\frac{k_1}{2}e^{-i\frac{k_1}{2}}}{\sqrt{\frac{3-\cos k_1}{2}}} & 0 \\ \frac{2i\sin\frac{k_1}{2}}{\sqrt{3-\cos k_1}} & 0 & \frac{-\cos\frac{k_1}{2}e^{-i\frac{k_1}{2}}}{\sqrt{\frac{3-\cos k_1}{2}}} & 0 \end{pmatrix}, \quad (20)$$

leading to W identical 1×1 blocks,
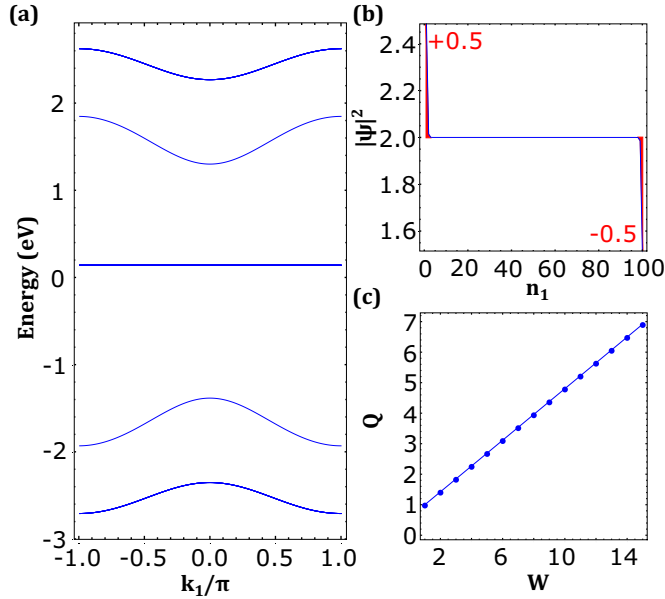
$$B_1 = E_0(\eta_p), \quad (21)$$

FIG. 7. (a) Band structure of minimal model ribbon of width $W = 8$ unit cells in the $\mathbf{n}_3$ direction. The flat bands have a degeneracy 16, whereas the highest and lowest dispersive bands $E_{1,2}(k_1)$ are sevenfold degenerate and the other dispersive bands $E_{\parallel 1,2}(k_1)$ are nondegenerate. (b) LDOS of flat bands for a single zigzag chain of length $L = 100$ unit cells as a function of position $\mathbf{n}_1$ with the accumulated charge quantized at both ends. (c) Accumulated charge as a function of thickness W along the $\mathbf{n}_3$ direction. We have used $V_{sc} = -1.5535$, $V_{pa} = -1.1909$, $V_{scp_a} = 1.1517$, $E_f = -1.330\,27$ (in meV) corresponding to HgS.

$W - 1$ identical 3×3 blocks,

$$B_3 = E_0 \begin{pmatrix} \eta_p & \sqrt{6 - 2\cos k_1} & 0 \\ \sqrt{6 - 2\cos k_1} & \eta_s & \sqrt{8} \\ 0 & \sqrt{8} & \eta_p \end{pmatrix}, \quad (22)$$

and one 3×3 block,

$$B_3' = E_0 \begin{pmatrix} \eta_p & \sqrt{6 - 2\cos k_1} & 0 \\ \sqrt{6 - 2\cos k_1} & \eta_s & c\sqrt{8} \\ 0 & c\sqrt{8} & \eta_p \end{pmatrix},$$

where $c = 0$ ($c = 1$) for the ribbon (cylinder) geometry. A schematic view of how the different states, represented by the columns of matrix U, contribute to each block is shown in Fig. 1(b). Each of the B_3 blocks contains one flat band with energy η_p and two bands with energies $E_{1,2}(k_1)$ given in Eq. (16). In the cylinder geometry with $c = 1$, block B_3' is identical to B_3, but in the ribbon geometry with $c = 0$ the block B_3' contributes a flat band with energy η_p and two dispersive bands with energies

$$E_{\parallel 1,2}(k_1) = \tfrac{1}{2}[\eta_p + \eta_s \mp \sqrt{24 + (\eta_p - \eta_s)^2 - 8\cos k_1}]. \quad (23)$$

The energy bands of a ribbon with $c = 0$ are shown in Fig. 7(a). Every B_3 block and B_3' block with $c = 1$ contributes two end states with energies $E_{1,2}(-i\ln 3)$ if the system is opened in the k_1 direction, whereas B_3' with $c = 0$ contributes two end states with energies $E_{\parallel 1,2}(-i\ln 3)$.

Because of the block decomposition the accumulated charge at the end of the ribbon, when it is opened in the k_1 direction, is related to the sum of the Zak phases of the different blocks. From an explicit calculation, using the standard prescription

$$\gamma_p = \frac{1}{i} \int_0^{2\pi} \langle E_p(k) | \partial_k | E_p(k) \rangle \quad (24)$$

and the analytical form of the eigenvectors, we get that the Zak phases of the flat bands from the blocks $\{B_1, B_3, B_3'\}$ are

$$\gamma_1 = \pi, \quad \gamma_3 = -\frac{\pi}{\sqrt{3}}, \quad \gamma_3' = -c\frac{\pi}{\sqrt{3}}. \quad (25)$$

Thus, inspired by Ref. [20], we expect that the difference of the left and right boundary charges due to the geometric phases of the flat bands is

$$Q = \frac{1}{\pi}(W\gamma_1 + [W - 1]\gamma_3 + \gamma_3'). \quad (26)$$

Indeed, we numerically find that

$$Q = \begin{cases} \frac{1}{\sqrt{3}} + W\left(1 - \frac{1}{\sqrt{3}}\right), & c = 0, \\ W\left(1 - \frac{1}{\sqrt{3}}\right), & c = 1, \end{cases} \quad (27)$$

demonstrating that Eq. (26) correctly describes the accumulated boundary charge, which increases proportionally to the width W of the system [see Figs. 7(b) and 7(c)].

Note that the above considerations are valid also when we set $k_1 = \pi$ as a starting point and consider a 2D system in the k_2-k_3 plane leading to a 1D ribbon or cylinder Hamiltonian $\mathcal{H}^{1D}(k_2)$ analogous to Eq. (14). Despite both Hamiltonians being apparently quite different, we show in Appendix E that they are related by a unitary transformation in the case of cylinder geometry and differ only in block B_3' in the case of ribbon geometry. In the former case the end states and the number of flat bands are the same as for $\mathcal{H}^{1D}(k_1)$ whereas in the latter one the number of edge states (flat bands) is smaller by two (larger by two) because of the difference between B_3' blocks (see Appendix E).

IV. CONNECTION BETWEEN THE NONTOPOLOGICAL EDGE STATES AND THE FLAT BANDS IN THE MINIMAL MODEL

Next, we demonstrate that the nontopological edge states indeed originate from the flat bands of the minimal model by interpolating between the Hamiltonians and following the evolution of the edge states.

We first notice that similar nontopological edge states are obtained both in the full heterostructure of CdTe$_{10}$/HgS$_8$/CdTe$_{10}$ and in HgS$_8$ [Figs. 8(a) and 8(b)]. Indeed, by interpolating between coupled $x = 0$ and uncoupled $x = 1$ systems of HgS$_8$ and CdTe$_{10}$, as described in Eq. (9), we find that the majority of the edge states at the high-symmetry point $k_1 = \pi$ remains unchanged throughout the evolution [Fig. 8(c)], despite the fact that the coupling has a large impact on the bulk state energies. Moreover, by studying the eigenvectors we conclude that the edge states are located in the HgS system. Therefore, we conclude that the CdTe barriers are not important for understanding the additional edge modes.
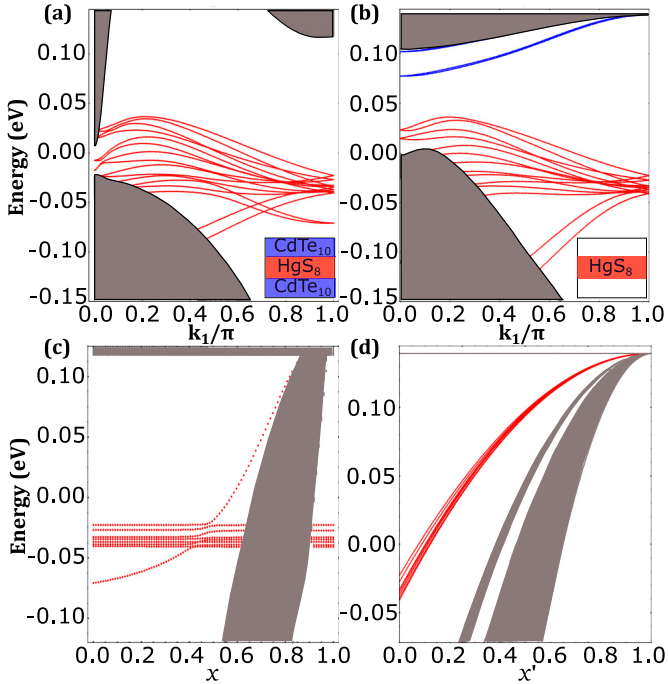
FIG. 8. (a), (b) Edge state spectra of $CdTe_{10}/HgS_8/CdTe_{10}$ and HgS_8 of width $W' = 300$ unit cells in the $\mathbf{n}_2$ direction, respectively. (c) Evolution of eigenenergies at $k_1 = \pi$ as a function of x interpolating between coupled ($x = 0$) and uncoupled ($x = 1$) systems of HgS_8 and $CdTe_{10}$ as described in Eq. (9). (d) Evolution of eigenenergies at $k_1 = \pi$ from HgS_8 ($x' = 0$) to the minimal model ($x' = 1$).

We can further trace back the origin of additional edge states from the HgS_8 system to the minimal model by interpolating the model parameters

$$\vec{P}(x') = (1 - x')\vec{P}_{HgS} + x'\vec{P}_{min} \tag{28}$$

between the HgS parameters

$$\vec{P}_{HgS} = \{V_{s_a}, V_{s_c} V_{p_a}, V_{p_c}, V_{ss\sigma},$$
$$\times V_{s_a p_c \sigma}, V_{s_c p_a \sigma}, V_{pp\sigma}, V_{pp\pi}, \lambda_a, \lambda_c, E_f\} \tag{29}$$

and the minimal model parameters

$$\vec{P}_{min} = \{V_{s_a}, V_{s_c}, V_{p_a}, V_{p_c}, 0, V_{s_c p_a \sigma}, V_{s_a p_c \sigma}, 0, 0, 0, 0, E_f\}. \tag{30}$$

By following the evolution of the edge states of HgS ($x' = 0$) to the minimal model ($x' = 1$) we find that the edge states are indeed connected to the flat bands of the minimal model [see Fig. 8(d)].

V. EFFECT OF EDGE POTENTIAL ON THE NONTOPOLOGICAL EDGE STATES

We have argued that the additional edge states are not topological. This suggests that it should be possible to remove them from the energy gap between the valence and conduction bands by applying an edge potential, for example, with the help of a side gate. In Fig. 9 we show the edge state spectra of $CdTe_{10}/HgS_8/CdTe_{10}$ in the presence of an additional on-site potential δ applied on the lattice sites at the right edge of the system. By decreasing the value of δ we find that all
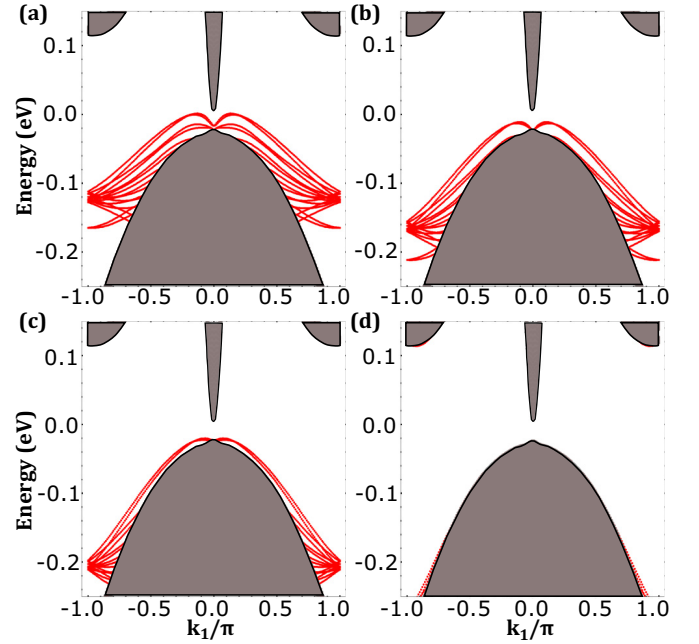

FIG. 9. Edge state spectra of $CdTe_{10}/HgS_8/CdTe_{10}$ of width $W' = 300$ unit cells with an on-site potential δ applied on the lattice sites at the right edge of the system. The values of the on-site potential are (a) $\delta = -0.1$ eV, (b) $\delta = -0.15$ eV, (c) $\delta = -0.2$ eV, and (d) $\delta = -0.3$ eV.

nontopological edge states can indeed be removed from the bulk gap.

VI. CONCLUSIONS

We have shown that HgTe/CdTe, HgS/CdTe, and InAs/GaSb heterostructures support additional edge states which are sensitive to edge termination, and we have traced the microscopic origin of these states back to a minimal model supporting flat bands with a nontrivial quantum geometry that gives rise to polarization charges at the edges. Moreover, we expect that additional edge states appear each time the edge cuts the s-p chains of the minimal model. Nontopological edge states have been observed in quantum spin Hall insulator candidate materials deteriorating the quality of the quantum spin Hall effect. Importantly, our results suggest that these states can be removed from the bulk energy gap by modifying the edge potential, for example, with a side gate or chemical doping.

APPENDIX A: COMPUTATIONAL DETAILS OF THE DENSITY-FUNCTIONAL CALCULATIONS

We performed electronic structure calculations by using the VASP [23] package based on the plane-wave basis set and projector augmented-wave method [24]. A plane-wave energy cutoff of 250 eV has been used. We have performed the calculations using a $8 \times 8 \times 8$ k-point Monkhorst-Pack grid in the presence of SOC with 512 k points and in the absence of SOC with 176 k points in the independent Brillouin zone. For the treatment of exchange correlation, the modified Becke-Johnson exchange potential together with a local density approximation for the correlation potential scheme [25,26] have been considered. In particular, we have an improvement in the band gap [27], and consequently an improvement in the spin-orbit splitting close to the gap. Similar settings for the DFT calculations were used to describe HgTe and InAs [28,29].

After obtaining the Bloch wave functions $\psi_{n,\mathbf{k}}$, the Wannier functions [30,31] are built up using the WANNIER90 code [32]. To extract the low-energy properties of the electronic bands, we have used the Slater-Koster interpolation scheme to obtain a long-range tight-binding model with the Wannier function method [32]. To obtain the first-neighbor tight-binding model, we require the tight-binding model to fit the DFT band structure at the high-symmetry points Γ, X, and L. Regarding the spin orbit, we extracted the effective SOC of the anion λ_a from the formula $3\lambda_a = E(\Gamma_8) - E(\Gamma_7)$, where Γ_8 and Γ_7 anion energy levels were obtained from first-principles calculations [33], and the same was done for the cation λ_c. Note that in Ref. [33] we used a different notation where $\frac{3\lambda_a}{2} = E(\Gamma_8) - E(\Gamma_7)$. Following this procedure, we obtained the hopping parameters, the on-site energies, and the spin-orbit constants. The experimental lattice constants, which coincide with those used in our DFT calculation except for HgS, are reported in Table II. For HgS we have used a larger lattice constant $a_0 = 6.835$ Å to obtain that the effective SOC is close to zero.

We demonstrate why the effective spin-orbit λ_a is negative for the p state of S in HgS [36]. First, we consider a Hamiltonian containing the Hg d states and anion p states with the respective bare SOC defined $\lambda_{\text{Hg-}d}^{\text{bare}}$ and λ_a^{bare} and we diagonalize the Hamiltonian to calculate the effective spin

orbit $\lambda_a \propto E(\Gamma_8) - E(\Gamma_7)$ as a function of the bare parameters. We define the difference between the on-site energies $\Delta\epsilon_1 = V_{pa} - V_{dc} > 0$. We calculate the eigenvalues of the Hamiltonian at the Γ point. In order to evaluate analytically the effective SOC, we perform the Löwdin approximation projecting on the anion subspace, obtaining

$$\lambda_a \approx \lambda_a^{\text{bare}} - \frac{H_{p_xa,d_{yz}c}^2 \lambda_{\text{Hg-}d}^{\text{bare}}}{\left(\Delta\epsilon_1 - \frac{3}{2}\lambda_{\text{Hg-}d}^{\text{bare}}\right)\left(\Delta\epsilon_1 + \lambda_{\text{Hg-}d}^{\text{bare}}\right)}, \quad (A1)$$

where $H_{p_xa,d_{yz}c}$ is the matrix element that connects the p_x-a and d_{yz}-c orbitals calculated at the Γ point. If we consider the conditions $|\Delta\epsilon_1| \gg \lambda_{\text{Hg-}d}^{\text{bare}}$, we obtain

$$\lambda_a \approx \lambda_a^{\text{bare}} - \left(\frac{H_{p_xa,d_{yz}c}}{\Delta\epsilon_1}\right)^2 \lambda_{\text{Hg-}d^{\text{bare}}}. \quad (A2)$$

We can observe that the leading correction term to the bare spin orbit is always negative. The validity of this formula is restricted to the region close to the Γ point, however, that is the interesting region for this class of compounds. This correction to the bare SOC is present in the entire HgX ($X = $ S, Se, Te) family, however, it is quantitatively more relevant in HgS.

APPENDIX B: DANGLING BONDS IN DENSITY-FUNCTIONAL CALCULATIONS

Here, we will show how to handle the dangling bonds using density-functional theory in this material class. To do that, we will consider the CdTe$_4$/HgTe$_9$/CdTe$_4$ case that is the most difficult to treat due to the large size of the constituent atoms. Figure 10(a) shows the 2D QW with unsaturated dangling bonds of the anion on top (Te terminated) and the cation on the bottom (Cd terminated). The band structure of the unsaturated crystal structure is shown in Fig. 11(a). We observe a metallic phase due to unsaturated edge states not related to the topology. Due to the large size of Cd and Te atoms, the saturation of the dangling bond with hydrogen atoms does not yield a good effect. To overcome this the dangling bonds of the anions are saturated with sodium atoms and cations are saturated with iodine atoms, as shown in Fig. 10(b). When we saturate the dangling bonds, we recover the band structure of the topological insulator as shown in Fig. 11(b). The 2D QW with these dangling bonds is an insulator by nature with the band inverted at the Γ point if the thickness of HgTe is sufficiently large. After considering the dangling bonds, the tight-binding model gives a satisfactory description of the electronic properties of the system. This saturation refers to the (001) top and bottom surface of the heterostructure and is expected to work similarly for other surfaces.

Additionally, the adatoms could aggregate [37]. Further investigations are needed to establish the results for this case. The necessity to use large unit cells, SOC, and an exchange functional for strongly correlated electrons makes these calculations for adatoms in HgTe quite challenging. Recent results were performed for magnetic bulk impurities in HgTe [33,38],

TABLE II. Experimental lattice constant at 8 K for HgTe and at 300 K for HgS, CdTe, at 0 K extrapolation for InAs, GaSb, and AlSb. All the values are in Å.

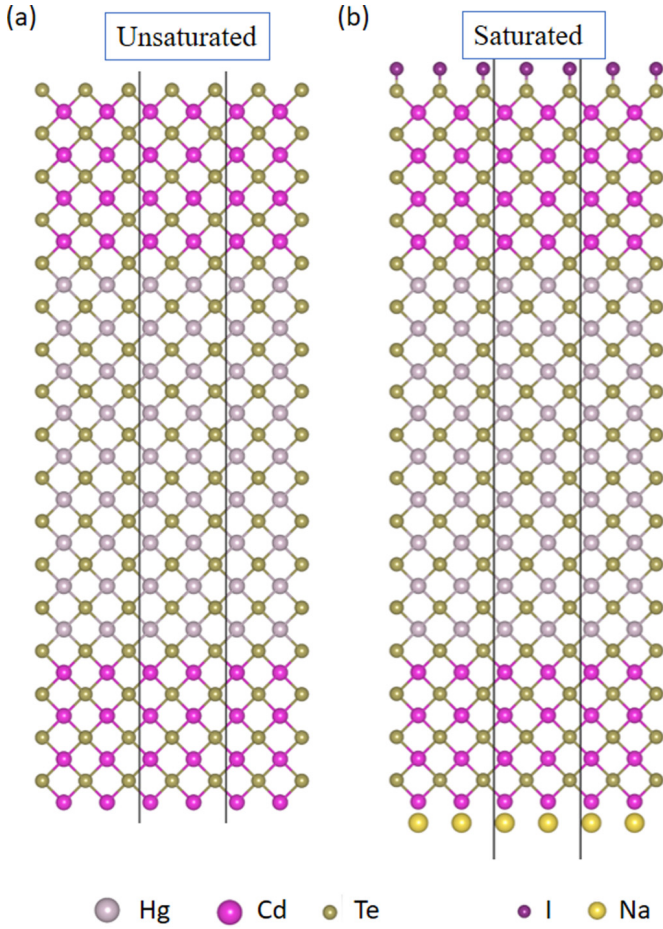|	HgTe [34]	HgS [34]	CdTe [34]	InAs [35]	GaSb [35]	AlSb [35]
a_0	6.460	5.851	6.480	6.050	6.082	6.128

(a) Unsaturated   (b) Saturated

FIG. 10. Crystal structure of the 2D QWs grown along the (001) orientation with (a) unsaturated dangling bonds on the top and bottom surface with stoichiometric concentration. (b) Dangling bond saturated with I and Na on the anion and cation surfaces, respectively.

APPENDIX C: HETEROSTRUCTURES GROWN IN THE (110) DIRECTION

In the main text we have studied heterostructures grown along the direction of the lattice vector $\mathbf{n}_3$. This means that the top and the bottom surfaces are perpendicular to the (001) direction and the side surfaces (edges) are perpendicular to the
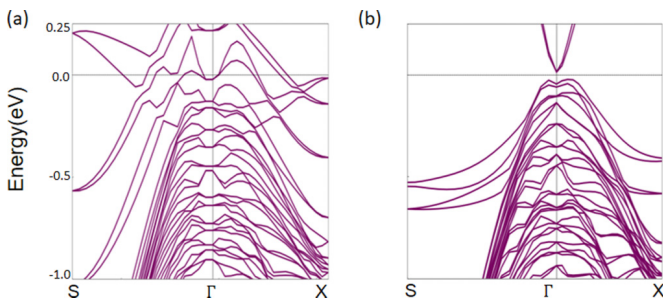

FIG. 11. Band structure of the 2D QWs with (a) unsaturated dangling bonds on the top and bottom surface. (b) Dangling bond saturated with I and Na on the anion and cation surface, respectively. After saturation the DFT band structure resembles the tight-binding Hamiltonian band structure.
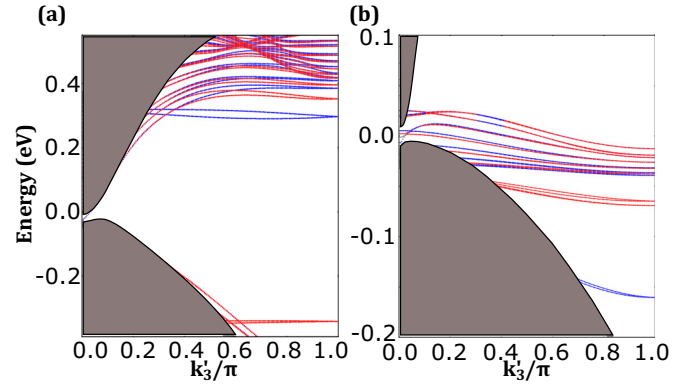

FIG. 12. Edge state spectra for heterostructures grown in the (110) direction: (a) $CdTe_{10}/HgTe_{16}/CdTe_{10}$ and (b) $CdTe_{10}/HgS_8/CdTe_{10}$. The widths are $W' = 150$ unit cells in the $\mathbf{n}'_2$ direction.

($11\bar{1}$) and ($1\bar{1}1$) directions. However, another typical growth direction of heterostructures is (110). Therefore in this Appendix we check how the results change when we consider this growth direction instead of the one considered in the main text. To address this issue we consider our tight-binding model with the unit cell doubled along the $\mathbf{n}_3$ direction and the new translation vectors being $\mathbf{n}'_1 = (1, -1, 0)$, $\mathbf{n}'_2 = (1, 1, 0)$, and $\mathbf{n}'_3 = (0, 0, 2)$. The layers of the heterostructure are now stacked along $\mathbf{n}'_1$ given the top and bottom surfaces as perpendicular to the (110) direction and the side surfaces or edges perpendicular to the (001) and ($1\bar{1}0$) directions.

For these new heterostructures we again construct 2D Hamiltonians $\mathcal{H}^{2D}(k'_2, k'_3)$, as in Eq. (5), for which we consider open-edge versions $\mathcal{H}^{1D}(k'_3)$, as in Eq. (10), to verify the presence of the additional edge states at the ($1\bar{1}0$) surface of the system. As previously, we define W' as a width of the 1D ribbon described by $\mathcal{H}^{1D}_{k'_3}$. As we can see from the spectra shown in Fig. 12, we still find additional edge states in the HgTe/CdTe and HgS/CdTe heterostructure. Additional edge states of CdTe/HgTe/CdTe lie outside the band gap, whereas for the CdTe/HgS/CdTe heterostructure they appear inside the gap and there is an equal number of them on both edges, in contrast to the cases discussed in the main text.

APPENDIX D: ANALYTICAL DERIVATION OF THE END STATE ENERGIES AND WAVE FUNCTIONS

In this Appendix we calculate the eigenenergies and the wave functions for the end states of the minimal model Hamiltonian (13), when the system has a finite length L along the k_1 direction. By using the Fourier decomposition

$$\mathcal{H}(k_1, k_3) = H_0(k_3) + e^{ik_1}H_1(k_3) + e^{-ik_1}H_1^\dagger(k_3), \quad \text{(D1)}$$

the Hamiltonian for the system can be written as

$$\mathcal{H}^{1D}(k_3) = \mathbb{1}_L \otimes H_0(k_3) + D \otimes H_1(k_3) + D^\mathsf{T} \otimes H_1^\dagger(k_3), \quad \text{(D2)}$$

where D is the $L \times L$ matrix of the form (11). The eigenstates $|\psi\rangle = \sum_{j=1}^{L} |j\rangle \otimes |\phi_j\rangle$, where $|j\rangle$ is the basis state describing the jth unit cell along the k_1 direction and $|\phi_j\rangle$ is the spinor

describing the state within the unit cell, must satisfy

$$H_1^\dagger(k_3)|\phi_{j-1}\rangle + H_0(k_3)|\phi_j\rangle + H_1(k_3)|\phi_{j+1}\rangle = E|\phi_j\rangle, \quad \text{(D3)}$$

for $j = 2, 3, \ldots, L-1$ and the boundary equations

$$H_0(k_3)|\phi_1\rangle + H_1(k_3)|\phi_2\rangle = E|\phi_1\rangle,$$
$$H_1^\dagger(k_3)|\phi_{L-1}\rangle + H_0(k_3)|\phi_L\rangle = E|\phi_L\rangle. \quad \text{(D4)}$$

We write an ansatz for the end states ($n = 1, 2$) as

$$|\phi_{n,j}(q)\rangle = A_q e^{ijq}|E_n(q)\rangle + B_q e^{-ijq}|E_n(-q)\rangle,$$

where the energies

$$E_{1(2)}(q) = \tfrac{1}{2}[\eta_p + \eta_s \mp \sqrt{56 + (\eta_p - \eta_s)^2 - 8\cos q}]. \quad \text{(D5)}$$

and spinors $|E_{1(2)}(q)\rangle$ are obtained from the dispersive bulk states by replacing the momentum k_1 with q. Therefore, the ansatz automatically satisfies Eq. (D3). Importantly, here q is an imaginary number so that the ansatz describes a state localized at the end of the system. Note that $|\phi_{n,j}(q)\rangle$ also contains dependence on k_3 which is however not essential here. Using the boundary conditions we find in the thermodynamic limit $L \to \infty$ for both $n = 1, 2$ and any k_3 that $q = -i\ln 3$ so that the charge density has a decay length

$$\xi = \frac{1}{2\log 3}. \quad \text{(D6)}$$

All end states localized at the right end of the system, and their energies are

$$E_{1(2)}(-i\ln 3) = \frac{1}{2}\left(\eta_p + \eta_s \mp \sqrt{\frac{128}{3} + (\eta_p - \eta_s)^2}\right). \quad \text{(D7)}$$

APPENDIX E: k_1-k_2 DUALITY OF THE MINIMAL MODEL

Consider the minimal model obtained as in Sec. III. Now, instead of setting $k_2 = \pi$ we take $k_1 = \pi$. The 2D bulk Hamiltonian of this system is

$$\tilde{\mathcal{H}}^{2D}(k_2, k_3) = \tilde{H}_\parallel + [e^{ik_3}\tilde{H}_\perp(k_2) + \text{H.c.}], \quad \text{(E1)}$$

and its spectrum does not depend again on k_3. The 1D Hamiltonian of the W unit cell wide cylinder ($c = 1$) is

$$\tilde{\mathcal{H}}^{1D}_{c=1}(k_2) = \mathbb{1}_W \otimes \tilde{H}_\parallel + [T \otimes \tilde{H}_\perp(k_2) + \text{H.c.}], \quad \text{(E2)}$$

which we will compare to the previous case of the $k_2 = \pi$ Hamiltonian,

$$\mathcal{H}^{1D}_{c=1}(k_1) = \mathbb{1}_W \otimes H_\parallel(k_1) + (T \otimes H_\perp + \text{H.c.}). \quad \text{(E3)}$$

Here, T is defined by Eq. (15), $H_\parallel(k_1)$ and $H_\perp$ are defined in Sec. III, and

$$\frac{\tilde{H}_\parallel}{E_0} = \begin{pmatrix} \eta_s & -2 & 2 & 0 \\ -2 & \eta_p & 0 & 0 \\ 2 & 0 & \eta_p & 0 \\ 0 & 0 & 0 & \eta_p \end{pmatrix}, \quad \text{(E4)}$$

and

$$\frac{\tilde{H}_\perp(k_2)}{E_0} = \begin{pmatrix} 0 & -e^{-ik_2}+1 & -e^{-ik_2}+1 & e^{-ik_2}+1 \\ 0 & 0 & 0 & 0 \\ 0 & 0 & 0 & 0 \\ 0 & 0 & 0 & 0 \end{pmatrix}. \quad \text{(E5)}$$

By a close inspection of the 1D chains described by the Hamiltonians (E2) and (E3) we find a duality relation between these two Hamiltonians given by

$$\mathcal{H}^{1D}_{c=1}(k_1) = \mathcal{V}^\dagger \tilde{\mathcal{H}}^{1D}_{c=1}(k_2 = -k_1)\mathcal{V}, \quad \text{(E6)}$$

where $\mathcal{V}$ is a unitary operator,

$$\mathcal{V} = \begin{cases} P_3 P_2 P_1 GQ, & W \in 2\mathbb{N}+1, \\ P_3 P_2 P_1 G, & W \in 2\mathbb{N}. \end{cases} \quad \text{(E7)}$$

Here, $P_{1,2,3}$ are the site permutations,

$$P_1 = \mathbb{1}_W \otimes \begin{pmatrix} 0 & 1 & 0 & 0 \\ 0 & 0 & 1 & 0 \\ 0 & 0 & 0 & 1 \\ 1 & 0 & 0 & 0 \end{pmatrix}, \quad \text{(E8)}$$

$$P_2 = \begin{pmatrix} 0 & \cdots & 0 & 0 & 0 & 1 & 0 \\ 0 & \cdots & 0 & 0 & 1 & 0 & 0 \\ 0 & \cdots & 0 & 1 & 0 & 0 & 0 \\ \vdots & \vdots & \vdots & \vdots & \vdots & \vdots & \vdots \\ 0 & 1 & 0 & 0 & \cdots & 0 & 0 \\ 1 & 0 & 0 & 0 & \cdots & 0 & 0 \\ 0 & 0 & 0 & 0 & \cdots & 0 & 1 \end{pmatrix}, \quad \text{(E9)}$$

and

$$P_3 = \mathbb{1}_W \otimes \begin{pmatrix} 0 & 0 & 0 & 1 \\ 0 & 1 & 0 & 0 \\ 0 & 0 & 1 & 0 \\ 1 & 0 & 0 & 0 \end{pmatrix}. \quad \text{(E10)}$$

Note that P_1 and P_3 only reshuffle sites inside the unit cell consisting of four sites whereas the order of the unit cells remains unchanged. On the other hand, the P_2 operator reverts the whole chain and shifts sites by one in a cyclic manner. The remaining constituents of $\mathcal{V}$ are the alternating gauge matrix,

$$G = \begin{pmatrix} 1 & 0 & 0 & 0 & \cdots \\ 0 & -1 & 0 & 0 & \\ 0 & 0 & 1 & 0 & \\ 0 & 0 & 0 & -1 & \\ \vdots & & & & \ddots \end{pmatrix} \otimes \begin{pmatrix} 1 & 0 & 0 & 0 \\ 0 & -1 & 0 & 0 \\ 0 & 0 & 1 & 0 \\ 0 & 0 & 0 & -1 \end{pmatrix}, \quad \text{(E11)}$$

and operator Q acting on the first unit cell,

$$Q = \begin{pmatrix} 1 & 0 & 0 & \cdots & 0 \\ 0 & 0 & 0 & \cdots & 0 \\ 0 & 0 & 0 & \cdots & 0 \\ \vdots & \vdots & \vdots & \vdots & \vdots \\ 0 & 0 & 0 & \cdots & 0 \end{pmatrix} \otimes \begin{pmatrix} 1 & 0 & 0 & 0 \\ 0 & 0 & -1 & 0 \\ 0 & -1 & 0 & 0 \\ 0 & 0 & 0 & 1 \end{pmatrix}$$
$$+ \begin{pmatrix} 0 & 0 & 0 & 0 & \cdots & 0 \\ 0 & 1 & 0 & 0 & \cdots & 0 \\ 0 & 0 & 1 & 0 & \cdots & 0 \\ \vdots & \vdots & \vdots & \vdots & \vdots & \vdots \\ 0 & 0 & \cdots & 0 & 1 & 0 \\ 0 & 0 & 0 & \cdots & 0 & 1 \end{pmatrix} \otimes \mathbb{1}_4. \quad \text{(E12)}$$

From Eq. (E6) and the results of Sec. III it follows that for a cylindrical geometry along k_3 the $\tilde{\mathcal{H}}^{1D}_{c=1}(k_2)$ Hamiltonian splits into W identical 1×1 blocks,

$$\tilde{B}_1 = E_0(\eta_p), \quad \text{(E13)}$$

and another W identical 3×3 blocks,

$$
\tilde{B}_3 = E_0 \begin{pmatrix} \eta_p & \sqrt{6 - 2\cos k_2} & 0 \\ \sqrt{6 - 2\cos k_2} & \eta_s & \sqrt{8} \\ 0 & \sqrt{8} & \eta_p \end{pmatrix},
$$
(E14)

under transformation $\mathcal{W} = V\,U$. The same transformation $\mathcal{W}$ used on a ribbon-geometry $(c = 0)$ Hamiltonian

$$
\mathcal{H}^{1\mathrm{D}}_{c=0}(k_2) = \mathbb{1}_W \otimes \tilde{H}_\parallel + [D \otimes \tilde{H}_\perp(k_2) + \mathrm{H.c.}],
$$
(E15)

with D defined by Eq. (11) gives almost the same block structure with one of the 3×3 blocks substituted by

$$
\tilde{B}'_3 = E_0 \begin{pmatrix} \eta_p & 0 & 0 \\ 0 & \eta_s & \sqrt{8} \\ 0 & \sqrt{8} & \eta_p \end{pmatrix}.
$$
(E16)

Concluding, we have found that for cylindrical geometry the Hamiltonians $\mathcal{H}^{1\mathrm{D}}_{c=1}(k_1)$ and $\mathcal{H}^{1\mathrm{D}}_{c=1}(k_2)$ have the same band structures and the same end states. In the case of the ribbon geometry $\mathcal{H}^{1\mathrm{D}}_{c=0}(k_2)$ has two more (less) flat (dispersive) bands compared to $\mathcal{H}^{1\mathrm{D}}_{c=0}(k_1)$, following from the difference between blocks $\tilde{B}'_3$ and $\tilde{B}'_3$. The number of end states in this case is smaller by two because the $\tilde{B}'_3$ having no dispersion cannot contribute any, unlike B'_3.

[1] M. Z. Hasan and C. L. Kane, Colloquium: Topological insulators, Rev. Mod. Phys. **82**, 3045 (2010).

[2] X.-L. Qi and S.-C. Zhang, Topological insulators and superconductors, Rev. Mod. Phys. **83**, 1057 (2011).

[3] B. A. Bernevig, T. L. Hughes, and S.-C. Zhang, Quantum spin Hall effect and topological phase transition in HgTe quantum wells, Science **314**, 1757 (2006).

[4] C. Liu, T. L. Hughes, X.-L. Qi, K. Wang, and S.-C. Zhang, Quantum Spin Hall Effect in Inverted Type-II Semiconductors, Phys. Rev. Lett. **100**, 236601 (2008).

[5] M. König, S. Wiedmann, C. Brüne, A. Roth, H. Buhmann, L. W. Molenkamp, X.-L. Qi, and S.-C. Zhang, Quantum spin Hall insulator state in HgTe quantum wells, Science **318**, 766 (2007).

[6] L. Du, I. Knez, G. Sullivan, and R.-R. Du, Robust Helical Edge Transport in Gated InAs/GaSb Bilayers, Phys. Rev. Lett. **114**, 096802 (2015).

[7] S. Wu, V. Fatemi, Q. D. Gibson, K. Watanabe, T. Taniguchi, R. J. Cava, and P. Jarillo-Herrero, Observation of the quantum spin Hall effect up to 100 kelvin in a monolayer crystal, Science **359**, 76 (2018).

[8] L. Lunczer, P. Leubner, M. Endres, V. L. Müller, C. Brüne, H. Buhmann, and L. W. Molenkamp, Approaching Quantization in Macroscopic Quantum Spin Hall Devices through Gate Training, Phys. Rev. Lett. **123**, 047701 (2019).

[9] Y. Tanaka, A. Furusaki, and K. A. Matveev, Conductance of a Helical Edge Liquid Coupled to a Magnetic Impurity, Phys. Rev. Lett. **106**, 236402 (2011).

[10] J. C. Budich, F. Dolcini, P. Recher, and B. Trauzettel, Phonon-Induced Backscattering in Helical Edge States, Phys. Rev. Lett. **108**, 086602 (2012).

[11] A. M. Lunde and G. Platero, Helical edge states coupled to a spin bath: Current-induced magnetization, Phys. Rev. B **86**, 035112 (2012).

[12] A. Del Maestro, T. Hyart, and B. Rosenow, Backscattering between helical edge states via dynamic nuclear polarization, Phys. Rev. B **87**, 165440 (2013).

[13] D. I. Pikulin and T. Hyart, Interplay of Exciton Condensation and the Quantum Spin Hall Effect in InAs/GaSb Bilayers, Phys. Rev. Lett. **112**, 176403 (2014).

[14] T. Paul, V. Fernández Becerra, and T. Hyart, Interplay of quantum spin Hall effect and spontaneous time-reversal symmetry breaking in electron-hole bilayers. I. Transport properties, Phys. Rev. B **106**, 235420 (2022).

[15] J. I. Väyrynen, M. Goldstein, Y. Gefen, and L. I. Glazman, Resistance of helical edges formed in a semiconductor heterostructure, Phys. Rev. B **90**, 115309 (2014).

[16] T. Dietl, Charge dopants control quantum spin Hall materials, arXiv:2206.01613.

[17] G. Dolcetto, M. Sassetti, and T. L. Schmidt, Edge physics in two-dimensional topological insulators, Riv. Nuovo Cimento **39**, 113 (2016).

[18] F. Nichele, H. J. Suominen, M. Kjaergaard, C. M. Marcus, E. Sajadi, J. A. Folk, F. Qu, A. J. A. Beukman, F. K. de Vries, J. van Veen, S. Nadj-Perge, L. P. Kouwenhoven, B.-M. Nguyen, A. A. Kiselev, W. Yi, M. Sokolich, M. J. Manfra, E. M. Spanton, and K. A. Moler, Edge transport in the trivial phase of InAs/GaSb, New J. Phys. **18**, 083005 (2016).

[19] M. C. Dartiailh, S. Hartinger, A. Gourmelon, K. Bendias, H. Bartolomei, H. Kamata, J.-M. Berroir, G. Fève, B. Plaçais, L. Lunczer, R. Schlereth, H. Buhmann, L. W. Molenkamp, and E. Bocquillon, Dynamical Separation of Bulk and Edge Transport in HgTe-Based 2D Topological Insulators, Phys. Rev. Lett. **124**, 076802 (2020).

[20] J.-W. Rhim, J. Behrends, and J. H. Bardarson, Bulk-boundary correspondence from the intercellular Zak phase, Phys. Rev. B **95**, 035421 (2017).

[21] W.-K. Lou, W. Yang, and K. Chang, Helical conducting edge states in narrow-gap semiconductors without band inversion, Phys. Rev. B **105**, 045305 (2022).

[22] K. Yokomizo and S. Murakami, Non-Bloch Band Theory of Non-Hermitian Systems, Phys. Rev. Lett. **123**, 066404 (2019).

[23] G. Kresse and J. Furthmüller, Efficiency of ab-initio total energy calculations for metals and semiconductors using a plane-wave basis set, Comput. Mater. Sci. **6**, 15 (1996).

[24] G. Kresse and D. Joubert, From ultrasoft pseudopotentials to the projector augmented-wave method, Phys. Rev. B **59**, 1758 (1999).

[25] A. D. Beckea and E. R. Johnson, A simple effective potential for exchange, J. Chem. Phys. **124**, 221101 (2006).

[26] F. Tran and P. Blaha, Accurate Band Gaps of Semiconductors and Insulators with a Semilocal Exchange-Correlation Potential, Phys. Rev. Lett. **102**, 226401 (2009).

[27] J. A. Camargo-Martínez and R. Baquero, Performance of the modified Becke-Johnson potential for semiconductors, Phys. Rev. B **86**, 195106 (2012).

[28] R. Islam, B. Ghosh, G. Cuono, A. Lau, W. Brzezicki, A. Bansil, A. Agarwal, B. Singh, T. Dietl, and C. Autieri, Topological states in superlattices of HgTe class of materials for engineering three-dimensional flat bands, Phys. Rev. Res. **4**, 023114 (2022).

[29] G. Hussain, G. Cuono, R. Islam, A. Trajnerowicz, J. Jureńczyk, C. Autieri, and T. Dietl, Electronic and optical properties of $InAs/InAs_{0.625}Sb_{0.375}$ superlattices and their application to far-infrared detectors, J. Phys. D **55**, 495301 (2022).

[30] N. Marzari and D. Vanderbilt, Maximally localized generalized Wannier functions for composite energy bands, Phys. Rev. B **56**, 12847 (1997).

[31] I. Souza, N. Marzari, and D. Vanderbilt, Maximally localized Wannier functions for entangled energy bands, Phys. Rev. B **65**, 035109 (2001).

[32] A. A. Mostofi, J. R. Yates, Y. S. Lee, I. Souza, D. Vanderbilt, and N. Marzari, WANNIER90: A tool for obtaining maximally-localised Wannier functions, Comput. Phys. Commun. **178**, 685 (2008).

[33] C. Autieri, C. Śliwa, R. Islam, G. Cuono, and T. Dietl, Momentum-resolved spin splitting in mn-doped trivial CdTe and topological HgTe semiconductors, Phys. Rev. B **103**, 115209 (2021).

[34] *Physics of Group II-IV Elements and I-VII Compounds*, edited by O. Madelung, M. Schulz, and H. Weiss, Landolt-Börnstein, New Series, Group III, Vol. 17,Pt. B (Springer, Berlin, 1982).

[35] I. Vurgaftman, J. R. Meyer, and L. R. Ram-Mohan, Band parameters for III-V compound semiconductors and their alloys, J. Appl. Phys. **89**, 5815 (2001).

[36] Q.-Z. Wang, S.-C. Wu, C. Felser, B. Yan, and C.-X. Liu, Spin texture and mirror Chern number in Hg-based chalcogenides, Phys. Rev. B **91**, 165435 (2015).

[37] N. Gonzalez Szwacki, J. A. Majewski, and T. Dietl, Aggregation and magnetism of Cr, Mn, and Fe cations in GaN, Phys. Rev. B **83**, 184417 (2011).

[38] C. Śliwa, C. Autieri, J. A. Majewski, and T. Dietl, Superexchange dominates in magnetic topological insulators, Phys. Rev. B **104**, L220404 (2021).

Conclusions and perspectives

Summary of Main Results

The research expounded in this thesis is aimed at unraveling insights into the intricate realm of topological and non-topological boundary states within SnTe nanowires and quantum spin Hall candidates, including materials like HgTe, HgS, InAs, and GaSb. Our principal findings can be succinctly summarized as follows:

- SnTe materials exhibit robust corner states and hinge states in the normal state. The topological nature of these states is connected to the approximate symmetries inherent in SnTe nanowires.

- Nontrivial crystalline insulator and higher-order topologies can manifest either independently or jointly, as the higher-order topological invariant governing hinge states does not directly correlate with the topological crystalline insulator invariant.

- For realistic nanowire thicknesses, our theoretical study demonstrates that experimentally achievable Zeeman field strengths can lead to topological nontrivial phases.

- We have made the significant discovery that superconducting SnTe nanowires can host gapless bulk Majorana modes when inversion symmetry is present. The introduction of an inversion-symmetry-breaking field leads to the gapping of these bulk Majorana modes, and the nanowires would support topologically protected Majorana zero modes localized at the ends of the wire.

- On the other hand, quantum spin Hall insulator candidate materials showcase additional edge states that are influenced by the edge termination, an aspect not yet explored in current literatures.

- The origin of these states can be traced back to a simple minimal model, which serves as a fundamental unit for constructing these heterostructures. This minimal model gives rise to flat bands characterized by nontrivial quantum geometry, resulting in polarization charges at the edges. When these flat bands interact with each other and other states, these polarization charges transform into the additional edge states that appear within the complete heterostructure.

- It has been determined that these supplementary edge states lack topological significance. Consequently, the application of an edge potential holds the potential to eliminate them from the energy gap.

The results of this thesis may contribute to the solution of some of the most important challenges in the field of topological materials:

- The analysis of the SnTe nanowires can guide the experiments probing corner states and hinge states, and they can open up new opportunities for controlling and creating Majorana zero modes by manipulating inversion-symmetry-breaking fields (e.g. via ferroelectricity).

- The analysis of non-topological edge states in quantum spin Hall insulators can suggest ways to eliminate them from the energy gap, improving the quantization of the edge conductance in the experiments.

Bibliography

(1) Altland, A. & Zirnbauer, M. R. *Phys. Rev. B* **1997**, *55*, 1142–1161.

(2) Altland, A. & Zirnbauer, M. R. *Phys. Rev. B* **1997**, *55*, 1142–1161.

(3) Asbóth, J. K.; Oroszlány, L., & Pályi, A., *A Short Course on Topological Insulators*, 2016; Vol. 919.

(4) Balakrishnan, G.; Bawden, L.; Cavendish, S., & Lees, M. R. *Phys. Rev. B* **2013**, *87*, 140507.

(5) Balakrishnan, G.; Bawden, L.; Cavendish, S., & Lees, M. R. *Phys. Rev. B* **2013**, *87*, 140507.

(6) Bernevig, B. A.; Hughes, T. L., & Zhang, S.-C. *Science* **2006**, *314*, 1757–1761.

(7) Bernevig, B. A.; Hughes, T. L., & Zhang, S.-C. *Science* **2006**, *314*, 1757–1761.

(8) Bliesener, A.; Feng, J.; Taskin, A. A., & Ando, Y. *Phys. Rev. Materials* **2019**, *3*, 101201.

(9) Bliesener, A.; Feng, J.; Taskin, A. A., & Ando, Y. *Phys. Rev. Mater.* **2019**, *3*, 101201.

(10) Brzezicki, W. & Hyart, T. *Phys. Rev. B* **2020**, *101*, 235113.

(11) Brzezicki, W.; Wysoki ński, M. M., & Hyart, T. *Phys. Rev. B* **2019**, *100*, 121107.

(12) Budich, J. C.; Dolcini, F.; Recher, P., & Trauzettel, B. *Phys. Rev. Lett.* **2012**, *108*, 086602.

(13) Chang, K.; Liu, J.; Lin, H.; Wang, N.; Zhao, K.; Zhang, A.; Jin, F.; Zhong, Y.; Hu, X.; Duan, W.; Zhang, Q.; Fu, L.; Xue, Q.-K.; Chen, X., & Ji, S.-H. *Science* **2016**, *353*, 274–278.

(14) Chiu, C.-K. & Schnyder, A. P. *Journal of Physics: Conference Series* **2015**, *603*, 012002.

(15) Chiu, C.-K. & Schnyder, A. P. *Phys. Rev. B* **2014**, *90*, 205136.

(16) Chiu, C.-K.; Teo, J. C. Y.; Schnyder, A. P., & Ryu, S. *Rev. Mod. Phys.* **2016**, *88*, 035005.

(17) Chiu, C.-K.; Yao, H., & Ryu, S. *Phys. Rev. B* **2013**, *88*, 075142.

(18) Dartiailh, M. C.; Hartinger, S.; Gourmelon, A.; Bendias, K.; Bartolomei, H.; Kamata, H.; Berroir, J.-M.; Fève, G.; Pla çais, B.; Lunczer, L.; Schlereth, R.; Buhmann, H.; Molenkamp, L. W., & Bocquillon, E. *Phys. Rev. Lett.* **2020**, *124*, 076802.

(19) Del Maestro, A.; Hyart, T., & Rosenow, B. *Phys. Rev. B* **2013**, *87*, 165440.

(20) Deng, S.; Viola, L., & Ortiz, G. *Phys. Rev. Lett.* **2012**, *108*, 036803.

(21) De Wolff, P. M.; Belov, N. V.; Bertaut, E. F.; Buerger, M. J.; Donnay, J. D. H.; Fischer, W.; Hahn, T.; Koptsik, V. A.; Mackay, A. L.; Wondratschek, H.; Wilson, A. J. C., & Abrahams, S. C. *Acta Crystallographica Section A* **1985**, *41*, 278–280.

(22) Dietl, T. Charge dopants control quantum spin Hall materials, 2022.

(23) Dolcetto, G.; Sassetti, M., & Schmidt, T. L. *La Rivista del Nuovo Cimento* **2016**, *39*, 113–154.

(24) Du, L.; Knez, I.; Sullivan, G., & Du, R.-R. *Phys. Rev. Lett.* **2015**, *114*, 096802.

(25) Dybko, K.; Szot, M.; Szczerbakow, A.; Gutowska, M. U.; Zajarniuk, T.; Domagala, J. Z.; Szewczyk, A.; Story, T., & Zawadzki, W. *Phys. Rev. B* **2017**, *96*, 205129.

(26) Dzero, M.; Sun, K.; Coleman, P., & Galitski, V. *Phys. Rev. B* **2012**, *85*, 045130.

(27) Dzero, M.; Sun, K.; Galitski, V., & Coleman, P. *Phys. Rev. Lett.* **2010**, *104*, 106408.

(28) Dziawa, P.; Kowalski, B. J.; Dybko, K.; Buczko, R.; Szczerbakow, A.; Szot, M.; Lusakowska, E.; Balasubramanian, T.; Wojek, B. M.; Berntsen, M. H.; Tjernberg, O., & Story, T. *Nature Materials* **2012**, *11*, 1023.

(29) Fang, C.; Gilbert, M. J., & Bernevig, B. A. *Phys. Rev. Lett.* **2014**, *112*, 106401.

(30) Fang, C.; Gilbert, M. J., & Bernevig, B. A. *Phys. Rev. B* **2012**, *86*, 115112.

(31) Fang, C.; Gilbert, M. J., & Bernevig, B. A. *Phys. Rev. Lett.* **2014**, *112*, 106401.

(32) Fu, L. *Phys. Rev. Lett.* **2011**, *106*, 106802.

(33) Fu, L. & Kane, C. L. *Phys. Rev. B* **2007**, *76*, 045302.

(34) Fu, L.; Kane, C. L., & Mele, E. J. *Phys. Rev. Lett.* **2007**, *98*, 106803.

(35) Fu, Z.; Liu, M., & Yang, Z. *Phys. Rev. B* **2019**, *99*, 205425.

(36) Hasan, M. Z. & Kane, C. L. *Rev. Mod. Phys.* **2010**, *82*, 3045–3067.

(37) Hasan, M. Z. & Kane, C. L. *Rev. Mod. Phys.* **2010**, *82*, 3045–3067.

(38) Hsieh, T. H.; Lin, H.; Liu, J.; Duan, W.; Bansil, A., & Fu, L. *Nature Communications* **2012**, *3*, 982.

(39) Hsu, C.-H.; Stano, P.; Klinovaja, J., & Loss, D. *Phys. Rev. Lett.* **2018**, *121*, 196801.

(40) Kane, C. L. & Mele, E. J. *Phys. Rev. Lett.* **2005**, *95*, 146802.

(41) Kazakov, A.; Brzezicki, W.; Hyart, T.; Turowski, B.; Polaczynski, J.; Adamus, Z.; Aleszkiewicz, M.; Wojciechowski, T.; Domagala, J. Z.; Caha, O.; Varykhalov, A.; Springholz, G.; Wojtowicz, T.; Volobuev, V. V., & Dietl, T. Dephasing by mirror-symmetry breaking and resulting magnetoresistance across the topological transition in $Pb_{1-x}Sn_xSe$.

(42) Kim, J.; Kim, K.-W.; Shin, D.; Lee, S.-H.; Sinova, J.; Park, N., & Jin, H. *Nature Communications* **2019**, *10*, 3965.

(43) Kitaev, A. Y. *Physics-Uspekhi* **2001**, *44*, 131.

(44) Kitaev, A. *AIP Conference Proceedings* **2009**, *1134*, 22–30.

(45) Klitzing, K. v.; Dorda, G., & Pepper, M. *Phys. Rev. Lett.* **1980**, *45*, 494–497.

(46) König, M.; Wiedmann, S.; Brüne, C.; Roth, A.; Buhmann, H.; Molenkamp, L. W.; Qi, X.-L., & Zhang, S.-C. *Science* **2007**, *318*, 766–770.

(47) Kumaravadivel, P.; Pan, G. A.; Zhou, Y.; Xie, Y.; Liu, P., & Cha, J. J. *APL Materials* **2017**, *5*, 076110.

(48) Langbehn, J.; Peng, Y.; Trifunovic, L.; von Oppen, F., & Brouwer, P. W. *Phys. Rev. Lett.* **2017**, *119*, 246401.

(49) Lee, H.; Im, J., & Jin, H. *Applied Physics Letters* **2020**, *116*, 022411.

(50) Liu, C.; Hughes, T. L.; Qi, X.-L.; Wang, K., & Zhang, S.-C. *Phys. Rev. Lett.* **2008**, *100*, 236601.

(51) Liu, J. & Fu, L. *Phys. Rev. B* **2015**, *91*, 081407.

(52) Liu, J.; Hsieh, T. H.; Wei, P.; Duan, W.; Moodera, J., & Fu, L. *Nature Materials* **2014**, *13*, 178–183.

(53) Liu, P.; Han, H. J.; Wei, J.; Hynek, D.; Hart, J. L.; Han, M. G.; Trimble, C. J.; Williams, J.; Zhu, Y., & Cha, J. J. *ACS Applied Electronic Materials* **2021**, *3*, 184–191.

(54) Löthman, T. & Black-Schaffer, A. M. *Phys. Rev. B* **2017**, *96*, 064505.

(55) Lou, W.-K.; Yang, W., & Chang, K. *Phys. Rev. B* **2022**, *105*, 045305.

(56) Lunczer, L.; Leubner, P.; Endres, M.; Müller, V. L.; Brüne, C.; Buhmann, H., & Molenkamp, L. W. *Phys. Rev. Lett.* **2019**, *123*, 047701.

(57) Lunde, A. M. & Platero, G. *Phys. Rev. B* **2012**, *86*, 035112.

(58) Matsuura, S.; Chang, P.-Y.; Schnyder, A. P., & Ryu, S. *New Journal of Physics* **2013**, *15*, 065001.

(59) Mazur, G. P.; Dybko, K.; Szczerbakow, A.; Domagala, J. Z.; Kazakov, A.; Zgirski, M.; Lusakowska, E.; Kret, S.; Korczak, J.; Story, T.; Sawicki, M., & Dietl, T. *Phys. Rev. B* **2019**, *100*, 041408.

(60)   Nagaosa, N.; Sinova, J.; Onoda, S.; MacDonald, A. H., & Ong, N. P. *Rev. Mod. Phys.* **2010**, *82*, 1539–1592.

(61)   Nichele, F. et al. *New Journal of Physics* **2016**, *18*, 083005.

(62)   Nielsen, M. D.; Levin, E. M.; Jaworski, C. M.; Schmidt-Rohr, K., & Heremans, J. P. *Phys. Rev. B* **2012**, *85*, 045210.

(63)   Nimtz G., S. B., *Narrow-gap lead salts. In: Narrow-Gap Semiconductors.* Springer Tracts in Modern Physics, vol 98. Springer, Berlin, Heidelberg: 1983.

(64)   Ojajärvi, R.; Hyart, T.; Silaev, M. A., & Heikkilä, T. T. *Phys. Rev. B* **2018**, *98*, 054515.

(65)   Paul, T.; Fernández Becerra, V., & Hyart, T. Interplay of quantum spin Hall effect and spontaneous time-reversal symmetry breaking in electron-hole bilayers I: Transport properties, 2022.

(66)   Pikulin, D. I. & Hyart, T. *Phys. Rev. Lett.* **2014**, *112*, 176403.

(67)   Qi, X.-L.; Hughes, T. L., & Zhang, S.-C. *Phys. Rev. B* **2008**, *78*, 195424.

(68)   Qi, X.-L. & Zhang, S.-C. *Rev. Mod. Phys.* **2011**, *83*, 1057–1110.

(69)   Qi, X.-L. & Zhang, S.-C. *Rev. Mod. Phys.* **2011**, *83*, 1057–1110.

(70)   Rachmilowitz, B.; Zhao, H.; Li, H.; LaFleur, A.; Schneeloch, J.; Zhong, R.; Gu, G., & Zeljkovic, I. *Phys. Rev. B* **2019**, *100*, 241402.

(71)   Rachmilowitz, B.; Zhao, H.; Li, H.; LaFleur, A.; Schneeloch, J.; Zhong, R.; Gu, G., & Zeljkovic, I. *Phys. Rev. B* **2019**, *100*, 241402.

(72)   Rechci ński, R. & Buczko, R. *Phys. Rev. B* **2018**, *98*, 245302.

(73)   Rechcinski, R.; Galicka, M.; Simma, M.; Volobuev, V. V.; Caha, O.; Snchez-Barriga, J.; Mandal, P. S.; Golias, E.; Varykhalov, A.; Rader, O.; Bauer, G.; Kacman, P.; Buczko, R., & Springholz, G. *Advanced Functional Materials* **2021**, 2008885.

(74)   Rhim, J.-W.; Behrends, J., & Bardarson, J. H. *Phys. Rev. B* **2017**, *95*, 035421.

(75)   Ryu, S.; Schnyder, A. P.; Furusaki, A., & Ludwig, A. W. W. *New Journal of Physics* **2010**, *12*, 065010.

(76)   Sadowski, J.; Dziawa, P.; Kaleta, A.; Kurowska, B.; Reszka, A.; Story, T., & Kret, S. *Nanoscale* **2018**, *10*, 20772–20778.

(77)   Safaei, S.; Galicka, M.; Kacman, P., & Buczko, R. *New J. Phys.* **2015**, *17*, 063041.

(78)   Sasaki, S.; Ren, Z.; Taskin, A. A.; Segawa, K.; Fu, L., & Ando, Y. *Phys. Rev. Lett.* **2012**, *109*, 217004.

(79)   Sasaki, S.; Ren, Z.; Taskin, A. A.; Segawa, K.; Fu, L., & Ando, Y. *Phys. Rev. Lett.* **2012**, *109*, 217004.

(80)   Schindler, F.; Cook, A. M.; Vergniory, M. G.; Wang, Z.; Parkin, S. S. P.; Bernevig, B. A., & Neupert, T. *Science Advances* **2018**, *4*, eaat0346.

(81) Schnyder, A. P.; Ryu, S.; Furusaki, A., & Ludwig, A. W. W. *AIP Conference Proceedings* **2009**, *1134*, 10–21.

(82) Schnyder, A. P.; Ryu, S.; Furusaki, A., & Ludwig, A. W. W. *Phys. Rev. B* **2008**, *78*, 195125.

(83) Sessi, P.; Di Sante, D.; Szczerbakow, A.; Glott, F.; Wilfert, S.; Schmidt, H.; Bathon, T.; Dziawa, P.; Greiter, M.; Neupert, T.; Sangiovanni, G.; Story, T.; Thomale, R., & Bode, M. *Science* **2016**, *354*, 1269–1273.

(84) Shiozaki, K. & Sato, M. *Phys. Rev. B* **2014**, *90*, 165114.

(85) Story, T.; Gała zka, R. R.; Frankel, R. B., & Wolff, P. A. *Phys. Rev. Lett.* **1986**, *56*, 777–779.

(86) Story, T.; Karczewski, G.; Świerkowski, L., & Gała zka, R. R. *Phys. Rev. B* **1990**, *42*, 10477–10487.

(87) Su, W. P.; Schrieffer, J. R., & Heeger, A. J. *Phys. Rev. Lett.* **1979**, *42*, 1698–1701.

(88) Tanaka, Y.; Ren, Z.; Sato, T.; Nakayama, K.; Souma, S.; Takahashi, T.; Segawa, K., & Ando, Y. *Nature Physics* **2012**, *8*, 800.

(89) Tanaka, Y.; Furusaki, A., & Matveev, K. A. *Phys. Rev. Lett.* **2011**, *106*, 236402.

(90) Teo, J. C. Y.; Fu, L., & Kane, C. L. *Phys. Rev. B* **2008**, *78*, 045426.

(91) Teo, J. C. Y. & Hughes, T. L. *Phys. Rev. Lett.* **2013**, *111*, 047006.

(92) Trimble, C. J.; Wei, M. T.; Yuan, N. F. Q.; Kalantre, S. S.; Liu, P.; Han, H. .-.; Han, M. .-.; Zhu, Y.; Cha, J. J.; Fu, L., & Williams, J. R. Josephson Detection of Time Reversal Symmetry Broken Superconductivity in SnTe Nanowires.

(93) Väyrynen, J. I.; Goldstein, M.; Gefen, Y., & Glazman, L. I. *Phys. Rev. B* **2014**, *90*, 115309.

(94) Volobuev, V. V.; Mandal, P. S.; Galicka, M.; Caha, O.; Snchez-Barriga, J.; Di Sante, D.; Varykhalov, A.; Khiar, A.; Picozzi, S.; Bauer, G.; Kacman, P.; Buczko, R.; Rader, O., & Springholz, G. *Advanced Materials* **2017**, *29*, 1604185.

(95) Wu, S.; Fatemi, V.; Gibson, Q. D.; Watanabe, K.; Taniguchi, T.; Cava, R. J., & Jarillo-Herrero, P. *Science* **2018**, *359*, 76–79.

(96) Xu, S.-Y. et al. *Nature Communications* **2012**, *3*, 1192.

(97) Yang, H.; Li, Y.-Y.; Liu, T.-T.; Xue, H.-Y.; Guan, D.-D.; Wang, S.-Y.; Zheng, H.; Liu, C.-H.; Fu, L., & Jia, J.-F. *Advanced Materials* **2019**, *31*, 1905582.

(98) Yang, H.; Li, Y.-Y.; Liu, T.-T.; Xue, H.-Y.; Guan, D.-D.; Wang, S.-Y.; Zheng, H.; Liu, C.-H.; Fu, L., & Jia, J.-F. *Advanced Materials* **2019**, *31*, 1905582.

(99) Zhao, Y. X. & Wang, Z. D. *Phys. Rev. Lett.* **2013**, *110*, 240404.

(100) Zhao, Y. X. & Wang, Z. D. *Phys. Rev. B* **2014**, *89*, 075111.

(101)   Zirnbauer, M. R. *Journal of Mathematical Physics* **1996**, *37*, 4986–5018.